

**METHANE HYDRATE DISTRIBUTION OFFSHORE VANCOUVER ISLAND
FROM DETAILED SINGLE CHANNEL SEISMIC STUDIES**

by

Cameron Roger Fink
B.Sc., University of Alberta, Canada, 1993

A Thesis Submitted in Partial Fulfillment of the
Requirements for the Degree of

MASTER OF SCIENCE

in the School of Earth and Ocean Sciences

We accept this thesis as conforming
to the required standard

[REDACTED]

Dr. George D. Spence, Supervisor (School of Earth and Ocean Sciences)

[REDACTED]

Dr. Roy D. Hyndman, Member (Pacific Geoscience Centre, Geological Survey of
Canada)

[REDACTED]

Dr. Michael J. Whiticar, Member (School of Earth and Ocean Sciences)

[REDACTED]

Dr. Inez Fung, Member (School of Earth and Ocean Sciences)

[REDACTED]

Dr. Kristin M.M. Rohr, External Examiner (Pacific Geoscience Centre, Geological
Survey of Canada)

© Cameron R. Fink, 1995.

University of Victoria

All rights reserved. This thesis may not be reproduced in whole or in part, by photocopy
or other means, without the permission of the author.

Supervisor: Dr. George D. Spence

ABSTRACT

A detailed single channel seismic reflection survey of a region on the Juan de Fuca continental margin, 50 km offshore Vancouver Island, with a clear gas hydrate bottom-simulating reflector has been analyzed and interpreted. The results have been integrated with previously obtained multichannel seismic and Ocean Drilling Program borehole geophysical data. Seismic data includes tightly spaced single channel data collected in the immediate vicinity of Site 889 during Pacific Geoscience Centre (Geologic Survey of Canada) Cruise PGC93002 in June, 1993, and 100% coverage versions of multichannel lines collected in 1989. Borehole data includes sonic and density logs, drill core density estimates, and vertical seismic profile velocity estimates from Ocean Drilling Program Site 889.

Approximately 610 km of single channel data were acquired in two tightly spaced grid patterns, GRID A and GRID B, with survey lines in each grid nominally spaced 200 m and 100 m apart, respectively. GRID A consists of 41 lines, 12 km long (~500 km total), and covers approximately 100 km². GRID A used a 1.97 L (120 in.³) airgun as its acoustic source which generated a dominant frequency of 75 Hz. GRID B consists of 28 lines, 4 km long (~110 km) and covers approximately 11 km². These data were acquired with a 0.65 L (40 in.³) airgun, yielding a dominant frequency of 150 Hz. The 100% coverage lines were acquired with an airgun array of total volume 128.2 L (7820 in.³). This array produced a dominant acoustic frequency of 30 Hz.

The seismic survey target was the bottom simulating reflector (BSR) which corresponds to the base of the methane hydrate stability field, estimated at less than 240 mbsf in the study area. The BSR response to varying source frequencies has been examined and clearly suggests that the required negative impedance contrast is derived from a combination of high-velocity hydrated sediments above the BSR, and low velocity gas-bearing sediments below. Tuning width synthetic seismogram modeling has shown that these layers can not be thin (i.e., < 25 m), and that each layer must have a gradational boundary away from the BSR, since no sharp top to the hydrated sediment layer or sharp bottom to the gas-bearing sediment layer is observed on seismic data of any available frequency.

Reflection coefficient analysis shows a high degree of variability in reflector strength across the study area, and has established that local highs in seafloor and BSR reflectivity are closely correlated to local maxima in seafloor topography. The strongest reflections occur beneath a ridge formed by an anticlinal uplift of accretionary wedge

sediments. Reflection coefficients as high as 0.20 for the BSR, and as high as 0.60 for the seafloor have been calculated in these areas. Synthetic models suggest that the high seafloor reflection coefficients are associated with regions where methane-bearing fluids reaching the seafloor have reacted with seawater to produce a thin layer of carbonate pavement. High reflection coefficient values for the BSR have been interpreted as regions where increased sediment hydration has occurred due to an inferred increased fluid flux.

Hydrate concentration has been estimated from the BSR reflection coefficients and suggests that the hydrated sediments above the BSR, for the 100 km² of GRID A, contain approximately 3.92×10^8 m³ of methane hydrate, which yields a methane gas volume at standard temperature and pressure of 6.43×10^{10} m³ (2.07 tcf).

Examiners:



Dr. G.D. Spence, Supervisor (School of Earth and Ocean Sciences)



Dr. Roy D. Hyndman, Member (Pacific Geoscience Centre, Geological Survey of Canada)



Dr. Michael J. Whiticar, Member (School of Earth and Ocean Sciences)



Dr. Inez Fung, Member (School of Earth and Ocean Sciences)



Dr. Kristin M.M. Rohr, External Examiner (Pacific Geoscience Centre, Geological Survey of Canada)

TABLE OF CONTENTS

ABSTRACT.....	ii
TABLE OF CONTENTS.....	iv
LIST OF TABLES.....	viii
LIST OF FIGURES.....	ix
ACKNOWLEDGMENTS.....	xi
CHAPTER ONE INTRODUCTION	
1.1 Methane Hydrate History and Global Volume Estimates.....	1
1.1.1 Stability Conditions.....	1
1.1.2 Seismic Character and the Role of Free Gas.....	2
1.1.3 Global Distribution.....	5
1.2 Motivation for Methane Hydrate Investigation.....	6
1.2.1 Methane Hydrates as a Fuel Source.....	6
1.2.2 Methane Hydrates as a Mechanism for Geologic Hazard.....	8
1.2.3 Global Climate Change.....	8
1.2.4 Heat Flow Indicator.....	9
1.3 Current Hydrate Formation Models.....	10
1.3.1 Basic Constraints.....	10
1.3.2 Models.....	11
1.3.3 Discussion of Formation Models.....	12
1.4 Geologic and Geophysical Background.....	14
1.5 Thesis Outline.....	17
1.5.1 Primary Objectives.....	17
1.5.2 Secondary Objectives.....	18

CHAPTER TWO DATA ACQUISITION AND PROCESSING

2.1 Seismic Survey Parameters.....	19
2.1.1 Single Channel Seismic Data.....	19
2.1.2 Ocean Bottom Seismometer Data.....	28
2.2 Instrumentation.....	29
2.2.1 Seismic Data Acquisition.....	29
2.2.2 Navigation.....	29
2.3 Multichannel Seismic Data.....	30
2.4 Data from Ocean Drilling Program Site 889.....	32
2.4.1 Sonic Logs at ODP Site 889.....	32
2.4.2 VSP Data at ODP Site 889.....	34
2.4.3 VSP Data vs. Sonic Data.....	35
2.5 Processing of Single Channel Seismic Data.....	36
2.5.1 Filtering and Deconvolution.....	36
2.5.2 Analysis of Data from Large Airgun Array.....	39
2.5.3 Picking Horizons.....	39
2.5.4 Mapping Regional Variation.....	40

CHAPTER THREE AMPLITUDE ANALYSIS

3.1 Amplitude.....	44
3.1.1 Seafloor Amplitude.....	44
3.1.2 BSR Amplitude.....	47
3.1.3 Cross-Line Analysis.....	47
3.2 Conversion of Amplitudes to Reflection Coefficients.....	50
3.2.1 Warner's Method.....	50
3.2.2 Trace-by-Trace Warner's Method Application.....	52
3.2.3 Bin-by-Bin Warner's Method Application.....	55

3.2.4 Validity of a Local Application of Warner's Method.....	58
3.2.5 Single Value Warner's Method Application.....	59
3.2.6 Tying the Seismic Data to the Drillhole.....	60
3.3. Reflection Coefficient Results.....	61
3.3.1 Seafloor Reflector.....	61
3.3.2 Bottom Simulating Reflector.....	63

CHAPTER FOUR FREQUENCY ANALYSIS

4.1 Objectives of Frequency Analysis.....	66
4.2 Wavelet Extraction.....	66
4.3 Synthetic Seismograms from VSP Data.....	67
4.4 Synthetic Seismogram Modeling.....	73
4.4.1 Tuning Width Analysis.....	73
4.4.2 Carbonate Pavement at the Seafloor.....	83
4.5 Frequency Analysis Overview.....	84

CHAPTER FIVE DISCUSSION

5.1 Factors Affecting Seismic Amplitudes.....	88
5.1.1 Focusing and Defocusing.....	88
5.1.2 Scattering and Anelastic Attenuation.....	88
5.2 Frequency Analysis Results.....	90
5.2.1 Tuning Width Analysis.....	90
5.2.2 Seafloor Reflectivity Implications.....	91
5.3 Reflection Coefficient Analysis Results.....	92
5.3.1 Seafloor Reflectivity.....	92
5.3.2 BSR Reflectivity.....	93
5.4 Estimates of Hydrate Saturation.....	95

5.4.1 Hydrate Volume Estimate Assumptions.....	95
5.4.2 Hydrate Concentration Calculation.....	97
5.4.3 Regional Methane Gas Volume Estimate.....	100
CHAPTER SIX CONCLUSIONS	
.....	102
BIBLIOGRAPHY.....	105

LIST OF TABLES

Table 1.1.....6

LIST OF FIGURES

Figure 1.1	Gas hydrate structure I.....	1
Figure 1.2	Pressure/temperature phase diagram for methane hydrate.....	3
Figure 1.3	Offshore/onshore structural cross-section (Vancouver Island margin).....	15
Figure 2.1	Seismic survey location map.....	20
Figure 2.2	Seismic data detailed location map.....	21
Figure 2.3	GRID A lines SCS-6, SCS-9, and SCS-13.....	22
Figure 2.4	GRID A lines SCS-15, SCS-17, and SCS-20.....	23
Figure 2.5	GRID A lines SCS-23, SCS-24, and SCS-25.....	24
Figure 2.6	GRID A lines SCS-27, SCS-30, and SCS-35.....	25
Figure 2.7	GRID A lines SCS-38, SCS-41, and SCS-43.....	26
Figure 2.8	GRID B lines SCS-56, SCS-63, SCS-74, and SCS-83.....	27
Figure 2.9	100% coverage MCS lines 89-08 and 89-10.....	31
Figure 2.10	Sonic log, VSP and density data from ODP Site 889.....	33
Figure 2.11	Amplitude spectra for typical 30 Hz, 75 Hz and 150 Hz seismic lines.....	37
Figure 2.12	Effectiveness of predictive deconvolution.....	38
Figure 2.13	Map representation of seafloor topography from GRID A.....	42
Figure 2.14	3-D view of seafloor topography from GRID A.....	43
Figure 3.1	Seafloor amplitude map from GRID A.....	45
Figure 3.2	BSR amplitude map from GRID A.....	46
Figure 3.3	Cross-line seafloor amplitudes.....	49
Figure 3.4	Seafloor primary and water bottom multiple raypaths for single channel seismic acquisition.....	51
Figure 3.5	Trace-by-trace reflection coefficients for SCS-19.....	53
Figure 3.6	Seafloor WBM amplitude map from GRID A.....	56
Figure 3.7	Bin-by-bin reflection coefficients for GRID A.....	57

Figure 3.8	Best estimates for seafloor reflection coefficients (GRID A).....	62
Figure 3.9	Best estimates for BSR reflection coefficients (GRID A).....	65
Figure 4.1	Source wavelets for the primary frequencies.....	68
Figure 4.2	Comparison of seismic data and synthetic seismograms generated from the VSP at 889B.....	70
Figure 4.3	Observation of only a single BSR reflection for seismic lines of the three primary frequencies (1).....	75
Figure 4.4	Observation of only a single BSR reflection for seismic lines of the three primary frequencies (2).....	76
Figure 4.5	Regional velocity-depth function for typical margin sediments in the survey area.....	77
Figure 4.6	Tuning width velocity models.....	78
Figure 4.7	Wedge model synthetic seismograms for free gas zone.....	80
Figure 4.8	Wedge model synthetic seismograms for hydrate zone.....	81
Figure 4.9	Seafloor amplitude variation between 30 Hz and 75 Hz coincident lines.....	85
Figure 4.10	Carbonate pavement synthetic seismograms.....	86
Figure 5.1	Hydrate velocity and concentration map.....	96

ACKNOWLEDGMENTS

I want to extend thanks to my supervisor, Dr. George D. Spence, who was extremely helpful in guiding the research for this thesis, and whose financial support, together with the University of Victoria Fellowship, has made a graduate school experience possible for me. Dr. Spence was particularly accommodating during the later stages of the thesis development devoting many hours of his free time to a review of the material, and to handling the logistics of a summer session defense.

I extend thanks to my graduate committee; Dr. Roy D. Hyndman, Dr. Michael J. Whiticar, and Dr. Inez Fung who provided useful discussion for, and revisions to the thesis. Additional thanks are owed to Dr. Kristin M.M. Rohr who took time out of her busy schedule to review this thesis, and attend the defense as the external examiner.

Thank-you to the captain and crew of the research vessel C.S.S. John P. Tully employed during acquisition of the single channel seismic data, and to the Pacific Geoscience Centre (Geological Survey of Canada) for the use of the data acquisition system.

I owe a special thanks to Dr. Rolf Lueck who allowed the use of his color plotter and who also offered invaluable advice concerning MatLab programming and display options, and to Steve Lynch for the disbursement and support of the latest version of Outrider synthetic seismogram modeling software. I would also like to thank Tianson Yuan, Bernard Desmons, Daniel Oleskevich, and Joe Henton who were always available for advice, consultation, or help with computer applications.

Finally, a sincere thank-you to my wife, Kimberley, who stood by me through it all, and without whose support this accomplishment would not have been possible.

CHAPTER ONE INTRODUCTION

1.1 METHANE HYDRATE HISTORY AND GLOBAL VOLUME ESTIMATES

1.1.1 Stability Conditions

Methane hydrates are a type of clathrate compound, a naturally occurring solid comprised of three-dimensional lattice framework structures of water ice with open cages, into which various molecules can fit (Figure 1.1). In this situation water crystallizes in the isometric crystallographic system rather than the hexagonal system of normal ice. Two structures (I & II) of the isometric form are found in nature. Structure I is the most common and is able to accommodate molecules of H₂S, CO₂, ethane and methane. Structure II has some cages large enough to hold molecules of propane and isobutane (Sloan, 1990).

The maximum amount of methane that can occur in a clathrate is fixed by the clathrate geometry. In a fully saturated structure I methane hydrate, one molecule of methane is present for every $5\frac{3}{4}$ molecules of water. The volume ratio of methane gas to solid methane hydrate is estimated to be between 150:1 and 180:1 (Hunt, 1979, *ref. in Kvenvolden, 1993*). The upper limit assumes a fully methane saturated

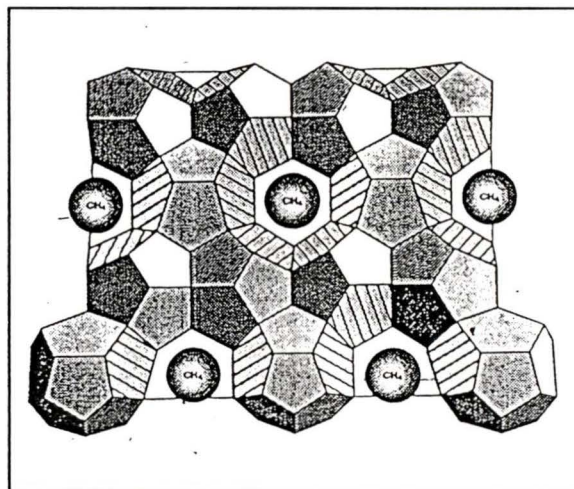


Figure 1.1
Gas hydrate structure I. Each methane molecule is effectively trapped by rigid cages of hydrogen-bonded water molecules. Structure is stable when >85% of cages are filled. From Kvenvolden (1993).

structure, while the lower limit assumes 85% of the cages filled with methane, below which the hydrate structure is not stable. With a ratio of such magnitude seemingly moderate volumes of solid methane hydrate can yield large volumes of gas.

Gas hydrates will usually form with about 90% of the clathrate cages filled. However, because methane solubility in sea water is very low (approximately 0.045 volumes of methane per volume of water at standard temperature and pressure [Sloan, 1990]), enormous amounts of methane gas production are necessary for the formation of hydrates, and this therefore limits the regions on Earth where gas hydrates can be expected and are found. Typically we can expect to find hydrates in marine sediments on the continental margins and in permafrost regions (Kvenvolden, 1993). We limit our discussion here to the marine case.

Provided sufficient methane concentrations are present, the stability of hydrates is primarily controlled by an interrelation of temperature and pressure. Secondary controls include the concentration of gases other than methane, and ionic impurities in the local sea water. Figure 1.2 is a phase diagram showing the boundary between free gas methane and methane hydrate from the equation of state computation for artificial seawater by Englezos and Bishnoi (1988). Methane hydrates are stable in sediments to depths of several thousand meters, and at temperatures below 25°C, depending on depth below seafloor. The maximum depth limit for the stability zone is a function of the geothermal gradient, below which the temperature is too high to permit the formation of hydrates.

1.1.2 Seismic Character and the Role of Free Gas

As drilling of hydrates has only recently been approved by the Ocean Drilling Program, previous inferences of hydrate occurrence have been based on the appearance of bottom simulating reflectors (BSRs). These reflectors mark the presumed base of the hydrate stability field below which the temperature is too high to permit the formation of methane hydrate.

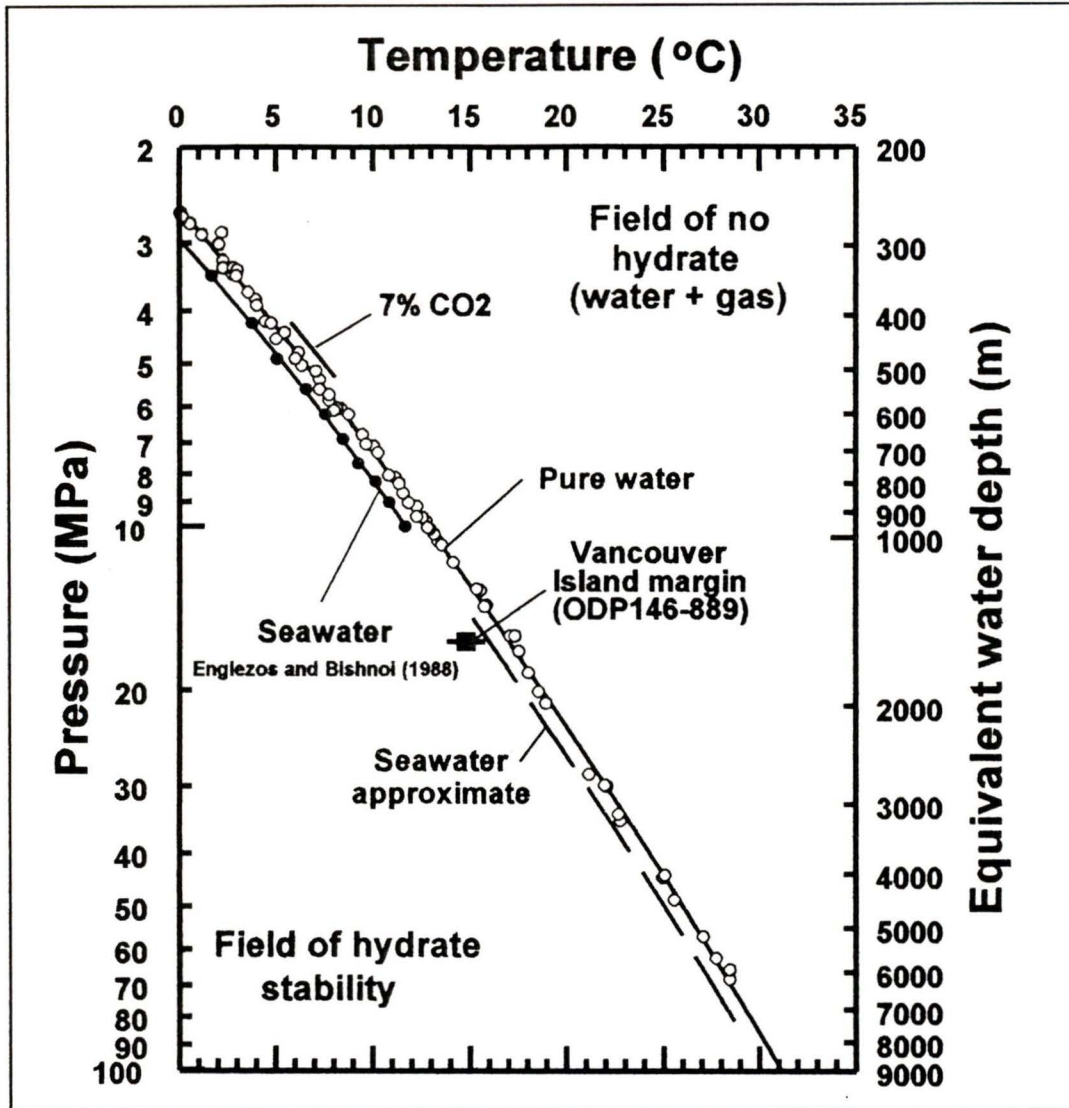


Figure 1.2
 Pressure/temperature phase diagram for methane hydrate stability. The solid line seawater curve is from the equation-of-state computation for artificial seawater by Englezos and Bishnoi (1988). Modified from Hyndman and Davis (1992).

The Bottom Simulating Reflection

A typical methane hydrate BSR may be seismically characterized in three ways:

- (1) The BSR is a single symmetrical pulse characteristic of a simple two-medium interface.

- (2) The polarity of the reflector is reversed relative to the seafloor reflection indicating a lower acoustic impedance below the interface.
- (3) The reflection coefficients are reasonably large, requiring a large impedance contrast between the two layers.

Interface Models

The negative impedance boundary correlates closely with the predicted base of the hydrate stability zone. A decrease in velocity across the boundary may be a result of (1) high velocity hydrate (3.3 - 3.8 km/s) above the BSR (MacDonald, 1990b), (2) it may be due to the presence of free gas in sediments below the hydrate which results in a sonic velocity much slower than water saturated sediments, or (3) it may be the result of a combination of the above two phenomena.

Mackay et al (1994) argued that the impedance contrast, in the Cascadia subduction zone, is solely the result of free gas. They envisioned that the BSR is the pressure/temperature dependent phase boundary marking the top of the free gas zone, and that this model is probable in other regions where strong BSRs are observed. Hyndman and Spence (1992), on the other hand, argued that no free gas is required to produce such an impedance contrast at Cascadia, but also recognized that their model is non-unique and so acknowledged the possible existence of free gas below the BSR.

The question of whether or not free gas exists below the BSR is still open to debate, although recent evidence from Ocean Drilling Program expeditions suggests that there is a good probability for a small percentage of free gas to exist just below the hydrate stability zone [DSDP Leg 76, Blake Bahamas, 1983; Leg 110, Barbados, 1986; Leg 112, Peru Margin, 1986; Leg 141, Chile Triple Junction, 1991/92; Leg 146, Cascadia Subduction Zone, 1992].

Currently three models have been proposed to explain the required impedance contrast at the BSR:

(1) A layer of sediments containing a small percentage of free gas (1-5%) overlain by sediments containing a very small amount of hydrate (Minshull and White, 1989; MacKay et al., 1994). This theory derives the required impedance contrast almost entirely from the presence of free gas below hydrate.

(2) A layer of normal, unhydrated, gasless sediments overlain by sediments containing a large concentration of hydrate in the pore space (Hyndman and Spence, 1992). This theory derives the necessary impedance contrast solely from the high velocity hydrate infilling at least $\frac{1}{3}$ of the pore space (assuming 50% porosity).

(3) A combination of the above two hypotheses, with moderate amounts of hydrate infilling the pore space of the uppermost sediments and free gas concentrations of 1% or greater in the sediments below (e.g., Miller et al., 1991; Kvenvolden, 1993; Katzman, Holbrook, and Paull, 1994; Minshull et al., 1994).

1.1.3 Global Distribution

Pressure and temperature requirements of the hydrate stability zone limit their existence to two regions: polar continental and moderate to deep oceanic. Irrefutable evidence from drilling has identified marine methane gas hydrates at the following locations: offshore Peru, Costa Rica, Guatemala, southeastern United States, western United States, western Canada, Gulf of Mexico, Black Sea, Caspian Sea, and Okhotsk Sea. Continental slope hydrates are widespread around the world (Kvenvolden, 1988), but the majority of well-defined occurrences are in subduction zones, where large clastic sedimentary wedges have been scraped off the incoming and underthrusting seafloor. Hydrates do not appear to occur in the sediments of deep sea basins, and occur only infrequently on stable continental margins (Hyndman, 1992), although some stable margin reservoirs, such as Blake Ridge offshore North Carolina, can be very large.

It has been suggested that the reservoir of carbon in methane hydrates far exceeds most other carbon reservoirs, including oil, coal and natural gas (Gornitz and Fung, 1994). Table 1 shows current estimates for both the oceanic margin and for continental

permafrost regions. Estimates of carbon volume in methane hydrates vary widely between 3.1 and $7600 \times 10^{15} \text{ m}^3$ for marine sediments and between 0.014 and $34 \times 10^{15} \text{ m}^3$ for continental permafrost. The amount of gas trapped in hydrate form is probably enormous but current estimates are highly speculative.

Volume, 10^{15} m^3	Mass, 10^{12} kg	Reference
<i>Oceanic</i>		
3.1	1.7×10^3	<i>McIver</i> [1981]
5-25	$(2.7-13.7) \times 10^3$	<i>Trofimuk et al.</i> [1977]
7600	4100×10^3	<i>Dobrynin et al.</i> [1981]
17.6	11×10^3	<i>Kvenvolden</i> [1988b]
19.5	$\sim 11 \times 10^3$	<i>MacDonald</i> [1990]
<i>Continental</i>		
0.014	7.5	<i>Meyer</i> [1981]
0.031	17	<i>McIver</i> [1981]
0.057	31	<i>Trofimuk et al.</i> [1977]
34	18000	<i>Dobrynin et al.</i> [1981]
	400	<i>MacDonald</i> [1990]

Estimates are adapted from *Potential Gas Committee* [1981].

Table 1.1
Estimates of the amount of methane in gas hydrates of Oceanic margin and permafrost settings. From *Gornitz and Fung* (1994).

1.2 MOTIVATION FOR METHANE HYDRATE INVESTIGATION

The question of why we should study methane hydrates can be addressed in four ways: (1) it potentially represents a substantial carbon fuel resource, (2) it may be one of the driving forces behind many marine geological hazards, (3) it may have had a significant effect on global climate in the past, and could affect global climate in the future, and (4) the base of the hydrate stability field (signified by the BSR) can be used in determining heat and fluid flow in accretionary wedges.

1.2.1 Methane Hydrates as a Fuel Source

Gas hydrates have real potential as a future carbon fuel source and there appears to be vast reserves of this resource. The United States Department of Energy believes that methane hydrates may represent a potential fuel reserve that will dwarf all the fossil fuel deposits on land combined (Appenzeller, 1991).

Essentially three factors make methane hydrates an attractive future carbon fuel source. First is the apparent huge volumes potentially available in reasonably limited

(spatially) sediment stores. The energy density of methane hydrates is estimated at 10 times greater than the energy density of other unconventional sources of natural gas, such as coal beds, tight sands and black oil shales, and 2 to 5 times greater than conventional natural gas (MacDonald, 1990a). Second is that hydrates are distributed globally wherever continental margins exist. The existence of these hydrates offshore Japan, combined with a notable lack of conventional natural gas prospects, has prompted some of Japan's leading energy companies to take a serious look at methane hydrates as a future energy resource (Murota, 1995). Third, is that compared to oil and coal, methane gas is extremely clean burning.

Currently three principal methods are being considered for extraction of the methane gas from its clathrate state: thermal stimulation, depressurization, and inhibitor injection (Kvenvolden, 1993). Warm water circulation into the hydrate and horizontal drilling techniques provide alternative production methods. Holder et al. (1984) determined a combination of depressurization combined with hot water injection to be the most practical where free gas is anticipated below the base of the hydrate stability zone. However, it is uncertain whether the energy required to release the gas is significantly less than the energy extracted from it. Global demand and the market price for natural gas will determine what constitutes significant.

Methane gas has been exploited from continental permafrost gas hydrates at the Messoyakha gas field in western Siberia. However, the methanol injection production methods proved overly expensive for sustained economic viability (Makogan, 1981). Sloan (1990) suggests that the North Slope of Alaska will be the probable region of initial commercial production as the infrastructure for handling gas is already in place. However, we are not likely to see commercial production until the 21st century.

1.2.2 Methane Hydrates as a Mechanism for Geologic Hazard

As hydrates dissociate, due to a change in the pressure and/or temperature regime, the pore space may become overpressured due to newly released free gas. The overpressuring creates a zone of low shear strength, which could lead to failure from gravitational loading or seismic disturbances resulting in massive slumping or submarine slides (Kvenvolden, 1993). A stability zone change might occur as a result of sea level lowering or an increase in bottom water temperatures.

Periodic eustatic sealevel changes or associated temperature changes provide mechanisms for the accumulation and dissociation of submarine gas hydrates. The last Pleistocene regression, 28 to 17 thousand years ago, involved a sea level drop of approximately 100 m. This drop in sea level corresponds to a seafloor pressure change of 1000 kPa, enough to initiate dissociation at the base of the gas hydrates, and subsequent failure on moderate slopes. Several examples of slumps and submarine slides attributed to methane hydrate dissociation have been cited by Kvenvolden (1993). In the Beaufort Sea, he has demonstrated a remarkable coincidence between known landslide structures and the inferred presence of gas hydrates. Similar marine slump scars are also evidenced in the Blake Ridge/Bahamas region. Hydrate dissociation from marine slumping has been cited, by some scientists, as a possible explanation for the mysterious disappearance of ships in the Bermuda Triangle (Appenzeller, 1991).

On a smaller scale hydrates can cause damage when dissociation occurs as a result of drilling and production of conventional oil and gas reserves. The destabilization caused from the increased heat can result in casing failures from high pressure gas "blow-outs", and in many cases dissociation has led to catastrophic well site subsidence.

1.2.3 Global Climate Change

Methane is considered a "greenhouse gas" because it is radiatively active (Watson et al., 1990). It has a global warming potential 20 times greater than an equivalent volume of

carbon dioxide when integrated over a 100-yr. span (Shine et al., 1990). The amount of methane trapped as hydrate, both on- and offshore is estimated at 3000 times the amount in the atmosphere (Whiticar, 1990). A large release of methane from this source could have a significant impact on atmospheric composition of properties which affect global warming.

Although the continental hydrates in the polar regions of the earth are more susceptible or vulnerable to global climate change (Miller et al., 1991) it may be the negative feedback loop of the marine hydrates that aids in driving the global climate over geologic time. As mentioned previously, when temperatures fall, ice advances and sea levels drop, thus destabilizing the hydrates and releasing methane gas to the atmosphere. This increases the concentration of radiatively active agents in the atmosphere and trends toward a global warming. The warming then instigates a eustatic sea level rise, increasing sea floor pressure, lowering the hydrate stability zone, and promoting the accumulation of hydrate structures within the zone.

MacDonald (1990b) proposes a positive feedback cycle for dissociation of hydrates. He suggests that the global warming due to an enhanced interglacial plus the effects of anthropogenic greenhouse gases, will lead to significant sealevel rise which could provide another mechanism for the decomposition of hydrates. This scenario is mainly applicable to continental permafrost hydrates which are sustained as a function of very low temperatures and the absence of SO_4 . Relatively warm oceanic water flooding permafrost plains could significantly increase the in-situ temperature of near-surface hydrates, while only marginally increasing pressure, thus releasing large volumes of methane to the atmosphere.

1.2.4 Heat Flow Indicator

The BSR has been used to infer heat flow in continental margin settings (Yamano et al., 1982) because its depth is primarily constrained by the geothermal gradient. An example

of the use of this method comes from offshore Peru where geothermal gradients of 43° and 49.5°C/km were estimated in two areas from the BSRs, and are consistent with results obtained by conventional methods such as downhole temperature and surface heat flow measurements (Hyndman et al., 1992). The overall heat flow uncertainty using the BSR depth method is estimated at $\pm 20\%$ (Davis et al., 1990).

1.3 CURRENT HYDRATE FORMATION MODELS

1.3.1 Basic Constraints

Although thermogenic methane hydrates are possible (Brooks et al., 1985; Kvenvolden, 1993), studies of the relatively few DSDP/ODP drillcore, or gravity-cored samples (e.g., Westbrook et al., 1995) indicates most methane in hydrates are of biogenic (bacterial) origin (MacDonald, 1990b). The evidence is based on the isotopic composition of the methane, and the methane to ethane plus propane ratio in both the clathrates and the surrounding pore water. Methane should constitute ~99% of the hydrocarbon gas mixture if the gas is biogenic. The isotopic composition of biogenic methane ($\delta^{13}C$) is expected between -55‰ and -85‰, compared to the thermogenic composition of between -25‰ and -60‰ (Sloan, 1990). The decomposition of fermentable organic matter in the anaerobic environment of marine sediments (i.e., below 10 m of sediment) yields methane as the primary product. The temperature range for biogenic methane production is broad, estimated at between 4° and 55° Celsius with an optimum between 35° and 42° C (MacDonald, 1990b). A detailed description of biogenic methane production is given in Makogan (1978). Makogan predicts that, in order for clathrate hydrates to form, the methane concentration must exceed the solubility of methane in pore water. However, the necessity of methane over-saturation prior to hydration has been challenged by Hyndman & Davis (1992), and the issue is currently unresolved.

1.3.2 Models

In-Situ Formation Model

The first model, advocated by Claypool and Kaplan (1974) but favored by many authors (Kvenvolden and Barnard, 1983; Brooks et al., 1985), proposes that methane is produced microbially from organic matter within the zone of hydrate stability. This model requires that free gas be present below all BSRs for if there is enough methane to form hydrates within the stability field there should be enough to be present as free gas below the hydrate stability zone, assuming methane concentration is over saturated with respect to seawater. The theory requires a massive quantity of carbon-bearing sediments in a relatively small section of the sediment column.

Fluid Expulsion Model

The second model, put forth by Hyndman and Davis (1992), suggests that methane is produced microbially at depths well below the stability zone, but not at depths sufficient for thermogenic production. The hydrate is formed by the upwelling of methane-rich, but unsaturated, fluids which become saturated after moving into the stability field, and hence release methane to form hydrate. Hydrate formation is then possible in regions where sediments are carbon depleted. This theory does not specifically require that free gas be present but it does not exclude free gas either. Upward movement of the stability zone would result in free gas due to the dissociation of previously hydrated sediment.

The shortening associated with thrust structures in accretionary margins may support the fluid expulsion theory of hydrate formation, in effect squeezing methane-bearing fluid from the sediments within and underlying anticlinal structures. Conversely, in passive margins, fluids are released as sediments are compacted with depth (i.e., in very thick sediment accumulations).

Gas Bubble Migration Model

The third model, advanced by Minshull et al. (1994), suggests that the mechanism of formation is by upward migration of free methane gas bubbles. This mechanism, it is argued, is consistent with gas concentration in structural highs, seen on multichannel seismic data collected offshore Columbia. If gas bubbles are permitted to travel some distance into the hydrate stability field before becoming hydrated the problem of a self-sealing hydrate layer is avoided. Once hydrate crystals have been formed some distance above the base of the stability zone, the hydrate may then build downward as more free gas migrates up. Indirect evidence that free gas migration through the stability field does occur comes from hydrates collected in piston cores at 530-560 m water depth in the Gulf of Mexico (Brooks et al., 1984). BSR depths and hydrothermal gradient estimates suggest that the base of the stability field in this region is 570 m below seafloor, which suggests that the methane (plus other hydrocarbons) must have traveled a distance of this order before they became hydrates.

1.3.3 Discussion of Formation Models

Hyndman and Davis (1992) argued that the assumption of in-situ methane production as the source for methane hydrate formation leads to several questions that do not have obvious answers.

(1) What is the origin of the large amounts of methane that the hydrate contains? Large quantities, as are required for hydrate formation, probably cannot be produced locally from common concentrations of organic material (< 2-3%; Claypool and Kaplan, 1974).

(2) Why is free gas not seismically detectable everywhere below the base of the hydrate stability zone? If the methane concentration within the stability field is large enough for hydrates to form, then the concentration below the stability field would be large enough for large amounts of free gas to be present. Amplitude versus offset (AVO)

analysis performed in the Cascadia subduction zone (Hyndman & Spence, 1992) does not support a free gas interpretation in all areas. However, AVO analysis by Katzman et al. (1994) showed that in the Blake Ridge study area, offshore South Carolina, the free gas model is the preferred interpretation. It has been suggested that small quantities (not observable seismically) of free gas below the stability field might be the result of migration of this free gas into the stability field after initial hydrate formation (Whiticar, personal communication).

(3) Why is the hydrate primarily located near the base of the stability field? Some mechanism of concentration near the base is required. The fluid expulsion model provides such a mechanism. As the pore fluids move up into the stability zone, the methane is removed from the fluids as it forms the hydrate, and thus the hydrate zone is built from the bottom upwards, resulting in a sharp boundary at the base and a gradational top, which fits the seismic data from many study areas (Collins and Watkins, 1985; Miller et al., 1991; Hyndman and Spence, 1992; Lodolo et al., 1993; Wood et al., 1993; Singh et al., 1993; Katzman et al., 1994).

There are at least two mechanisms that can concentrate the hydrate at the base of the stability zone after hydrate formation that will apply to any of the formation theories (Westbrook et al., 1994). (i) Changes in the pressure-temperature regime will move the base of the stability zone up or down accordingly. If the base moves up then free gas will initially be formed as the methane dissociates from the hydrate form, then as the gas migrates upwards back into the zone it will be reintroduced to the hydrate form and be thus concentrated nearer the base. (ii) Separate gas-phase migration from greater depths after initial hydrate formation could result in a concentration at the base of the stability zone. However, any significant gas volume (>1%) should be seen seismically over some depth range beneath the BSRs.

(4) Why are hydrates rare in deep-sea basin settings, and why do they most commonly occur in coarse clastic accretionary sedimentary wedges? The in-situ model

does not provide an answer to this question. The fluid expulsion model, on the other hand, favors a zone of shortening where the overlying sediments are porous. The shortening associated with active accretionary wedges, such as the Cascadia subduction zone (Hyndman and Spence, 1992; Spence et al., 1995) and offshore Peru (Miller et al., 1991), tends to squeeze the deeper sediments providing a mechanism for upward fluid expulsion, and the porosity of clastic sediments, in combination with thrust faulting, provides a medium for fluid transport.

1.4 GEOLOGIC AND GEOPHYSICAL BACKGROUND

Most of the continental margin of western North America lies along the right-lateral transform boundary between the Pacific and North American plates. The San Andreas fault system extends from the Gulf of California to Cape Mendocino in northern California, and the Queen Charlotte fault system extends from just north of Vancouver Island to the Aleutian Trench of Alaska. Along the intervening margin of northern California, Oregon, Washington, and southern British Columbia, subduction of the Juan de Fuca plate takes place in the Cascadia subduction zone. The Juan de Fuca plate is the remnant of the larger Farallon plate which has fragmented and diminished in size as a result of the convergence of the East Pacific Rise spreading center and the North American continent, and the northward movement of the southern (Mendocino) triple junction.

Evidence from seafloor magnetic anomalies suggests that the main portion of the Juan de Fuca plate has been converging to the northeast and underthrusting the continent since the Eocene, presently at a rate of about 45 mm/yr (Riddihough, 1984). The North American plate has been advancing westward over the asthenosphere and overriding the Pacific plate at a rate of 20mm/yr for the past 10 Ma resulting in a relatively shallow angle of subduction (Hyndman et al., 1994).

Principal to the argument of fluid expulsion as a means of methane hydrate formation is the structure of the Cascadia accretionary prism. The northern Cascadia accretionary prism is bounded at its base by the underthrusting oceanic crust and on its landward side by the landward dipping Crescent Terrane. Off southern Vancouver Island the dip of the oceanic crust increases from 3° to 4° just seaward of the deformation front to 10° under the edge of the shelf and continues increasing to 15° beneath the Pacific coast (Hyndman et al., 1990) (see Figure 1.3). The Crescent Terrane acts as the backstop against which the oceanic sediments are scraped off the incoming Juan de Fuca plate.

The frontal portion of the accretionary prism off southern Vancouver Island has been well surveyed by seismic reflection imagery and swath bathymetry, revealing its

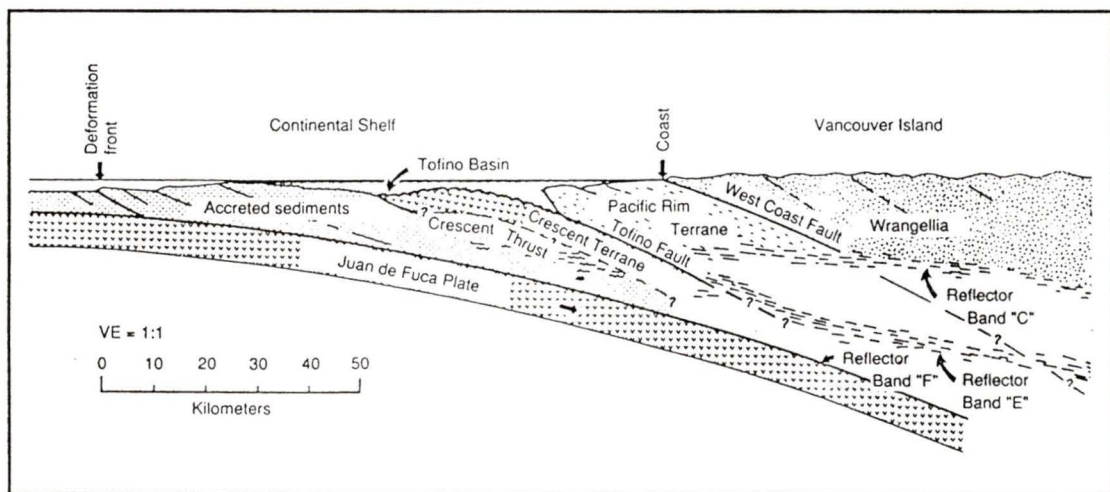


Figure 1.3

Offshore-onshore structural cross-section across southern Vancouver Island margin, showing increase in subducting slab dip angle landward. Setting for experiment is approximately denoted by deformation front location. From Hyndman et al., (1990).

surface morphology, cross-sectional geometry, and deformational style (Clowes, Yorath, and Hyndman, 1987; Davis and Hyndman, 1989; Spence, Hyndman, Davis et al., 1991, and others). The uppermost 2.5 - 3 km of crust consists of nearly 2 km of acoustically layered turbidite sediments overlying a section of more seismically transparent sediments. The oceanic crust dips gently landward toward the deformation front, with a corresponding thickening of the incoming sediment section. Maximum water depths

recorded are only 2500 m, due to the thickness of sediment and the relatively young age (5-7 Ma) of the oceanic crust.

At the deformation front sediments are folded and faulted along anticlinal ridges that run nearly parallel to the coast of Vancouver Island. These anticlinal ridges are usually 20 - 30 km long and often asymmetric with their steep sides facing seaward. The anticlines are developed over a thrust ramp which extends down to near the top of the oceanic crust, indicating that the present decollement is near the base of the sediment section and that most of the sediments are being scraped off the subducting oceanic plate at the deformation front (Davis and Hyndman, 1989).

Yuan et al. (1994) established the velocity and porosity relationship across the accretionary margin from RMS and interval velocity cross-sections on several multichannel seismic lines in the study area. Landward from the Cascadia Basin the velocities first increase in the discrete thrust zone area, probably as a consequence of increased horizontal tectonic stress. Further landward the velocities are much lower than beneath the basin. This landward decrease in velocity is inferred to be a consequence of horizontal shortening and vertical stretching of the porosity depth profile. The tectonic thickening in the section occurs faster than loading and pore fluid expulsion can re-establish a normally consolidated section.

Recent detailed seismic studies were directed at providing supporting data for drilling during ODP Leg 146 on the Cascadia margin (Westbrook et al., 1994). Objectives of the drilling program included (1) elucidation of the role of sediment consolidation and fluid expulsion in the development of the accretionary wedge, and (2) the origin of bottom-simulating reflectors and estimates of in-situ methane carbon reserves.

1.5 THESIS OUTLINE

The data set analyzed in this thesis included closely-spaced single channel seismic lines acquired in the immediate vicinity of ODP site 889. A unique opportunity was thus provided to tie extremely detailed, variable frequency seismic data to geophysical data from a drillhole within the survey area.

1.5.1 Primary Objectives

Four primary objectives have been identified.

- (1) To confirm or reject the existence of free methane gas below the BSR.
- (2) To quantify the regional variation in hydrate or gas concentration.
- (3) To obtain a more accurate estimate of the volume of methane gas sequestered by marine hydrates for this area.
- (4) To determine what role topography might play in the variation of hydrate or gas concentration.

The strength of the BSR, as measured by its reflection coefficient, has been established for a 100 km² area in the immediate vicinity of ODP site 889. By calibrating the reflection coefficient with known velocities at the drillhole, an estimate of velocity variability over the survey area has been made. The velocity contrast necessary to generate the required impedance contrast was established from which the existence of at least 1% free gas was established. An estimate of hydrate concentration above the BSR was made from the velocity interpretations by making assumptions regarding the relationship of velocity to hydrate concentration.

A correlation between "highs" in the strength of the BSR and local highs in seafloor topography was immediately evident in the data and plausible mechanisms for such an association are explored here. Regional variation in reflection strength of the seafloor was also examined, as its "hardness" can yield information about the geological processes which occur beneath it.

1.5.2 Secondary Objective

The second main focus for the thesis was the delineation of the BSR's frequency dependence. The data set contains coincident seismic data lines of three unique dominant source frequencies. Analysis of this data has enabled constraints to be established for the minimum thickness of hydrated sediments above the BSR, and rules out previous theories that suggested only a *thin* layer of free gas exists below the BSR. In some areas of the survey, the seafloor to BSR amplitude ratio varies with respect to the source frequency. A practical geologic situation which could explain this feature has been modeled.

CHAPTER TWO DATA ACQUISITION & PROCESSING

2.1 SEISMIC SURVEY PARAMETERS

The seismic data analyzed in this thesis were collected in the vicinity of Ocean Drilling Program (ODP) site 889, drilled in October of 1992 during ODP Leg 146 (Westbrook et al., 1994). Single channel seismic reflection (SCS) and wide-angle ocean-bottom seismometer (OBS) data were recorded on board the *C.S.S. John P. Tully* research vessel during Pacific Geoscience Center (PGC) cruise 93002 from June 4-17, 1993. The cruise was a collaborative project between the University of Victoria and the University of Cambridge. The data were collected near the continental margin, approximately 50 km offshore Vancouver Island (Figure 2.1), and the primary focus was the BSR which is on average less than 240 meters below seafloor (mbsf) in this area. The principal objective of the cruise was to obtain the velocity structure above, at, and below the BSR.

2.1.1 Single Channel Seismic Data

During the cruise a total of 1160 km of single channel seismic data were acquired, of which almost 500 km were shot with a 1.97 L (120 in³) airgun in a large grid pattern, GRID A (red lines on Figure 2.2). The 41 lines of this grid (SCS-4 through SCS-44) were spaced approximately 200 m apart and averaged 12 km in length, corresponding to a grid survey area of ≈ 100 km². Figures 2.3-2.7 show samples of the SCS lines from across GRID A.

Another 110 km of SCS data were shot in a transversely acquired smaller grid pattern, GRID B (yellow lines), using a 0.65 L (40 in³) airgun as the seismic source. The 28 lines of GRID B averaged 4 km in length and were nominally spaced 100 meters apart covering an area of ≈ 11 km². Figure 2.8 shows four of these smaller airgun lines from

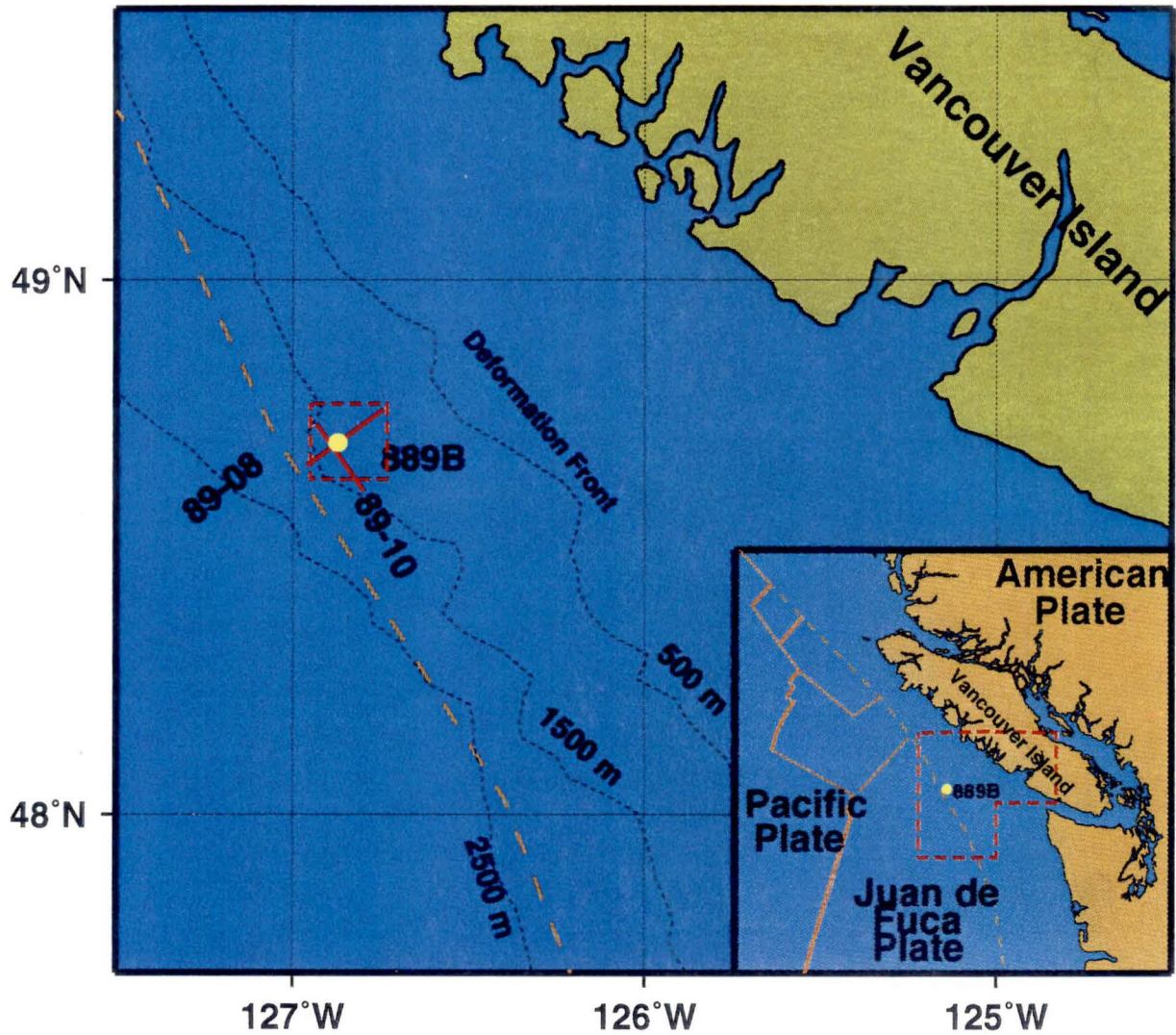


Figure 2.1

Seismic survey location map. SCS and OBS data were collected in a collaborative project between the University of Victoria and the University of Cambridge, 50 km offshore Vancouver Island. The detailed survey was shot in the immediate vicinity of ODP site 889, near the leading edge of the deformation front in 1200 to 1500 m of water. This area is outlined by the dashed red line.

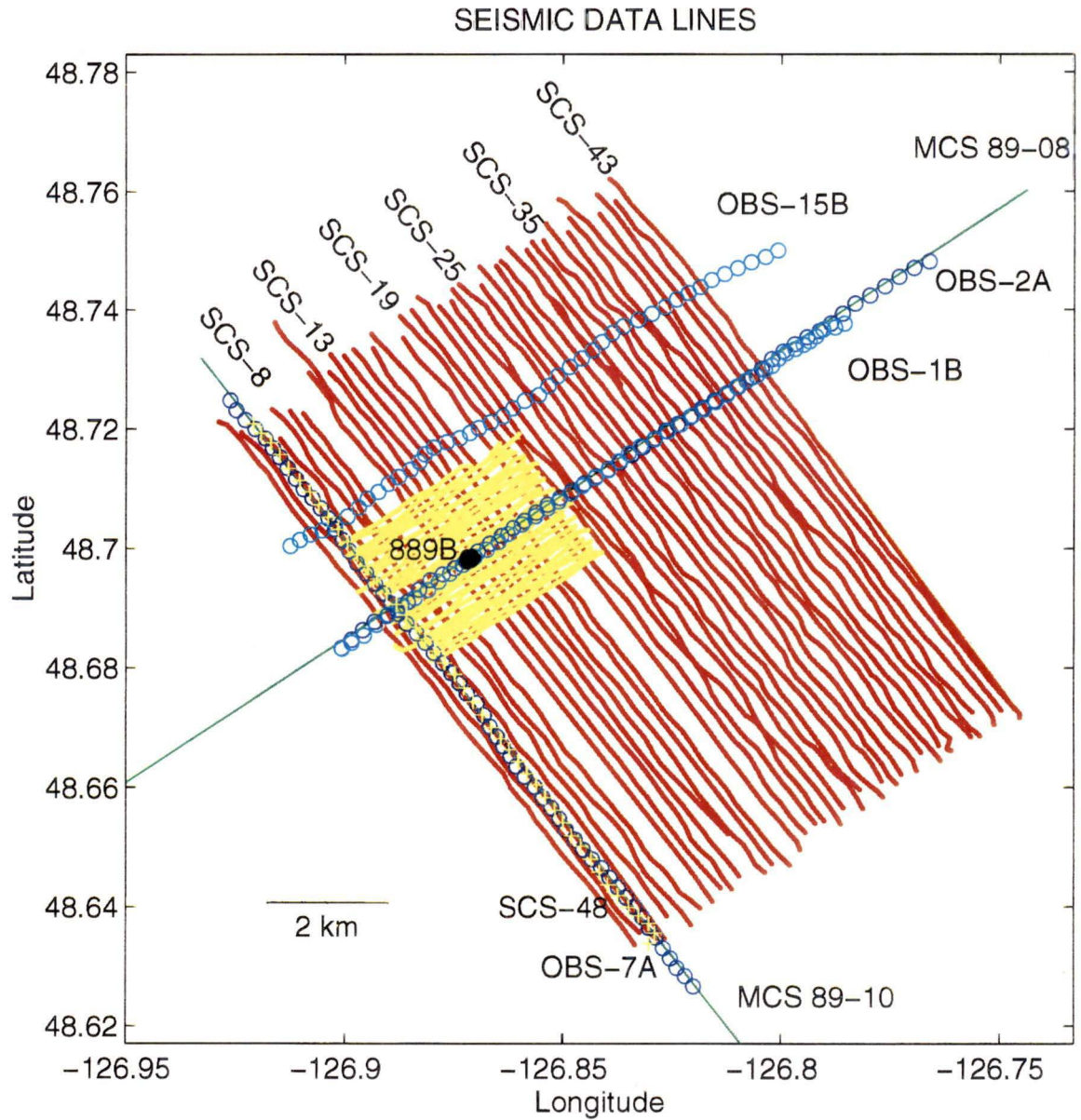


Figure 2.2

Seismic data detailed location map. This figure corresponds to the box around ODP site 889 on Figure 1. Red: SCS lines of GRID A shot with 1.97 L (120 in³) airgun. Yellow: SCS lines of GRID B shot with 0.65 L (40 in³) airgun. Yellow '+' is SCS-48 shot with 0.65 L (40 in³) airgun. Blue: SCS lines acquired simultaneously with OBS acquisition. Green: MCS lines from 1989 survey. 89-08 runs perpendicular to the margin; 89-10 runs parallel to the margin.

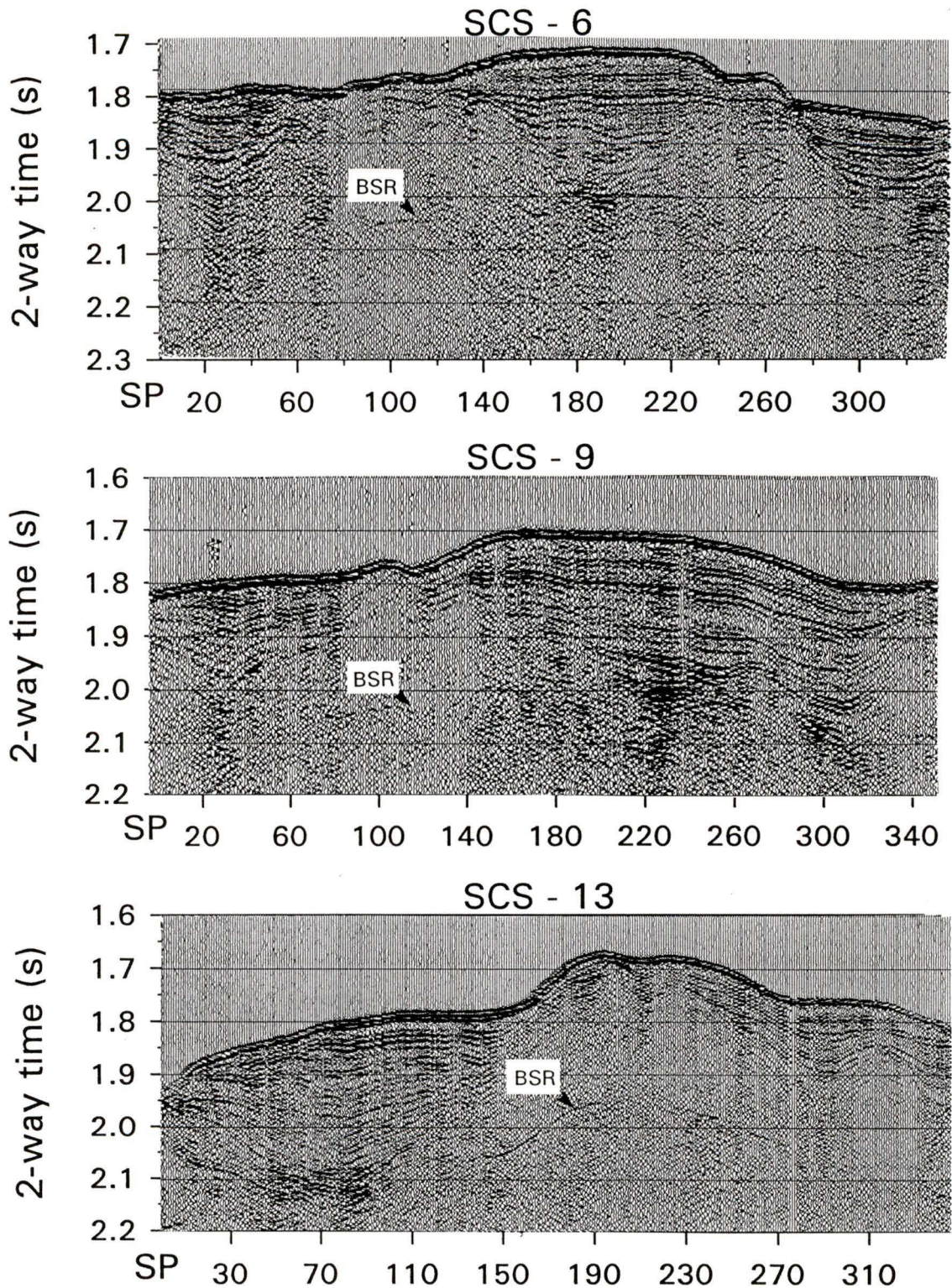


Figure 2.3

Single channel seismic lines SCS-6, SCS-9, and SCS-13 from GRID A. All seismic sections from GRID A are plotted with reversed polarity to emphasize the BSR, and are oriented from NW to SE.

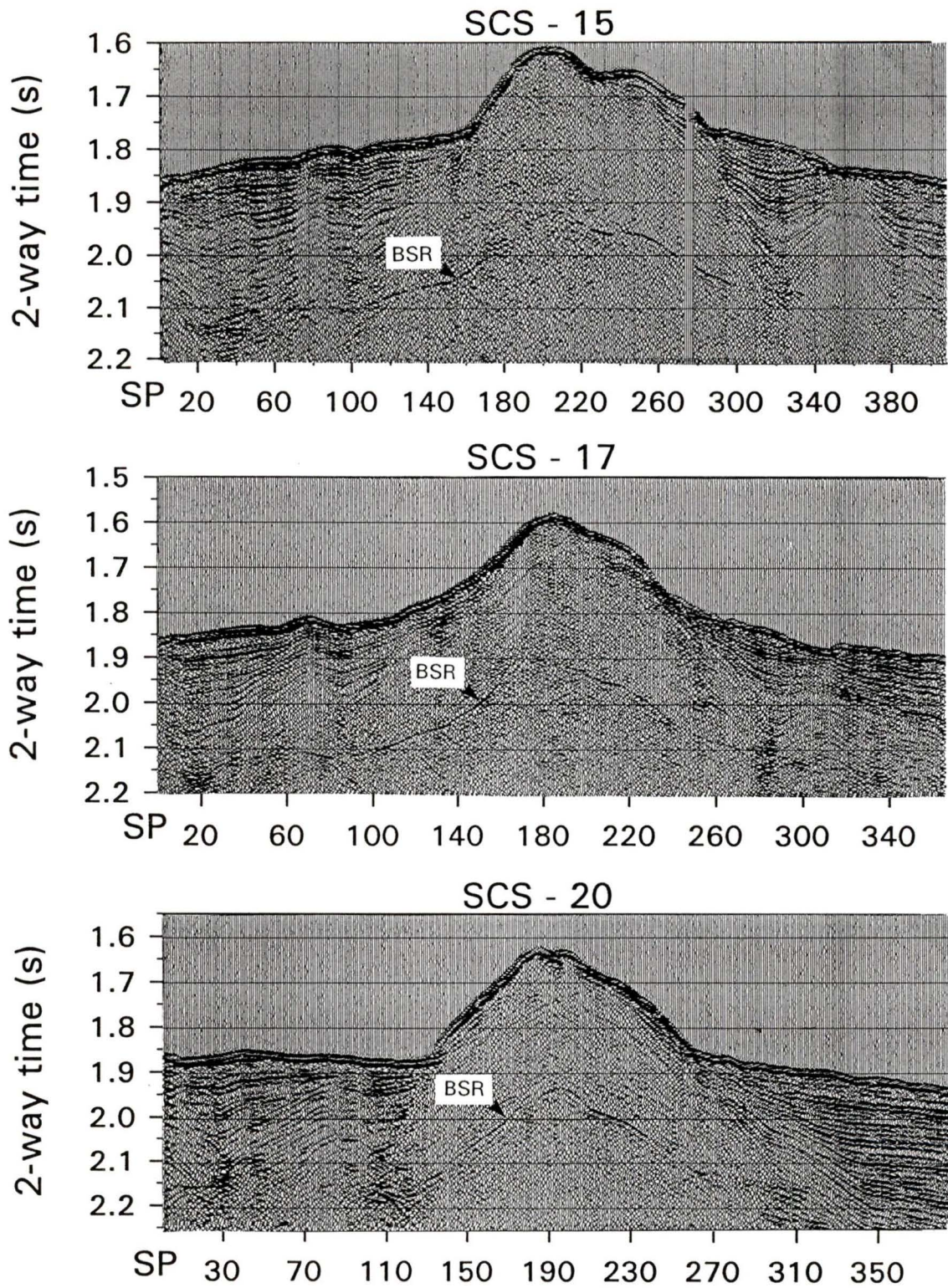


Figure 2.4
 Single channel seismic lines SCS-15, SCS-17, and SCS-20 from GRID A. The strongest and most continuous BSR is observed over the topographic high between lines SCS-12 and SCS-20.

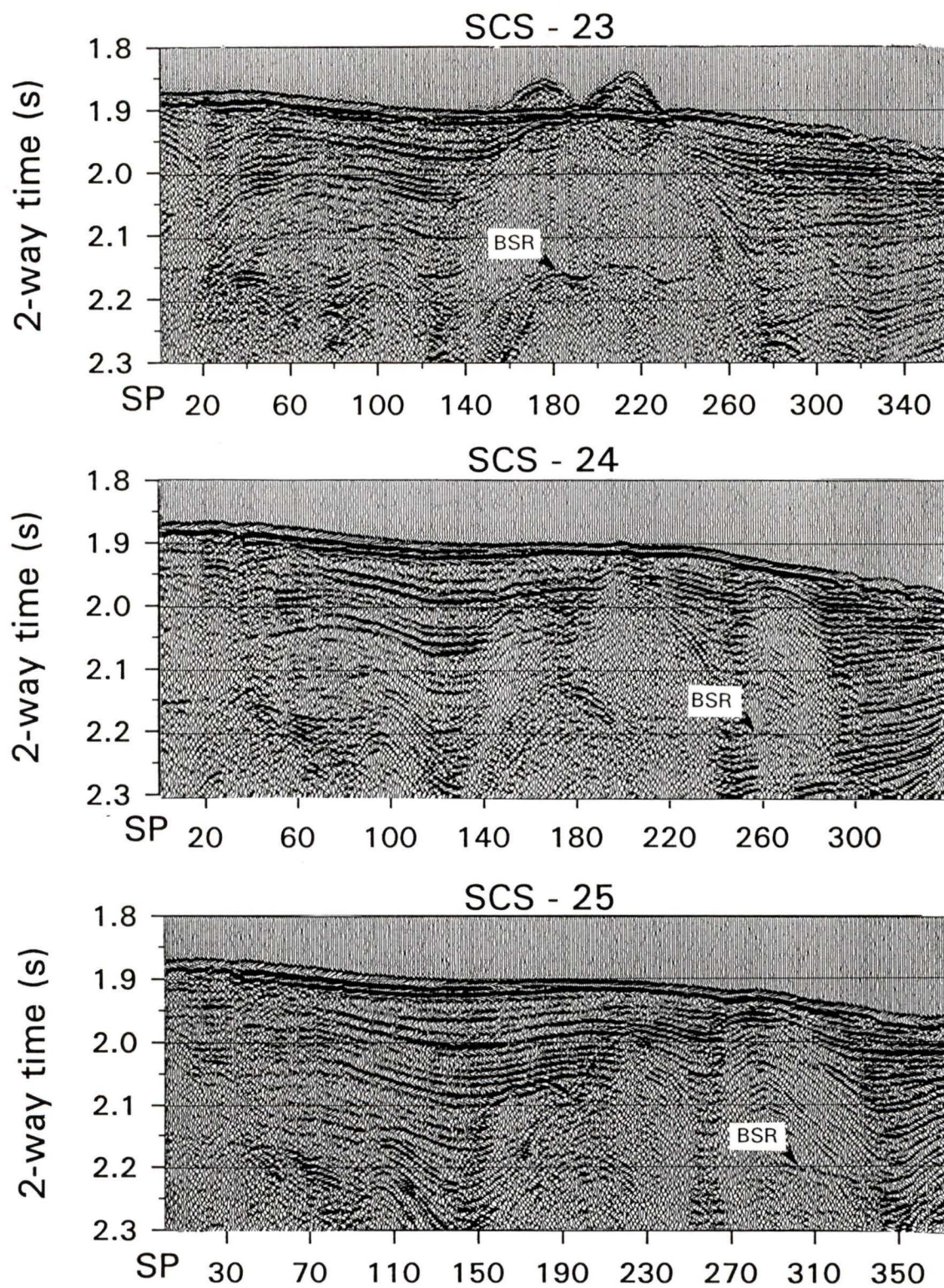


Figure 2.5
Single channel seismic lines SCS-23, SCS-24, and SCS-25 from GRID A. Note off-line reflection observed on SCS-23 from topographic peaks identified on Figure 2.4.

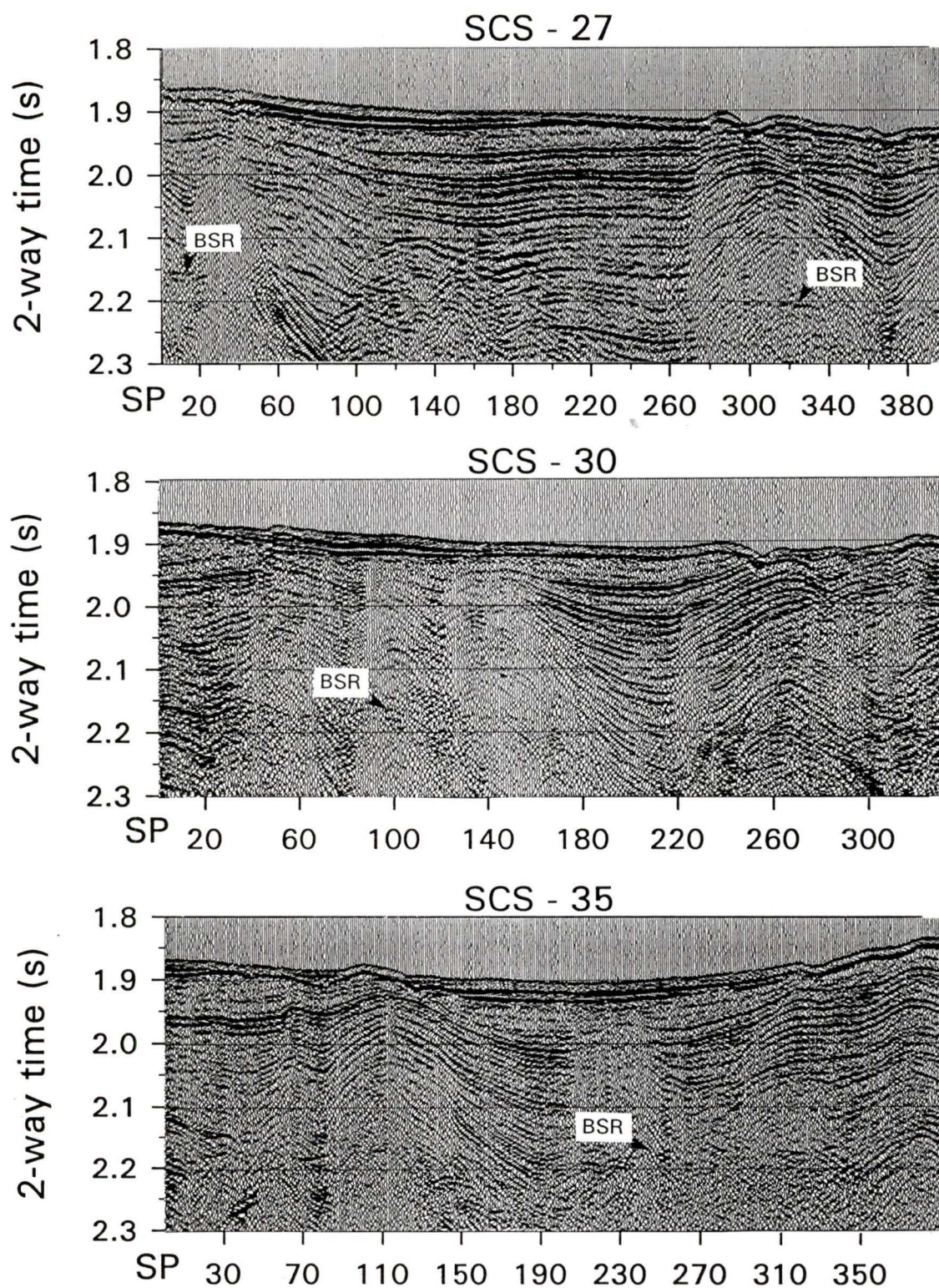


Figure 2.6
 Single channel seismic lines SCS-27, SCS-30, and SCS-35 from GRID A. Note thin layers at seafloor. These have been interpreted as recent slope basin turbidites. No BSR is interpreted over the central portion of these lines. This implies that either, (1) no seismically detectable BSR exists here, or (2) the BSR exists but is obscured by the overlying high amplitude reflectors

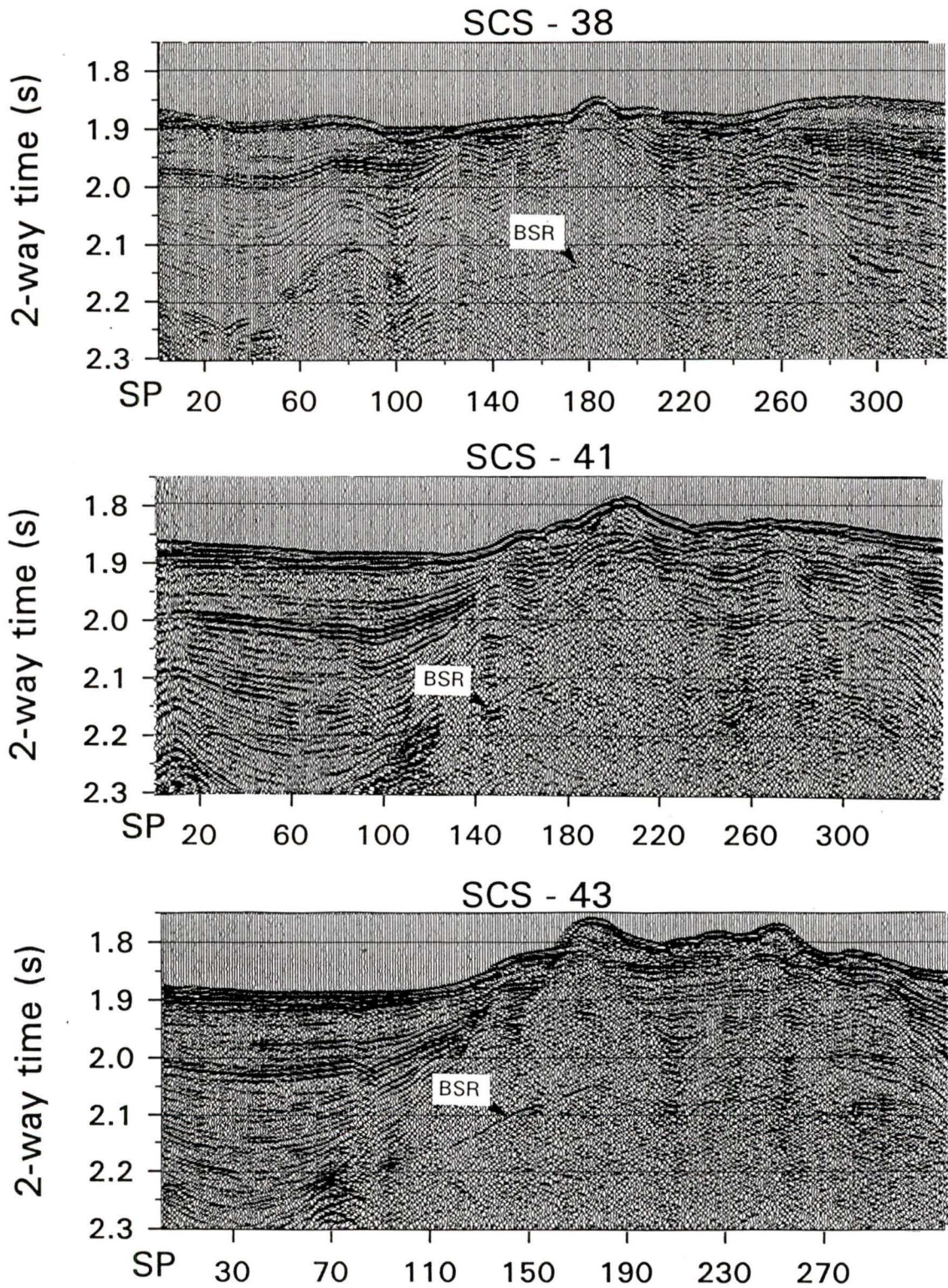


Figure 2.7

Single channel seismic lines SCS-39, SCS-41, and SCS-43 at landward edge of GRID A. Note the resurgence in BSR strength and continuity over this portion of GRID A, relative to the sections shown in Figure 2.6.

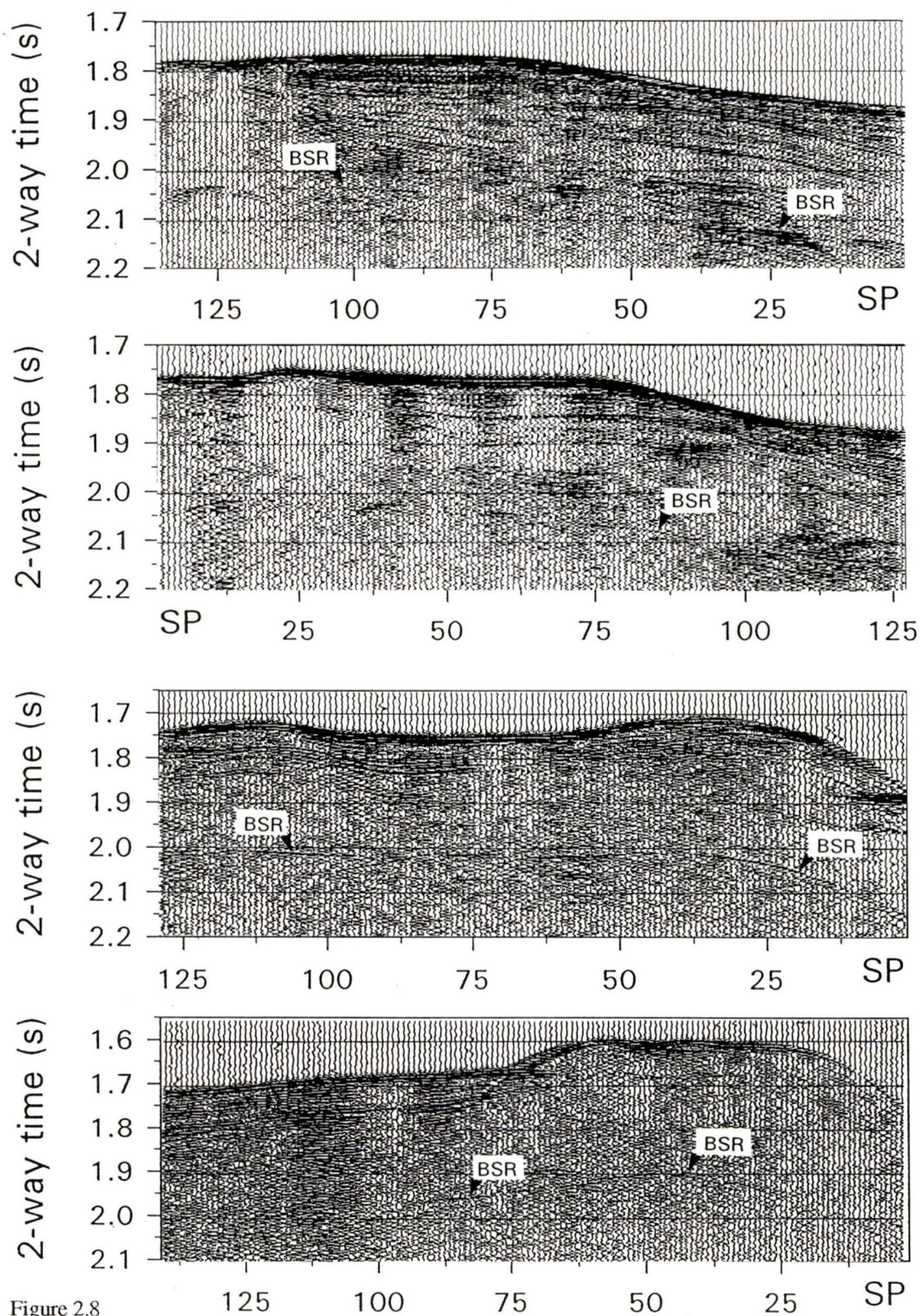


Figure 2.8

Single channel seismic lines from 0.65 L (40 in³) airgun survey, GRID B. Lines shown from top to bottom are, SCS-56, SCS-63, SCS-74, and SCS-83, with the latter farthest south (see Figure 2.2). These sections have a dominant frequency of 150 Hz. All sections are displayed from NW to SE, perpendicular to the 75 Hz lines of GRID A.

across GRID B. We note that the BSR is still observed as a single symmetrical pulse, but that the reflector is less continuous at the higher frequencies of this airgun.

The remaining 450 km of single channel data were acquired simultaneously with the acquisition of Ocean Bottom Seismometer (OBS) data, using the 1.97 L (120 in³) airgun as a source. Four of these lines (OBS-2A, -7A, -1B, and -15B; blue lines in Figure 2.2), were used for cross-line verification of the data in GRID A, and as part of a comparison of the reflection response from different frequency sources.

The 1.97 L (120 in³) airgun produced a dominant acoustic frequency of 75 Hz while the 0.65 L (40 in³) airgun yielded a dominant frequency near 150 Hz. The 75 Hz data were sampled at 2 ms and shots were recorded every 14 seconds for a shot spacing of approximately 35 m. The higher frequency data had a 1 ms sampling rate, and shots were recorded every 10 seconds at a somewhat faster ship speed resulting in a 30 m shot spacing.

2.1.2 Ocean Bottom Seismometer Data

The seismic cruise included two deployments of five digital Ocean Bottom Seismometers (OBSs). In the first deployment (A), the seismometers were spaced 3.3 km apart and 8 lines were shot to offset distances of 10 km. The second deployment (B) used a 1 km seismometer spacing and 15 lines were shot to offsets of 5-6 km. Both deployments used the 1.97 L (120 in³) airgun as the acoustic source.

OBS data were not specifically analyzed in this thesis. However, an interpretation of wide-angle reflections and refractions recorded on several OBSs was carried out by Spence et al. (1995). These results were used in this thesis as an additional constraint for velocity estimates of sediments above the BSR.

2.2 INSTRUMENTATION

2.2.1 Seismic Data Acquisition

Single channel seismic data were acquired using the Pacific Geoscience Centre (Geological Survey of Canada) digital acquisition system. The system was controlled by an IBM 8088 PC and SEG-Y output was written to a 9-track tape drive. The acquisition low-cut filter was set to approximately 5 Hz and the hi-cut filter was set to 200 Hz for the 1.97 L (120 in³) airgun and to 250 Hz for the 0.65 L (40 in³) airgun .

Timing for the experiment was achieved through the use of a Kinematics GOES receiver, which provided ASCII output to a PC of the time of arrival of a trigger pulse. Comparisons with the University of Cambridge clock system, which provided the triggering, indicated stable behavior to within 1 ms. A triggering problem detected on board during the cruise resulted in spurious trigger advances of 100 ms. This problem was corrected on board after the first two days, and on the recorded traces by manual adjustment of the trace header travel times.

SCS data were recorded from a Teledyne Model 178 Hydrostreamer with an active section of 25 m, containing 50 hydrophones. Although poorly constrained, the streamer depth was estimated to be 6 m, and the airguns were towed at approximately 3 m. Source-receiver offset was 30 m for the 1.97 L (120 in³) airgun and 15 m for the 0.65 L (40 in³) airgun. Since the water depth varied between 1200 m and 1550 m over the survey, the data could effectively be considered zero-offset or vertically incident.

A more detailed description of the data acquisition system is given in the cruise report (Spence, 1993).

2.2.2 Navigation

The navigation was recorded using a Trimble GPS receiver integrated with a Furuno LC-90 Mark II receiver for Loran-C. The primary navigation software, Hydronav®, logged

both GPS and Loran-C. Post-cruise processing rationalized the two data sets and smoothed variations in the navigation. Estimates of precision are ± 15 m.

Each trace was tied to its corresponding navigation data during processing. The time of each shot (trace) was well known within each line segment, with a temporal shot-spacing of 14 seconds. The latitude and longitude of the ship, and the time of each measurement, were recorded independently every ten seconds as the ship moved through the survey. A FORTRAN program was written to tie each shot number to its appropriate navigation point within each line segment, using the common times of both shot and navigation point. Because the navigation data sets were very large these were decimated to approximately one measurement every 60 seconds. Where shot-point times fell between recorded navigation-point times, a straight line function was assumed between the two nearest navigation points which bracketed the shot. The time difference between the closest navigation point and the shot was then converted to distance, and a new latitude and longitude was calculated for that shot point. This enabled the seismic data to be plotted as a function of surface coordinates, and is estimated to be accurate within 15-20 m.

2.3 MULTICHANNEL SEISMIC DATA

Data from a multichannel survey conducted over this area in 1989 have also been analyzed. Lines 89-08 and 89-10 (Figure 2.9) were acquired with a tuned airgun array of 30 elements of total volume 128.15 L (7820 in³). This array yielded a dominant seismic frequency of 30 Hz.

The 4 nearest-offset traces were extracted from the raw shot records along the portions of 89-08 and 89-10 which tracked over the detailed survey area of GRID A. With a shot interval of 50 m and a receiver group interval of 25 m, the multichannel data were converted to 100% single channel coverage data with individual traces separated by 12.5 m. Single channel traces from the large airgun array (30 Hz dominant frequency)

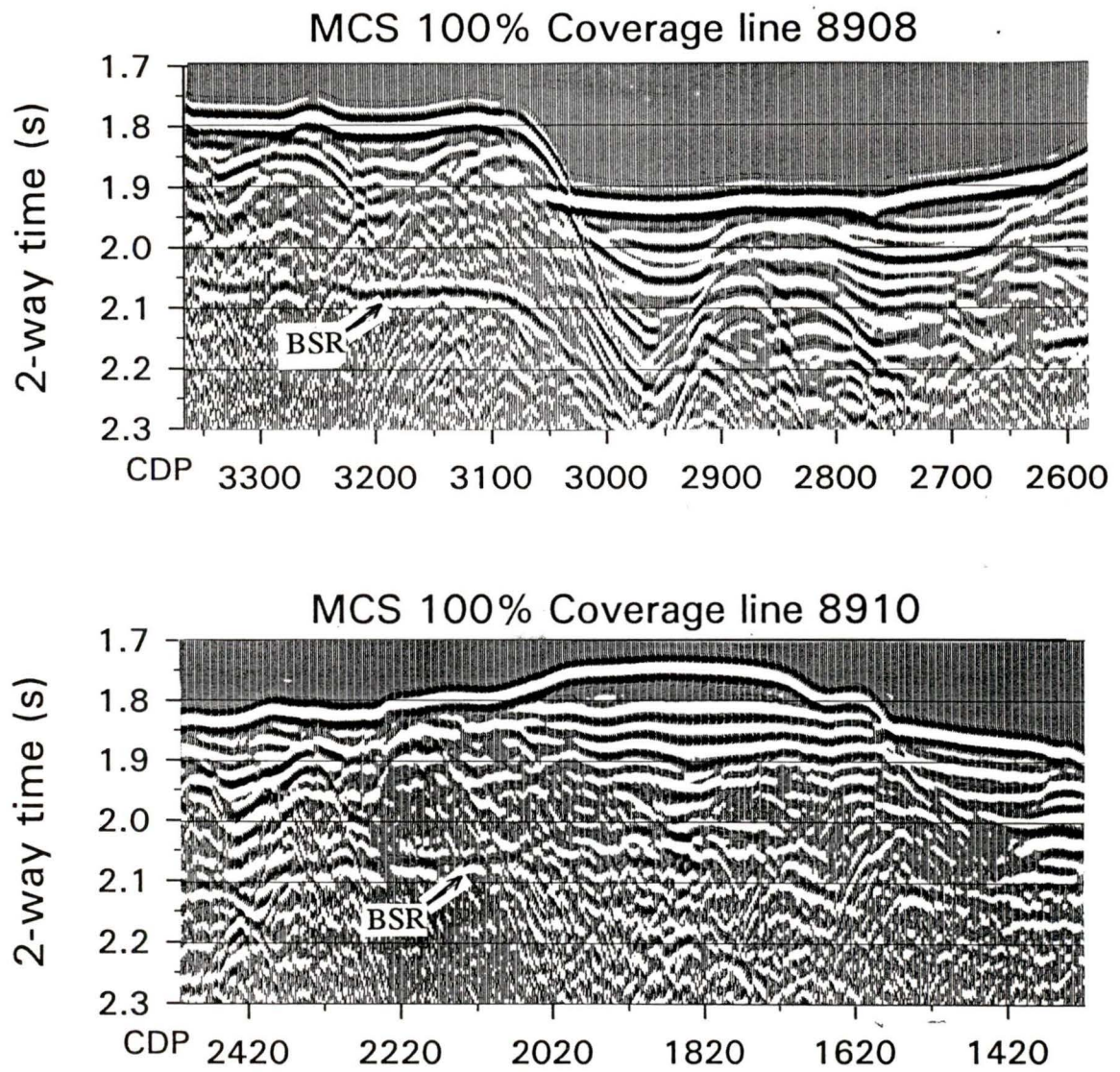


Figure 2.9

100% coverage multichannel lines 89-08 and 89-10. The 4 nearest offset traces were extracted from the raw shot records. Individual reflection points are separated by 12.5 m. Data are "true amplitude" with only bandpass filtering, geometrical spreading, and normal moveout corrections applied.

could then be compared directly to data from the 1.97 L (120 in³) airgun (75 Hz dominant frequency), and the 0.65 L (40 in³) airgun (150 Hz dominant frequency).

2.4 DATA FROM OCEAN DRILLING PROGRAM SITE 889

Detailed downhole velocity and density measurements were acquired during drilling at ODP site 889 (see Figure 2.10). Velocity information was obtained from sonic logs at drillholes 889A and 889B, and from a zero-offset vertical seismic profile (VSP) at 889B. Density estimates for the drillhole are based on both the density log and core sample measurements at 889A (Westbrook et al., 1994; Jarrard et al., 1995).

The high temperature litho-density tool (HLDT) uses a Ce¹³⁷ gamma-ray source and measures the resulting flux at fixed distances from the source. Excessive roughness in the borehole will cause some drilling fluid to infiltrate between the detector and the formation. As a consequence, density readings can be artificially low. Approximate corrections have been applied by Jarrard et al. (1995) by using the caliper data to compensate for unusual borehole roughness.

2.4.1 Sonic Logs at ODP Site 889

Sonic logs were run on holes 889A and 889B (approximately 500 m apart) from approximately 60 mbsf to 260 mbsf. Sonic log velocities range between 1650 m/s and 1850 m/s over the interval from 130 mbsf to the BSR at 224 mbsf. High velocity spikes at 190 and 214 mbsf are interpreted as low-porosity, high resistivity cemented zones (MacKay et al., 1994). Immediately beneath the BSR, the sonic velocity for 889B drops nearly 150 m/s and reaches a minimum value of 1630 m/s at 231 mbsf. This drop in velocity is not seen for 889A.

The long-spaced sonic tool (LLS) was used for the sonic logs on both holes. This instrument measures the time required for sound waves to travel between acoustic transmitters and receivers at offsets of 2.4 m, 3.0 m, and 3.6 m. The raw data reported the

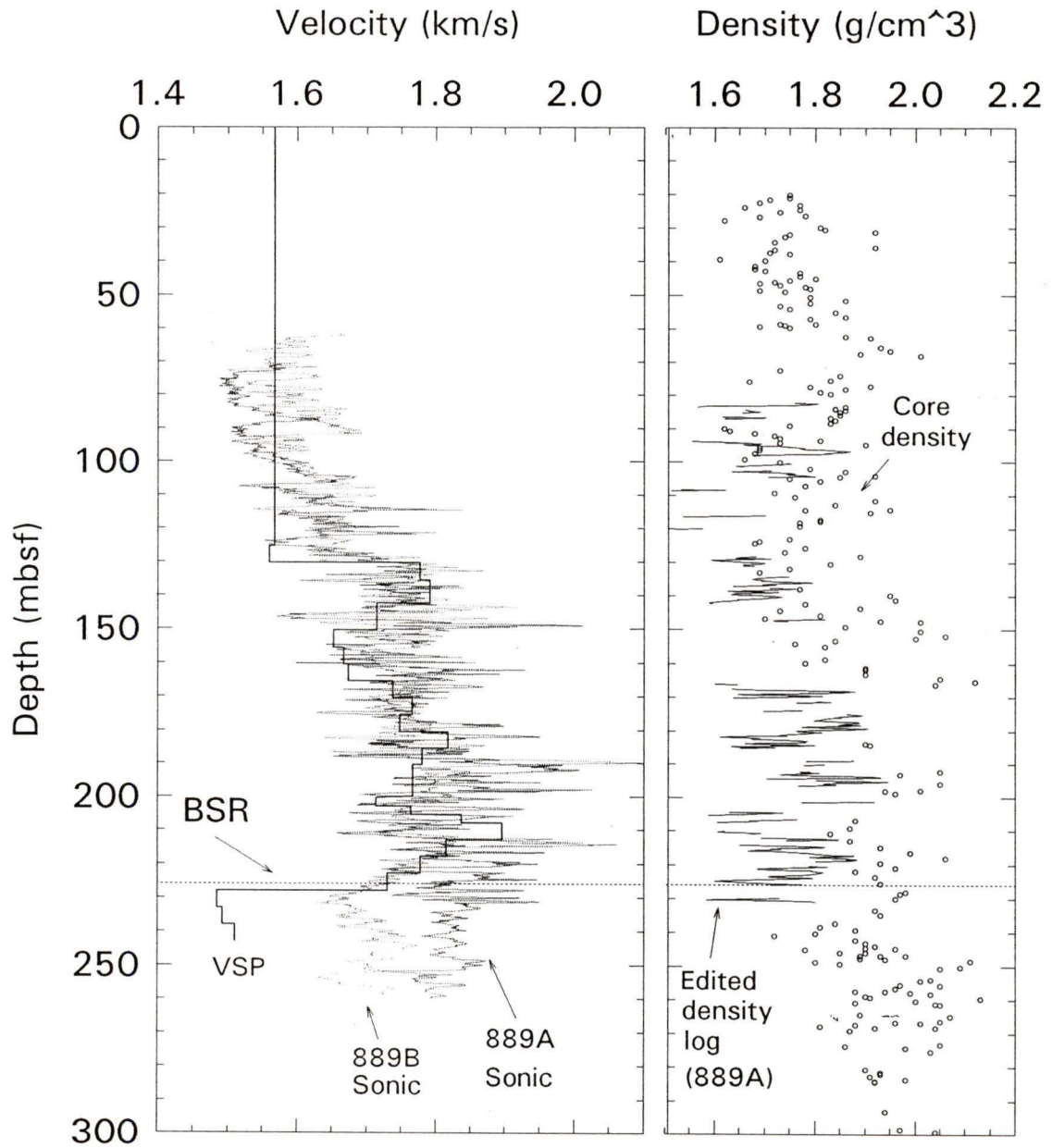


Figure 2.10

Sonic log, vertical seismic profile, and density data from ODP site 889. Sonic logs are from holes 889A and 889B. The VSP was shot at 889B. Density log and core density estimates were obtained from 889A. The BSR is interpreted to occur at 224 mbsf (MacKay et al., 1994). The density log has been edited to compensate for borehole roughness (Jarrard et al., 1995). VSP data are considered to be the most accurate velocity estimates, particularly for the region below the BSR where values deviate from sonic logs.

time required to travel vertically through 0.31 m of formation; these traveltimes are then converted to sonic velocities. Compressional wave velocity is dominantly controlled by porosity and degree of lithification; a decrease in porosity and increase in lithification will both act to increase velocities (Westbrook et al., 1994).

2.4.2 VSP data at ODP Site 889

Vertical seismic profiles provide an unambiguous time/depth relationship from the direct arrival time of a compressional wave at each borehole receiver location within the drillhole. The VSP data at ODP site 889B were recorded with a single-component (vertical) borehole receiver at increments of 5 m as the receiver was moved uphole from 243 mbsf to 125 mbsf. The compressional wave was generated at zero offset with a 4.92 L (300 in³) airgun and a 6.55 L (400 in³) watergun fired in alternate series. Each receiver location recorded between 6 and 20 shots of both air- and watergun source (MacKay et al., 1994).

The resolution for VSP velocity determinations is limited to averaging over 10 m intervals where data quality is good and over 15 m intervals in regions of particularly noisy data. Velocities were not averaged across the region of the BSR since this section clearly represents a strong discontinuity in sediment velocity.

Above the BSR, VSP velocity estimates resemble the sonic log interpretations ranging between 1600 and 1900 m/s. The spikes in the sonic log velocity, which were interpreted as cemented regions, are not observed on the VSP data, most likely due to the limited vertical resolution of the VSP data (10-15 m for VSP vs. 0.6 m for sonic log). Beneath the BSR, the velocity drops by more than twice that recorded by the sonic log, from approximately 1830 m/s to 1515 m/s.

2.4.3 VSP data vs. Sonic data

The VSP and sonic log velocity data agree reasonably well above the BSR, indicating an increase in sonic velocity with depth towards the BSR. However, the two velocity estimates exhibit a pronounced difference for sediments just below the BSR. The velocity structure has strong implications for the lithological structure of the BSR, and constraints on the validity of these estimates is necessary. MacKay et al. (1994) argue that the differences in velocities obtained from the two methods are attributable to the volumes of rock measured by each. Lateral penetration is much less for the sonic log (~0.3 m) than for the VSP (5-10 m), because the dominant frequencies of the sonic log (5-18 kHz) are much higher than the VSP (10-60 Hz).

Contrasts in velocities obtained by the two methods may be influenced by alteration of the formation near the borehole. One such example is the invasion of drilling fluids into the formation. Downhole circulation of sea water required to keep the borehole open for logging will flush out free gas from the near-borehole region and thus increase recorded velocities. Drilling fluid flushing of gas (invasion) is well recognized in the petroleum industry borehole logs. Another problem is that the sonic log will not record velocities lower than borehole fluid (sea water) velocity since the logging tool is designed to only record the fastest traveltimes from source to receiver. We expect gas-bearing sediments below the BSR will have velocities below sea water velocity (1500 m/s), but these will not be recorded with the sonic tool. A third complication is the pronounced differences in sonic log velocities below the BSR recorded in drillhole 889A as compared to those in 889B. Although the two drillhole locations are less than 500 m apart, they differ significantly.

Because of the limitations on the sonic log velocity determination and the observed disparity between the two drillholes, the VSP data are considered to be the most reliable direct measurements of interval velocity. This interpretation is shared by MacKay

et al. (1994). Therefore, modeling parameters and subsequent conclusions are primarily constrained by the VSP velocity estimates for sediments above and below the BSR.

2.5 PROCESSING OF SINGLE CHANNEL SEISMIC DATA

2.5.1 Filtering and Deconvolution

Because a majority of the interpretation required careful analysis of the seafloor and BSR amplitudes, special care was taken to ensure that the "true" amplitudes were preserved. Initial processing of the single channel data (both 75 Hz and 150 Hz) included Hanning bandpass filtering, which does not affect the absolute amplitudes for each shot recorded. The Hanning filters had corner frequencies of 10,15,100,140 Hz for the 75 Hz data and 10,15,190,240 Hz for the 150 Hz data. The data were very good quality with broad amplitude spectra (Figure 2.11), and the signal-to-noise ratio improved with the bandpass filtering performed by this author. The amplitude spectra were calculated with a standard ITA/Insight routine, for a traveltime interval including both the seafloor and BSR so that a better interpretation of the frequency bandwidth over the target reflectors could be obtained.

A strong bubble pulse, which is a phenomenon associated with the use of individual airguns in marine seismic surveys, was identified on the SCS data. When an airgun is fired, a bubble of air is released from the gun at some depth and travels upwards until it breaks at the surface. As this bubble travels upwards it expands and contracts due to the hydrostatic force acting to compress it and its own inherent elasticity forcing it outward again. With each outward expansion of the bubble, a near identical (although smaller amplitude) seismic signal is transmitted. This pulse travels down to the seafloor where, like the original pulse, part of the energy is transmitted and part is reflected upward. The data register a bubble pulse from each impedance contrast in the subsurface. The effect on the seismic section is a series of repeated "bubble" reflections, each arriving at a defined time-lag behind its original reflection, corresponding to the frequency of the

AMPLITUDE SPECTRA

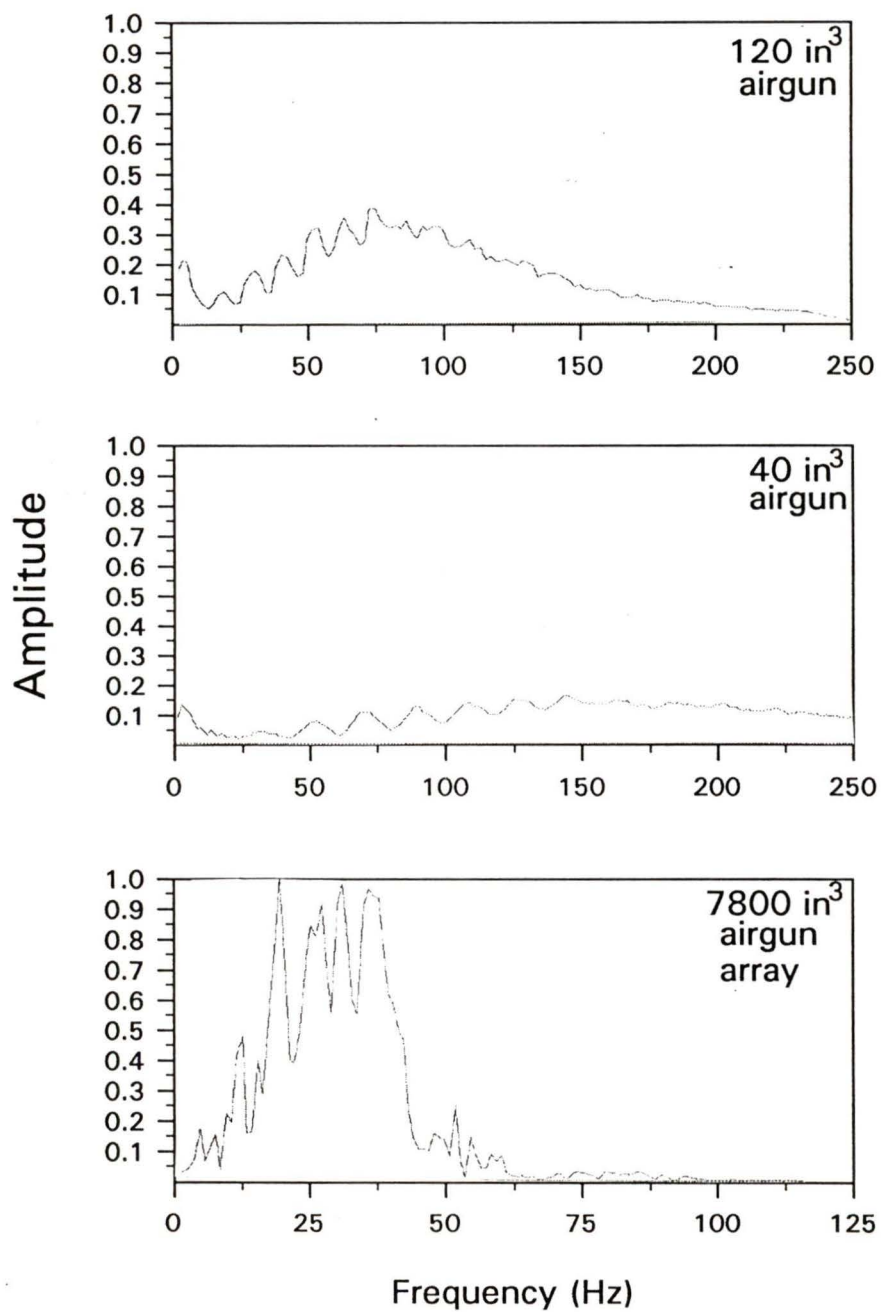


Figure 2.11

Amplitude spectra for typical 30 Hz, 75 Hz, and 150 Hz seismic lines. Corner frequencies for Hanning bandpass filters used on each are:

30 Hz - 10,12,50,70; 75 Hz - 10,15,100,140; 150 Hz - 10,15,190,240

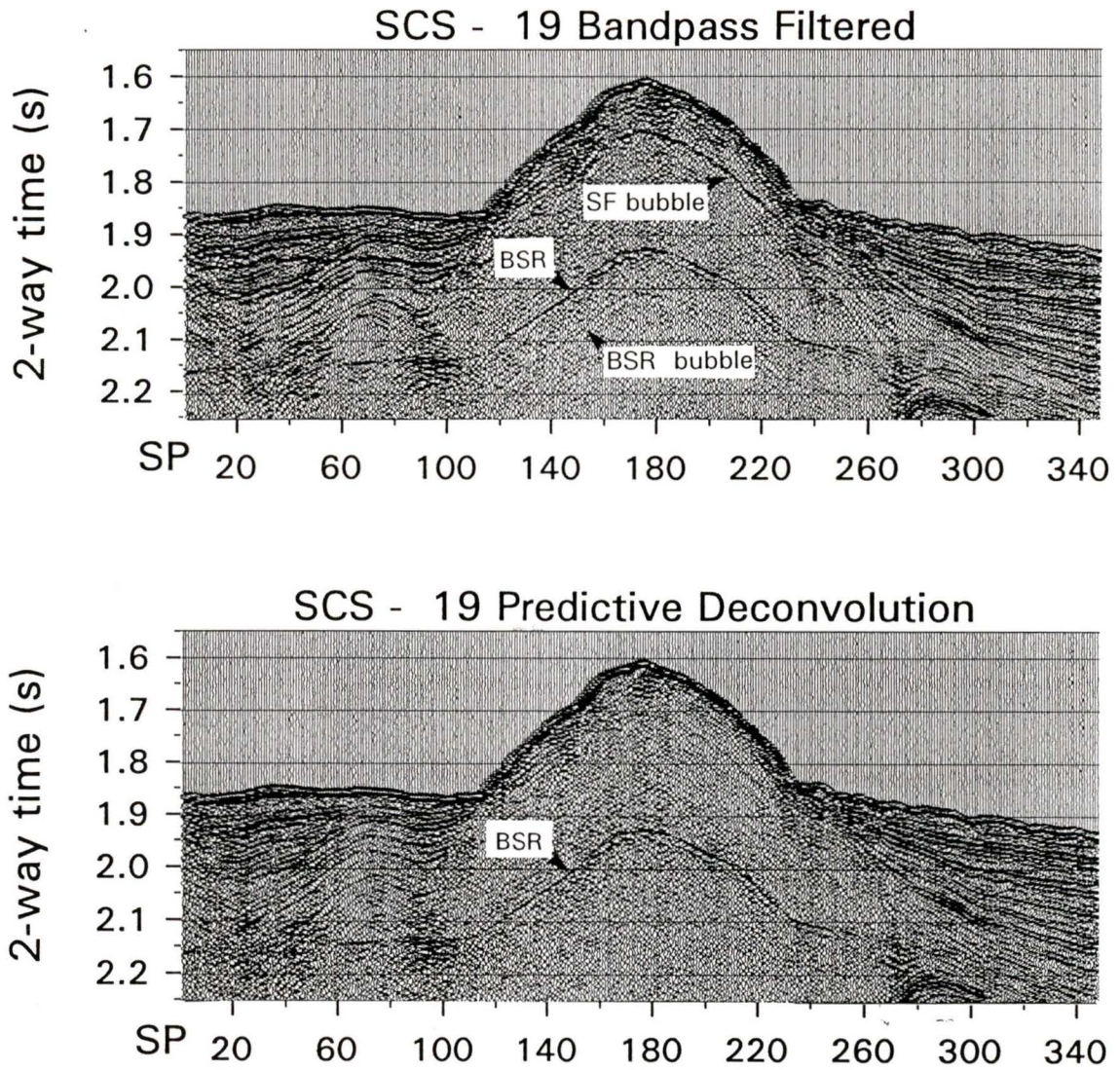


Figure 2.12

Effectiveness of predictive deconvolution in attenuating "bubble" pulse associated with single airgun marine acquisition. Deconvolution gap length averaged 20 ms and operator length averaged 180 ms. Line SCS-19 (1.97 L [120 in³] airgun) is displayed both before (top) and after deconvolution, and clearly demonstrates its effectiveness. Both sections have been bandpass filtered.

bubble expansion (~100 ms for the 1.97 L source and ~75 ms for the 0.65 L source). This series of repeated reflections, particularly from the high amplitude seafloor reflection, tends to obscure smaller amplitude reflectors deeper in the section and subsequently impairs the interpretation process. Predictive deconvolution, following Peacock and Treitel (1969), was very successful in removing the effect of this pulse (Figure 2.12), and in theory this processing step does not affect absolute amplitudes. Nevertheless, predictive deconvolution was only applied to sections for display purposes and to aid the interpretation. All amplitude and subsequent reflection coefficient analyses used amplitudes extracted from only bandpass filtered data to be certain that raw amplitudes were preserved.

2.5.2 Analysis of Data from Large Airgun Array

The large airgun array sections are considered "true amplitude" with processing limited to the application of a Hanning bandpass filter, normal moveout correction, and geometrical spreading correction. The bandpass filter corner frequencies were selected at 10,12,50,70 Hz, and the small moveout correction compensated for the 130 m-285 m source-receiver offset (4 nearest offset traces). Because of the interference effects of the tuned airgun array no bubble pulses were evident in the multichannel seismic records and therefore no predictive deconvolution was required. These data are effectively single channel but are referred to in subsequent discussions as MCS lines to distinguish them from the higher frequency data.

2.5.3 Picking Horizons

Each line of data was interpreted independently using ITA/Insight™ processing software. Three reflection horizons were picked (seafloor, BSR and water bottom multiple of the seafloor primary), using an interactive on-screen display and picking program. For the seafloor reflector, the maximum positive amplitude from within a 10 msec window

centered on the interpreted traveltimes was written to the trace headers. For both the BSR and seafloor multiple, the maximum negative amplitude within a 5 msec window was recorded. Subsequent analysis of amplitude information, including mapping and conversion to reflection coefficients, used MatLab™ numerical analysis software.

Because regional changes in amplitudes were used to make assessments of velocity structure, care was also taken to ensure that the source amplitude was consistent throughout the acquisition. The direct arrival for the 1.97 L (120 in³) source was consistent to within 2% along and between several lines for which variability in seafloor and BSR reflection strength is observed. Cruise log reports indicated that the pressure average of 1750 psi for this airgun was also consistent to within 5% of this average. The 0.65 L (40 in³) airgun showed consistency of the direct arrival amplitude to within 4%.

2.5.4 Mapping Regional Variation

As described in section 2.2.2 each trace in the tightly spaced lines of GRID A has an associated latitude and longitude. Each of these navigation points defines the coordinates of a third value, either traveltimes or amplitude, and together they can be considered coordinates in 3-space where the z-axis may represent depth, amplitude, or any other practical geophysical parameter. For each horizon, this series of coordinates was converted into a regular grid of bins, each bin approximately 200 meters square, resulting in about 3500 bins equally spaced over the survey area of GRID A. The 200 m resolution limit corresponds to the approximate spacing between adjacent lines during acquisition. For each horizon, all traces with navigation points that fall within the coordinates of a particular bin were averaged. Generally 4 or 5 shot points fall within each bin, often from 2 adjacent lines, resulting in a 4- or 5-point ensemble average smoothing function. This type of 2-D smoothing acts to remove some of the trace-to-trace spuriousness without diminishing the resolution provided by the grid design parameters.

Because some of the seismic acquisition lines were separated by more than 200 m, there were initially some "holes" in the bin map where no data were recorded (Figure 2.13 top). To get a smoother representation, an interpolation function was applied whereby the value for an empty bin was obtained from the average of its 8 nearest neighbors. However, a new data point was only generated if there existed a minimum of 4 adjacent bins with data. Shading interpolation was then applied to blend the colors of bins across their divisions for visual continuity (Figure 2.13 bottom). For orientation, MCS lines 89-08 (perpendicular to margin) and 89-10 (parallel to margin), and the location of drillhole 889B are included on all map diagrams of GRID A. Longitude and latitude are defined in decimal degrees.

With the bin format, GRID A data can also be displayed in a pseudo 3-D format, commonly referred to as 2 & 1/2 dimensions (Figure 2.14). The 3-D view was extremely valuable in aiding the interpretation process as it clearly defines the topographic features of the seafloor. The general trend of the seafloor topography compares favourably with the hydrographic/SeaMARC II bathymetry map for this area (see Figure 11A in Hyndman et al., 1994). It is the map view however, that enables us to more clearly evaluate the regional diversity of amplitude, reflection coefficient, sediment velocity, and ultimately hydrate concentration.

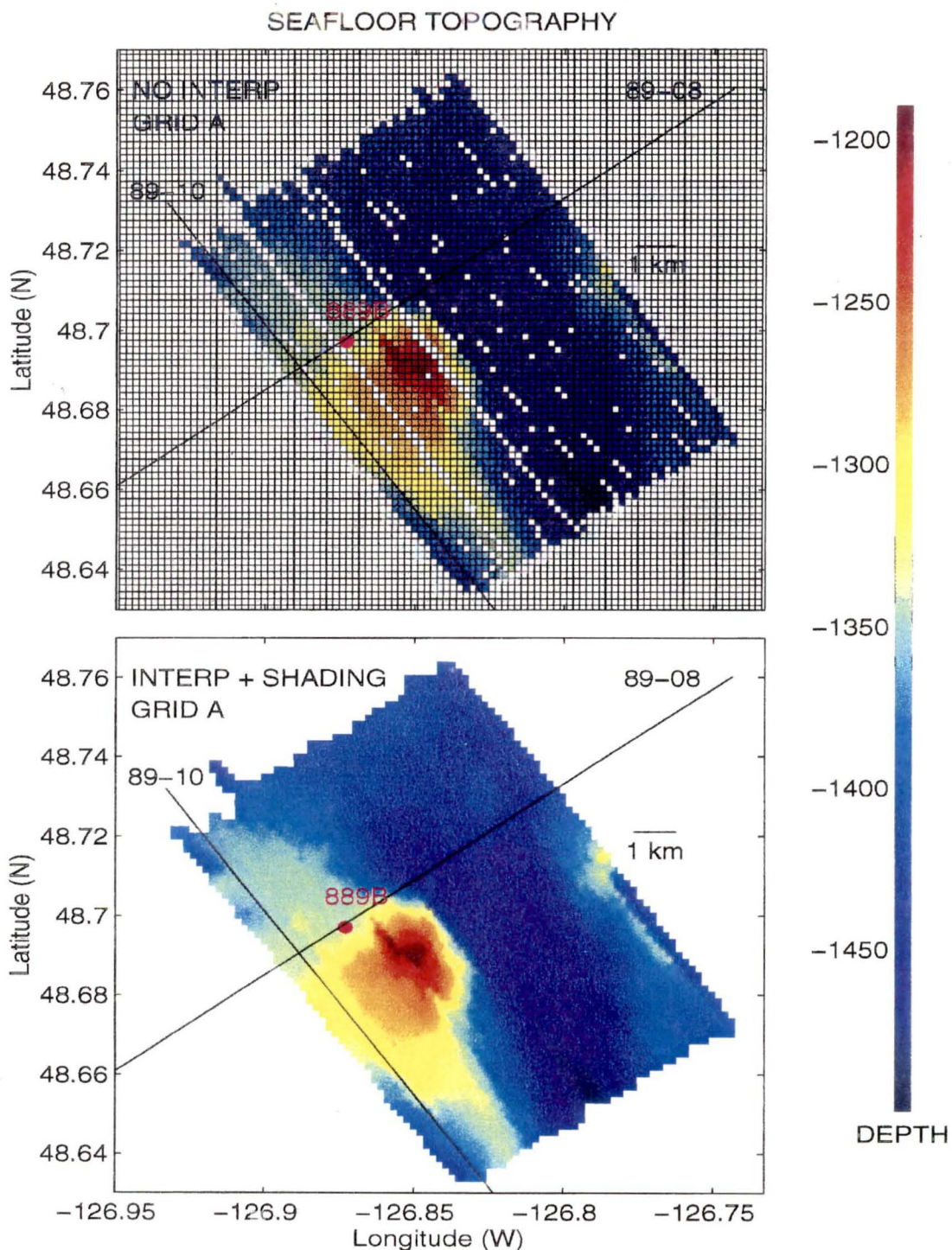


Figure 2.13

Map representation of seafloor topography from the tightly spaced 2-D lines of GRID A. Recorded navigation for each shot point (trace) in the survey is used to transform the data into 3500 equally spaced bins. The average value of all traces whose navigation coordinates lie within the boundaries of a bin is assigned to that bin. Bins are approximately 200 m square, and average 4 traces each. Because some lines were not equally spaced, there existed holes in the bin map (top). An interpolation function was run to fill in the missing bins with an average of the 8 nearest neighbors, provided at least 4 neighboring bins were not empty. Colors were then smoothed between bin divisions for visual continuity.

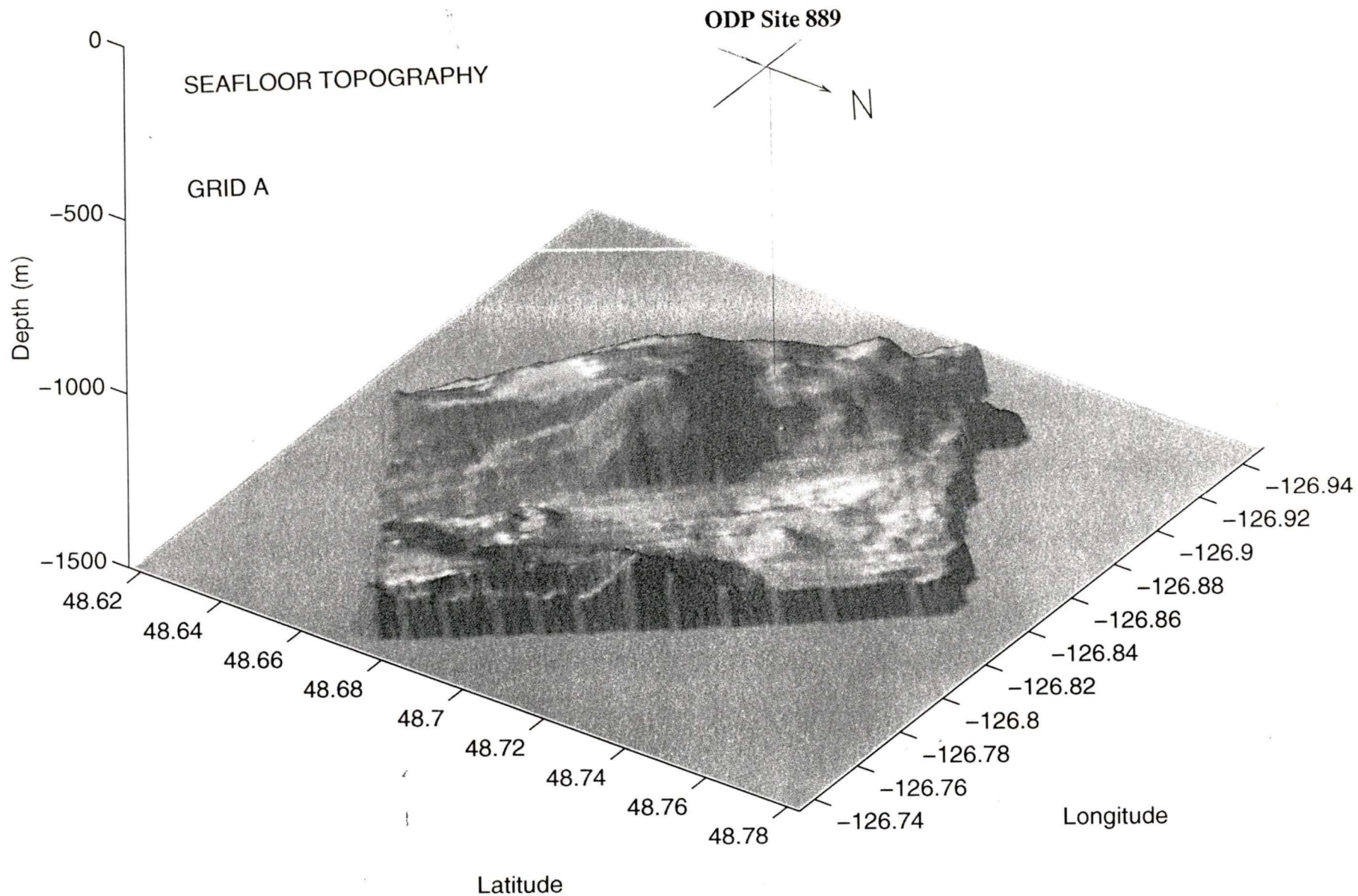


Figure 2.14
 3-D view of seafloor topography from tightly spaced 2-D lines of GRID A. Note the margin-parallel linearity of the thrust structure and the closure about the topographic highs. Highest point is 1190 mbsl, lowest point is 1495 mbsl.

CHAPTER THREE AMPLITUDE ANALYSIS

3.1 AMPLITUDE

Seismic amplitudes are a measure of the energy received from an acoustic reflection and are proportional to the voltage output by a hydrophone, which senses pressure variations. However, the absolute amplitude of a reflection is only significant if the absolute amplitude near the source is known, and this is a difficult quantity to measure. Rather it is the ratio of reflected amplitude to source amplitude that is significant. We will quantify reflection magnitude by converting amplitudes to reflection coefficients in section 3.2. At this point we will reserve discussion to only the regional variability in amplitude strength and will show that this conveys important information about the lithology.

3.1.1 Seafloor Amplitude

Seafloor amplitudes (SFA) for GRID A are shown in Figure 3.1. The largest amplitudes in the survey can be identified in an elongated oval centered at -126.86° longitude, 48.70° latitude, with a particularly strong region north and west of the drillhole. Amplitudes decrease smoothly as we move away from this oval, tapering off to a background value between 25% and 40% of the maximum. Another region of high amplitude along the extreme seaward edge of the survey is identifiable as a linear feature paralleling the margin, of at least 300 meters width but which likely extends beyond the survey. A slight increase in reflector strength (60% of maximum) is also observed near the extreme landward edge of the survey centered at approximately -126.79° , 48.71° .

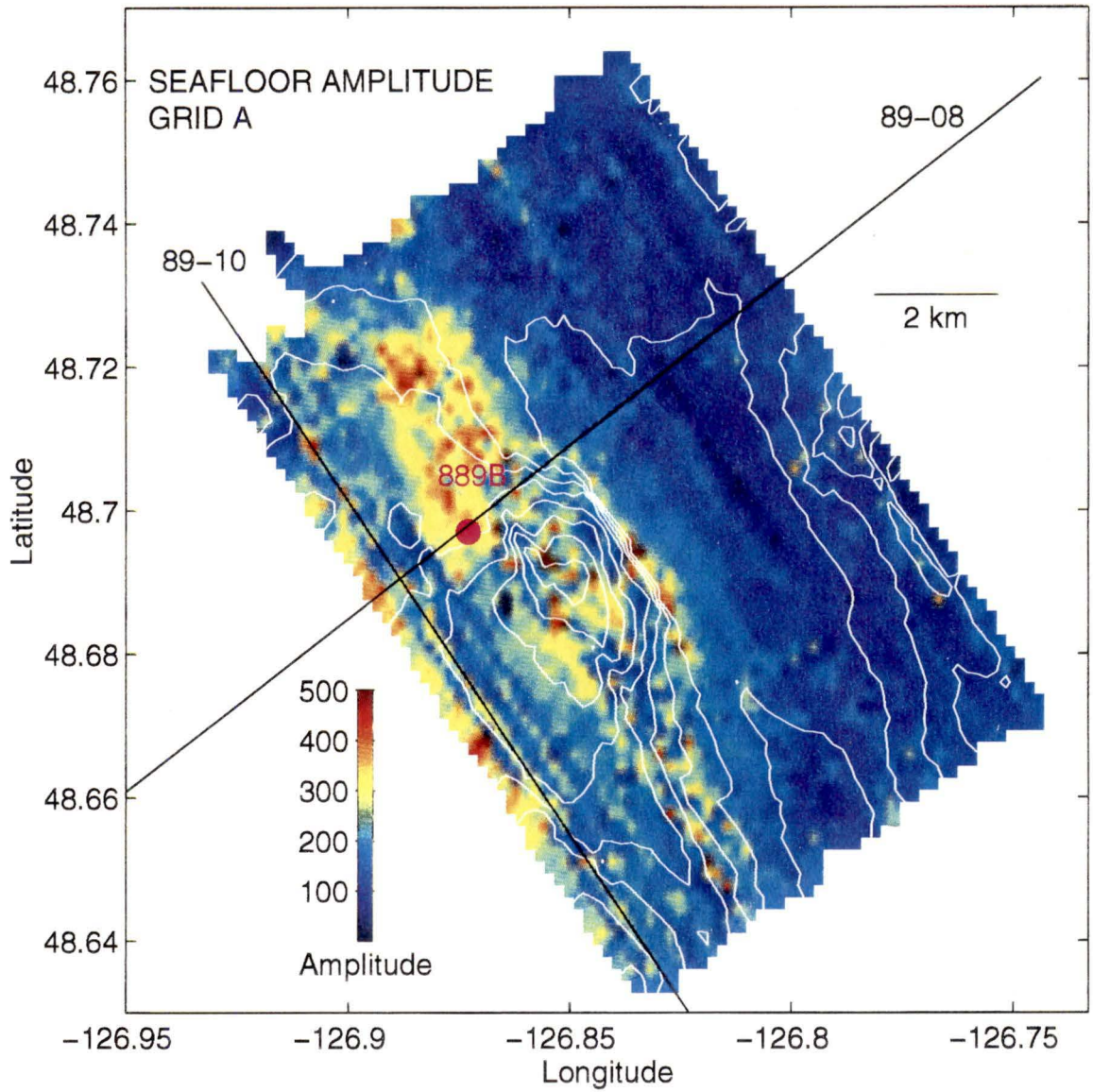


Figure 3.1
 Seafloor amplitude map created from SCS lines of GRID A. Amplitude magnitude is displayed in the lower left hand corner. Topographic contours are included and describe maxima at -126.85°, 48.64° and -127.79°, 48.7°. A correlation between topography and amplitude strength is observed. MCS lines 89-08 and 89-10, and ODP drillhole 889B have been labeled for orientation.

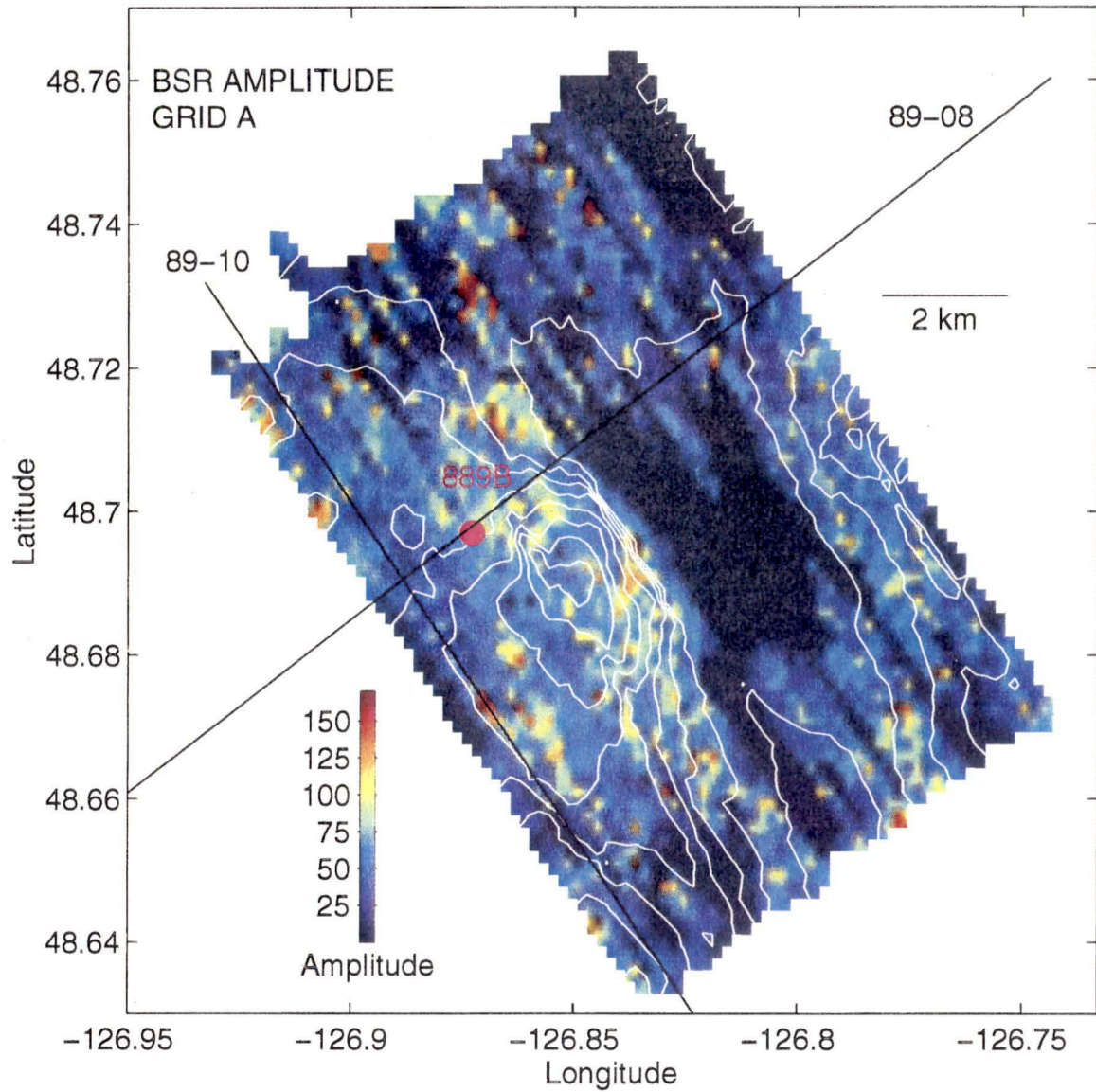


Figure 3.2

BSR amplitude map created from GRID A. Amplitude magnitude is displayed in the lower left hand corner. Amplitudes above 175 are considered spurious due to their localized nature and have been set to the upper limit of 175. Sections colored dark blue correspond to regions of the survey where no BSR is interpretable. Local highs in BSR amplitude correlate moderately well to highs in seafloor topography.

3.1.2 BSR Amplitudes

Figure 3.2 shows the bottom simulating reflector amplitudes for GRID A. Although the impedance contrast at the BSR returns negative values for amplitude, absolute values are displayed for ease of comparison with the seafloor.

Amplitudes greater than the largest scale value (175) are assigned a value of 175. These are considered spurious values since they occur infrequently and discontinuously across the survey. Regions colored dark blue have magnitude 0 and correspond to sections of single-channel lines where no BSR was interpreted. In these areas, either the impedance contrast is not sufficiently large for a BSR to be seismically definable, or a BSR exists but is obscured by overlying high-amplitude reflections which lie within the depth interval where a BSR is expected (i.e. 200 mbsf - 240 mbsf). These reflections often exhibit a pronounced degree of deformation (see Figure 2.6).

As was observed for the seafloor, the largest BSR amplitudes are identified in an elongated oval centered at -126.84° , 48.69° . A second local maximum can be seen along the landward edge of the survey extending south from MCS line 89-08 through to the SE corner of the map. Both of these features are correlated to local highs in seafloor topography.

3.1.3 Cross-line Analysis

For both the seafloor and the BSR a relative low in amplitude strength is observed as a linear feature paralleling the margin. This amplitude trough runs the length of the survey with its northwestern edge centered at -126.85° , 48.75° . Because the seismic lines of GRID A were also shot parallel to the margin, it might be argued that the decrease in both seafloor and BSR reflector strength in the trough is due to a proportional decrease in source amplitude along the single-channel lines sampling this area. To check this initially, the cruise logbook was reviewed to identify any systematic variations in airgun pressure for the

lines of GRID A. Airgun pressures averaged 1750 psi and varied by less than 5% across GRID A.

A more convincing argument for the legitimacy of the amplitude map data comes from analysis of lines directed near-normal to those of GRID A. The seafloor amplitude variation of SCS cross-lines OBS-15B, OBS-2A, and OBS-1B were examined (Figure 3.3). Lines 2A and 1B are coincident with MCS line 89-08. Line 15B parallels 89-08 and lies approximately 3 km to the north (see Figure 2.2). The cross-lines were shot with the same source as the lines of GRID A (120 in³ airgun), and the horizontal scale is in km NE of MCS 89-10. Average airgun pressures for line 2A were slightly higher than for lines 1B and 15B (1875 psi vs. 1700 psi). However, along each of these lines, the logbook showed airgun pressures remained within 5-7% of the line average. The difference in overall magnitude between the A-deployment and B-deployment lines might be attributed to the small difference in average airgun pressures described above.

The variation in amplitude exhibited along these lines correlates well to what is observed on the seafloor amplitude map, not only spatially, but also in terms of relative amplitude strength. For example, each cross-line exhibits the same characteristic drop in amplitude at a distinct "break point". This break is identified at approximately 2 km east of 89-10 on line 15B and at 1.6 km on lines 2A and 1B. On average, magnitudes NE of the break drop off to less than 40% of those SW of the break and this ties well to what is observed on the seafloor amplitude map (Figure 3.1). Southwest of the break, a less substantial drop in magnitude is clearly identifiable at -0.1 km on lines 2A and 1B, with a resurgence in strength farther SW. For line 15B a drop in magnitude can be seen 0.5 km NE of 89-10, although SW of this drop, magnitudes are more widely scattered. On Figure 3.1, this low amplitude feature is correlatable to the linear region of moderately low amplitude near the western edge which becomes wider north of MCS 89-08, and in the vicinity of line 15B amplitudes identified from GRID A data are also more variable.

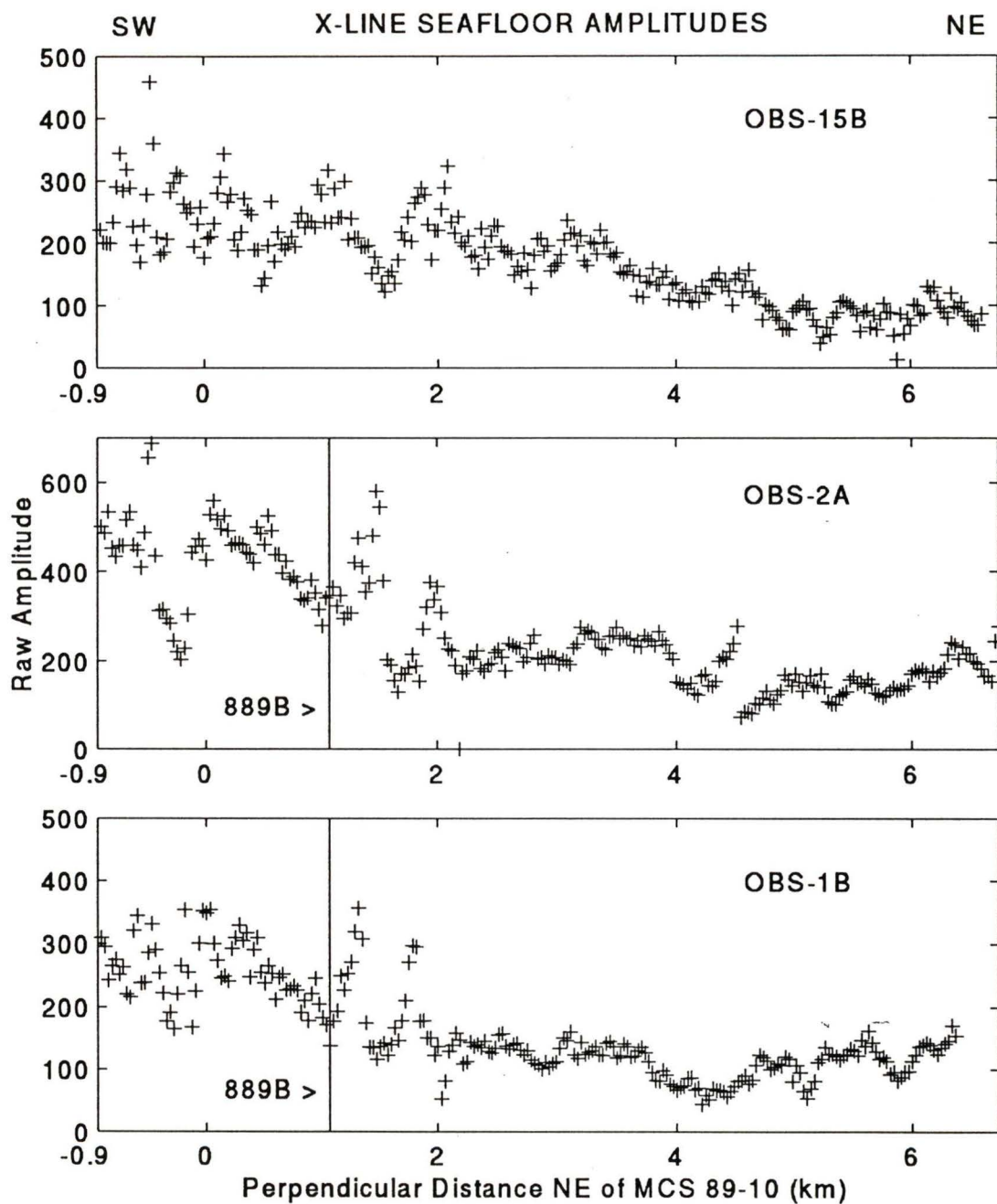


Figure 3.3

Cross-line seafloor amplitudes. Lines OBS-15B, OBS-2A, & OBS-1B were shot perpendicular to the SCS lines of GRID A. Lines 2A and 1B are coincident with MCS 89-08, and line 15B lies 3 km to the north (see Figure 2.2). Each of these exhibits a distinct decrease in amplitude which is spatially correlatable to the decrease in amplitude observed in Figure 3.1. This indicates that changes in source amplitude strength along GRID A are not responsible for observed decreases in seafloor and BSR reflector magnitude.

This cross-line analysis clearly demonstrates that the observed amplitude features in GRID A are representative of real changes in reflectance at both the seafloor and BSR.

3.2 CONVERSION OF AMPLITUDES TO REFLECTION COEFFICIENTS

Reflection coefficients (RCs) provide a quantitative analysis of reflector strength and impedance contrast. Consequently, a conversion of raw amplitude to RC allows data from independent acquisition systems to be compared and contrasted readily. This property is important for our data set since the average "raw" amplitude values of the MCS data differ from the SCS data by several orders of magnitude, and the SCS data acquired with the 1.97 L (120 in³) airgun differ from the data acquired with the 0.65 L (40 in³) airgun by approximately a factor of 3.

The seismic reflection coefficient, as defined by Yilmaz (1989), is:

$$RC = \frac{(I_2 - I_1)}{(I_2 + I_1)}, \quad (3.1)$$

where I_1 and I_2 are the sonic impedances of the top and bottom layer at a seismically reflecting interface. Impedance is simply the product of a layer's sonic velocity (v_p) and its bulk density (ρ):

$$I = v_p \rho. \quad (3.2)$$

Reflection coefficients represent the ratio of reflected amplitude to transmitted amplitude. Their values range between -1 and 1 and their sign indicates whether the second layer has a higher or lower impedance than the first. A lower impedance in the second layer results in a negative RC.

3.2.1 Warner's Method

In the following method of RC calculation, referred to hereafter as Warner's method (Warner, 1990), RCs are calculated from the ratio of a reflector's water bottom multiple (WBM) amplitude A_{mult} , to its primary amplitude, A_{prim} .

Figure 3.4 is a cartoon drawing of the raypaths for both the seafloor primary and WBM reflections. The primary reflection makes only one contact with the seafloor along its path, therefore its amplitude varies linearly with seafloor RC. The WBM contacts the seafloor twice, and the sea-air interface (RC = -1) once, in its path to the receiver. We expect that WBM amplitudes will be negative in sign, and that their magnitudes will vary proportional to the square of seafloor RC. These results are summarized in the equations at the bottom of Figure 3.4, and suggest that the 4:1 ratio between maximum and minimum amplitudes exhibited at the seafloor should translate to a 16:1 max./min. amplitude ratio for the WBM.

In equation form Warner's method is,

$$RC_{Warner} = \frac{c_1 \cdot A_{mult}}{A_{prim}}, \quad (3.3)$$

where c_1 is the correction factor for spherical divergence, which we assume is proportional to traveltime. Thus c_1 is equal to 2 since the multiple reflection has a traveltime exactly twice that of the primary.

For the seafloor, RCs were calculated directly in this way. For the BSR, we assume its reflection coefficient can be calculated by comparing its amplitude to the seafloor amplitude. Dividing both sides of equation (3.3) by A_{prim} we obtain a coefficient that will convert amplitudes to reflection coefficients. The conversion coefficient expression for Warner's method is:

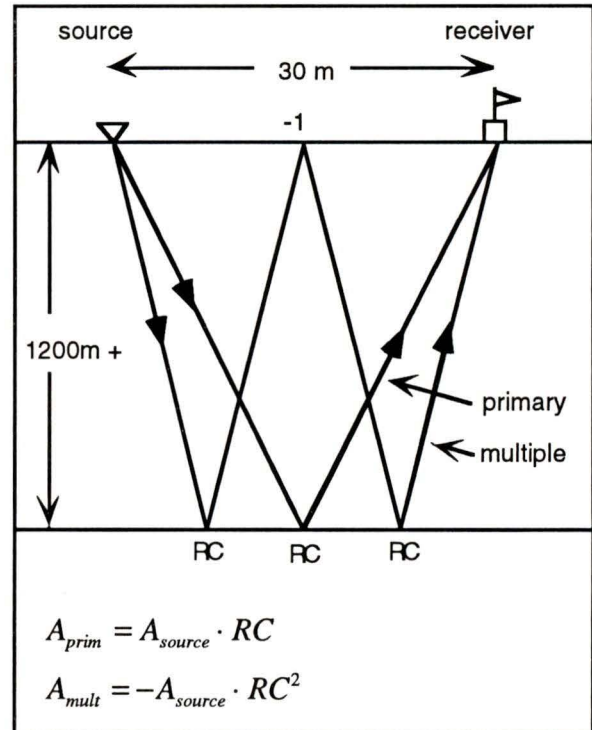


Figure 3.4
Seafloor primary and water bottom multiple raypaths for single-channel seismic acquisition. The equations describe what effect the seafloor interface (assumed a simple reflector between two half spaces) will have on the primary and multiple amplitudes. For a well-behaved seafloor, a change of x in the primary amplitude should result in a change of x^2 in the multiple amplitude.

$$ConvCoef = \frac{c_1 \cdot A_{mult}}{(A_{prim})^2}, \quad (3.4)$$

To calculate the BSR RCs we then simply multiply the conversion coefficient by BSR raw amplitude and another geometrical spreading correction factor, c_2 . Equation (3.5) describes the amplitude to RC conversion for the BSR,

$$RC_{BSR} = c_2 \cdot ConvCoef \cdot A_{BSR}, \quad (3.5)$$

where the correction factor here is proportional to the ratio of BSR travelttime to seafloor travelttime, approximately 2.1/1.8 for the majority of the survey.

3.2.2 Trace-by-Trace Warner's Method Application

Several single-channel lines from GRID A were analyzed on a trace-by-trace basis to observe the variation of RCs generated from the local amplitudes of the seafloor, the seafloor multiple, and the BSR. With no smoothing applied to the data, a wide variability in amplitude strength was observed between adjacent traces. Due to this variability, averages of broad groupings of similar values were taken to be representative of spatial variations in reflector strength.

Figure 3.5 depicts typical results for this trace-by-trace method. Immediately apparent is the wide scatter of RC values particularly for the BSR. For the seafloor, RCs range from less than 0.05 to just under 0.4. We have identified four "groupings" of reasonably similar values, and the average for each of these groupings is indicated by the solid line. Moving along line SCS-19 from NW to SE the average RCs are 0.12, 0.21, 0.11, and 0.15.

For the BSR, RCs range from 0 to as high as -0.12. However, RC values stronger than -0.10 might be considered spurious as they are infrequent and isolated. Again moving from NW to SE, interpreted average RCs for defined groupings are -0.039, -0.055, -0.041, and -0.065.

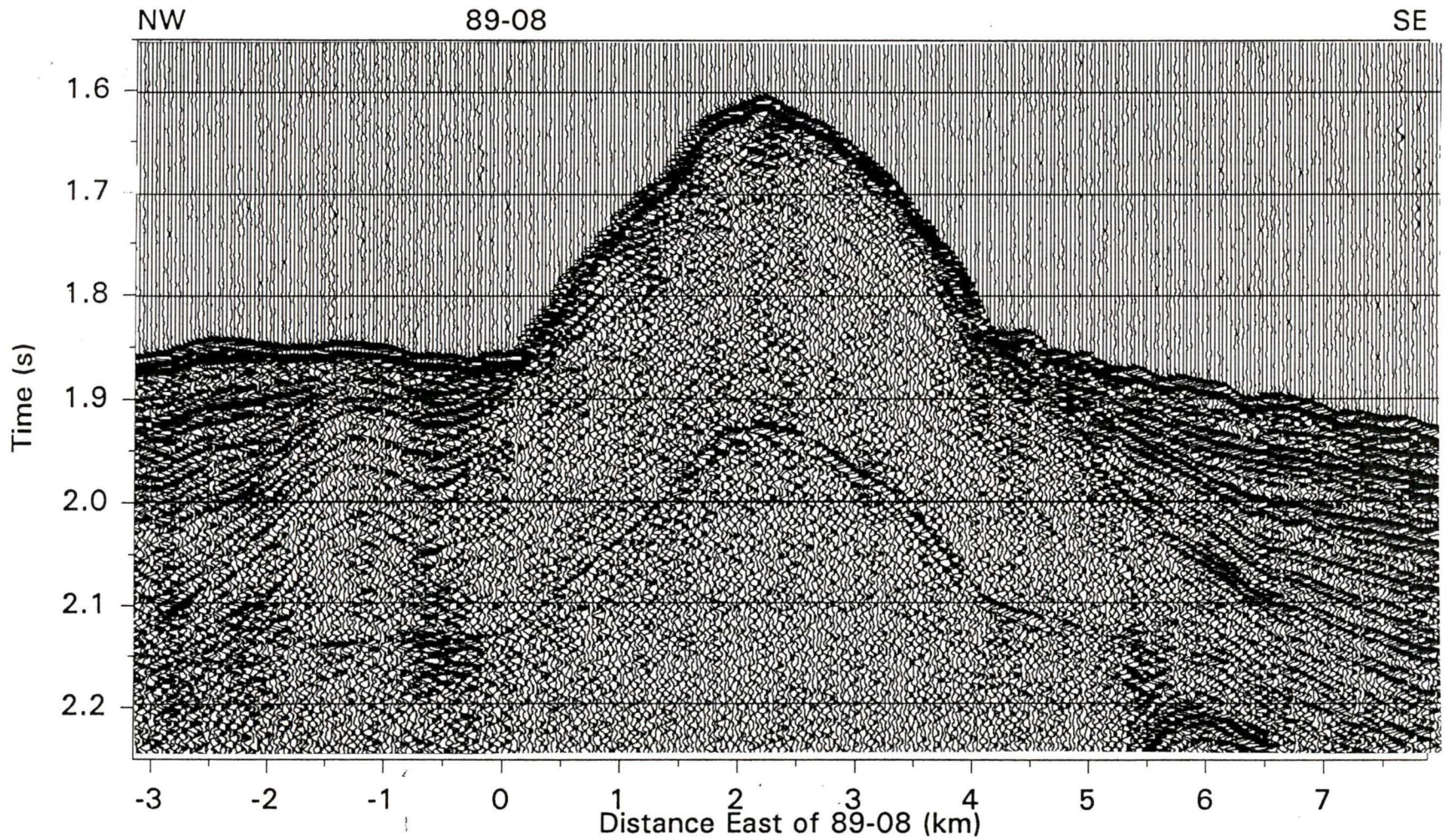


Figure 3.5
 Trace-by-trace reflection coefficients for SCS-19. This line exhibits the strongest amplitudes and greatest continuity for the BSR. Horizontal scale is in km east of cross-line 89-08, where SE is taken to be the positive x-direction. The BSR is clearly see beneath the topographic high but is less apparent beneath the flanks of this high. Note the onlapping of recent sediments SE of the topographic high. Seafloor amplitude is much lower here, but this is not reflected in the locally-calculated RC values. (continued on next page)

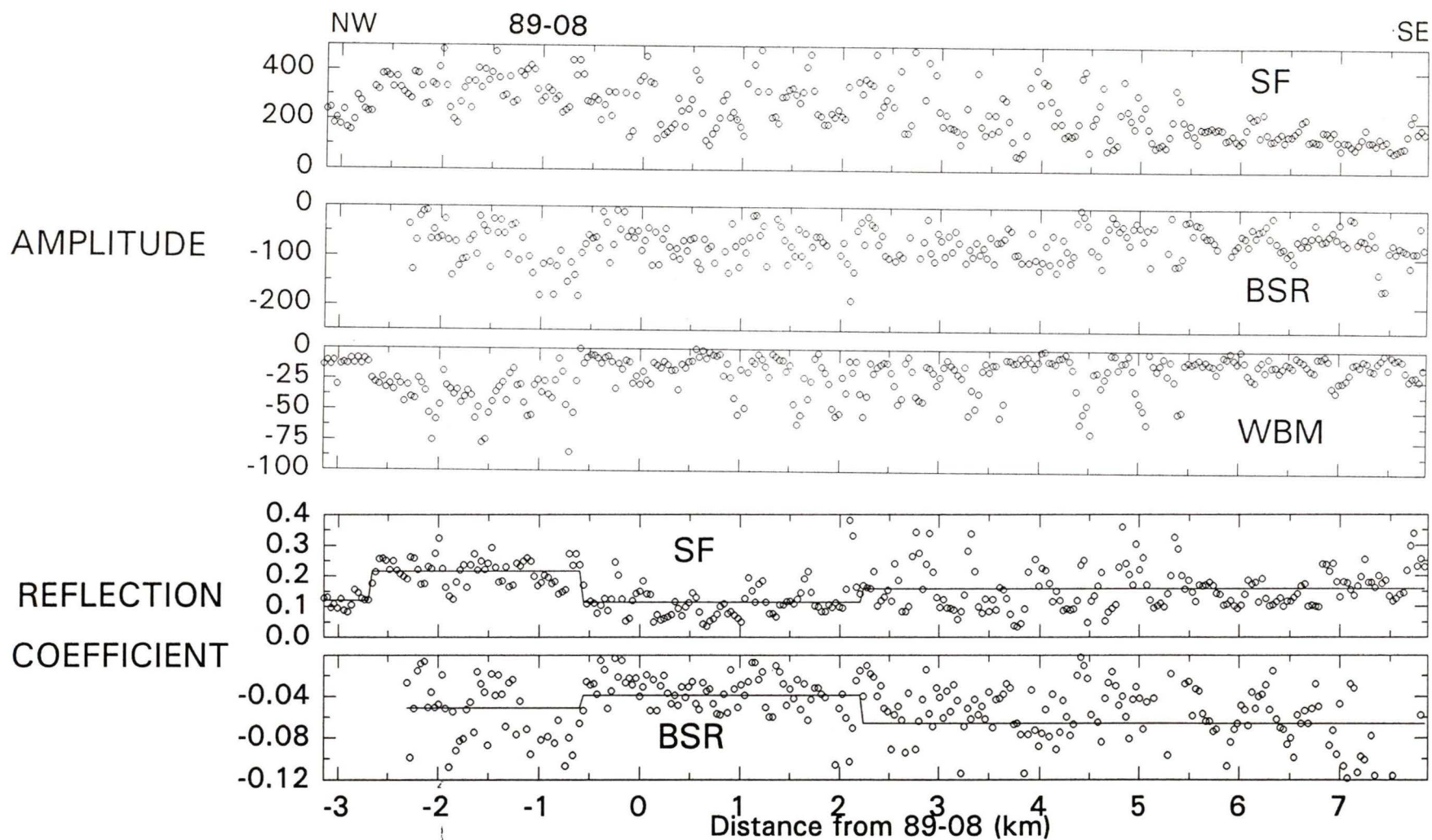


Figure 3.5 continued

Amplitudes and trace-by-trace reflection coefficients for SCS-19. The top three plots show raw amplitudes for the seafloor, BSR, and WBM reflections. The two lower figures are the corresponding reflection coefficients generated using equations 3.3, 3.4, and 3.5 for each trace. Due to wide scatter in the data, RCs are divided into sections of approximately similar value. The break in BSR amplitude and RC values indicate the one section of this line where no BSR was interpreted.

3.2.3 Bin-by-Bin Warner's Method Application

To obtain a clearer picture of regional variation in the locally-calculated RC values and reflector strength, Warner's method was applied to the bin-map representation of GRID A. Conversion coefficients were generated for each bin following equation (3.4), and then applied to the seafloor and BSR amplitudes to obtain a "local" reflection coefficient. The bin map representation of WBM amplitudes is shown in Figure 3.6.

Figure 3.7 shows the results of the bin-by-bin Warner's method of amplitude to RC conversion. RCs for the seafloor (left-hand figure) are remarkably uniform, averaging between 0.2 and 0.25 across the majority of the map. Regions of the map correlatable to relatively high amplitudes appear to be diminished in terms of their resultant RC value. Often they are of similar magnitude to RCs generated over regions of amplitude minima. An area of high RC is observed centered at -126.83° , 48.72° but it can not be correlated to a regional increase in seafloor amplitude. Instead, this RC high is the result of an anomalously high region of WBM amplitudes (see Figure 3.6).

Similar inconsistencies between raw amplitudes and RCs are exhibited for the BSR map (right-hand figure). Again a local maximum in RC can be found at -126.83° , 48.72° , yet no corresponding high in BSR amplitude is observed at this location. A linear feature along the eastern perimeter of the BSR map exhibits a local maximum in RC magnitude that *does* correlate to moderately large raw amplitudes. However, this appears to be the only similarity between the amplitudes and bin-by-bin generated RCs.

Regional variation in reflector strength for both the seafloor and the BSR was lost in the conversion from amplitude to RC using the bin-by-bin application of Warner's method. The cross-line analysis (section 3.1.3) suggests that the amplitude information corresponds to the true trace reflection strength, and is representative of real changes in lithology. As such, these changes should be manifested in the conversion to RCs. Because the regional variation exhibited in the amplitude data did not translate in the conversion to

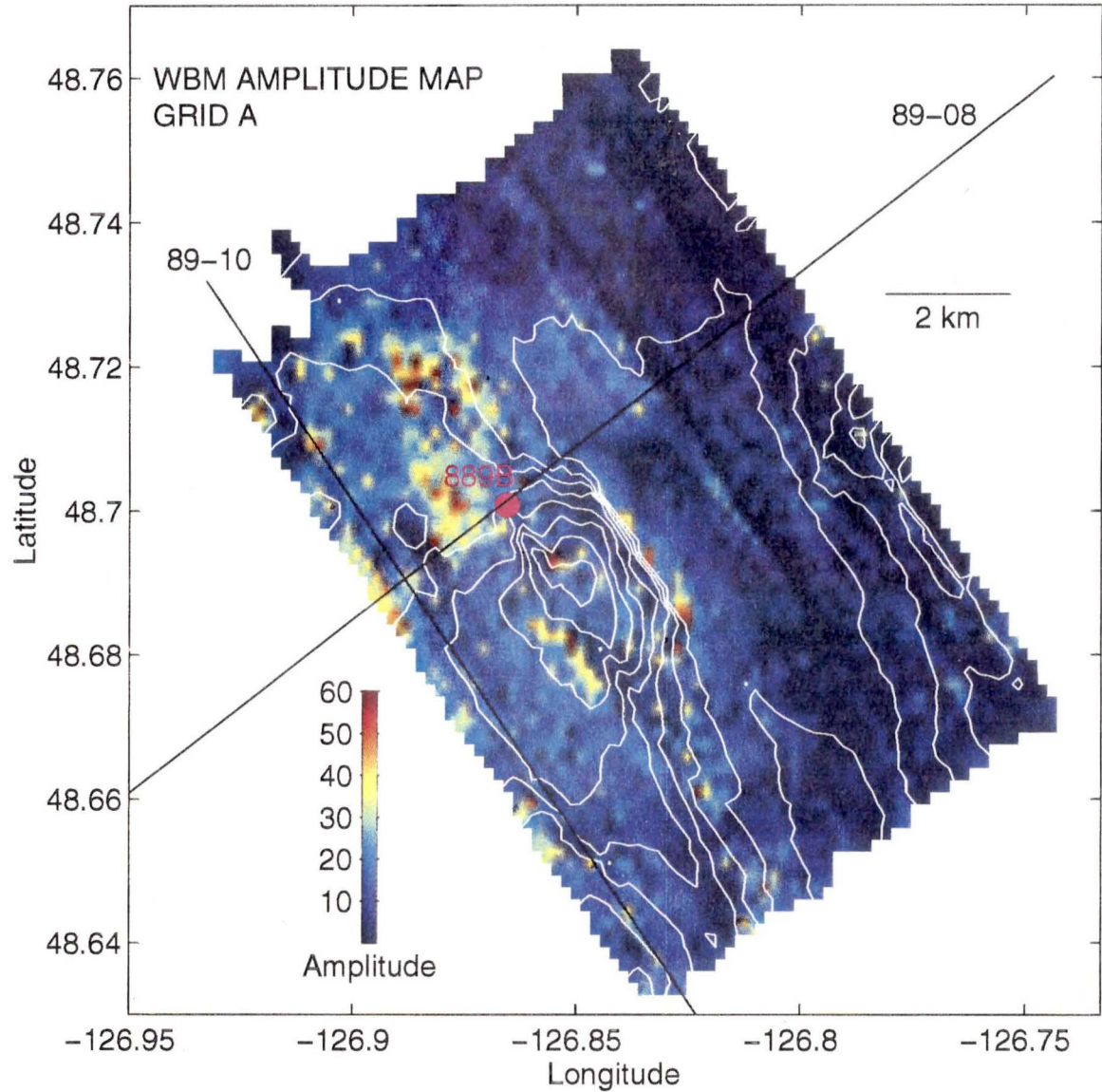


Figure 3.6

Seafloor water bottom multiple amplitude map for GRID A. Amplitude magnitude is displayed in the lower left hand corner. As expected, regional variation in amplitude follows the same pattern as the seafloor primary reflection. However, the observed maximum to minimum amplitude ratio (4:1) is inconsistent with what is predicted from geometric ray theory. WBM amplitudes over the topographic highs appear to be strongly attenuated relative to those over topographic lows. See section 3.2.4

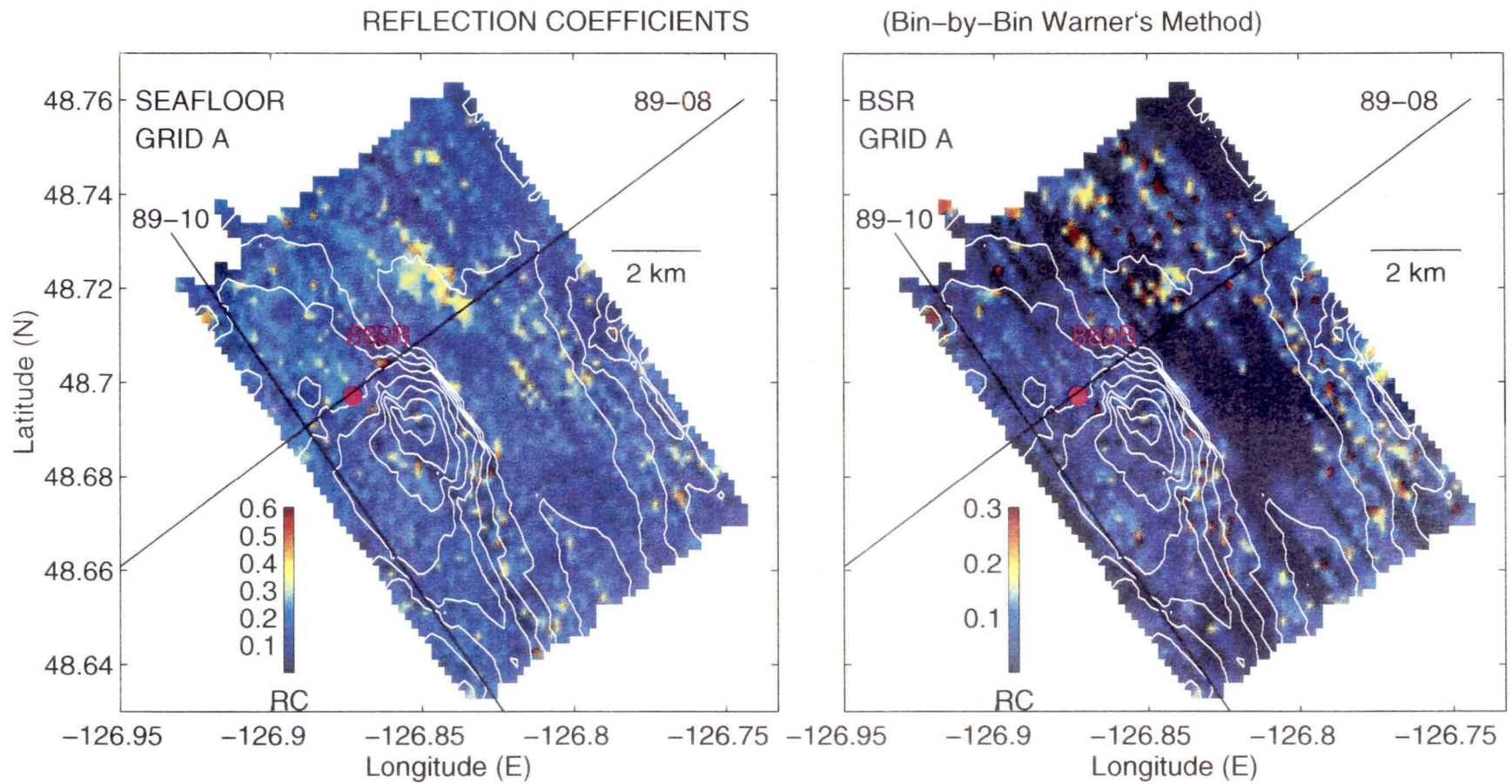


Figure 3.7
 Reflection coefficients for the seafloor (right) and BSR (left) over GRID A generated using a bin-by-bin application of Warner's method. For both the seafloor and the BSR, the regional variation in amplitude appears to have been lost in the conversion to RC by this method. A discussion of why this application may be giving erroneous results is given in Section 3.2.4

RC, it was determined that this application of Warner's method was yielding inaccurate results. In the next section we consider the validity of calculating conversion coefficients locally (i.e., bin-by-bin).

3.2.4 Validity of a Local Application of Warner's Method

Regional variation observed in the seafloor WBM amplitudes (Figure 3.6) follows the same general pattern that is exhibited for the seafloor (Figure 3.1), in that regions of high WBM amplitude correspond to regions of high seafloor amplitude and vice versa, save for the localized region of high WBM amplitude NE of the drillhole, 889B. Although the trends appear reasonably consistent, the relative magnitudes do not. We observe that the ratio of maximum to minimum WBM magnitude is approximately 4:1, nearly identical to the seafloor amplitude max./min. ratio, and contradictory to the results predicted by geometric ray theory (see Figure 3.4 and discussion section 3.2.1).

In regions where the seafloor amplitudes are large the WBM appears to have been attenuated strongly, potentially by a factor of 4. Generally these local highs correlate to regions of increased topographic relief, and the problem may be a result of energy defocusing from the more steeply dipping seafloor in these areas, since the WBM reflects twice from this surface.

Another possibility for low WBM amplitudes is energy scattering from small-scale roughness at the seafloor. On single-channel seismic lines over topographic lows, where seafloor amplitude is relatively low, thin layers of recent slope sediments are interpreted at the seafloor. These sediments drape onto the flanks of local highs in seafloor topography as seen along a section of line SCS-19 (Figure 3.5; 4 - 7.8 km SE of 89-08). The surfaces where these sediments were laid down are expected to be smoother relative to regions where no recent sediments are observed (i.e., topographic highs), and thus, scattering may be accentuated over the topographic highs..

The use of Warner's method to calculate accurate RCs is well documented in the literature. However, the systematic bin-by-bin application of this method shows that great caution must be exercised in choosing the region where the conversion coefficient is calculated. In particular the amplitude of the water bottom multiple has great variability that is difficult to understand and thus difficult to predict. Hence Warner's method reflection coefficient values calculated using only localized data are subject to a potentially significant amount of error that can not be easily quantified.

3.2.5 Single Value Warner's Method Application

Warner comments that the largest source of error for this type of RC calculation is in the calibration of the acquisition system. He outlines three conditions that have been shown to improve the accuracy of the calibration:

- (1) The water depth is large relative to the source-receiver offset.
- (2) The sea bottom is effectively a simple reflector between two half spaces.
- (3) The sea bottom is horizontal and smooth.

The first condition is easily satisfied for our data set considering a receiver offset of only 30 m compared to a water depth of over 1200 m. The second condition is also reasonably satisfied since the impedance contrast at the seafloor is derived primarily from a change in density, and densities within each halfspace are relatively uniform for at least a full wavelength (≈ 20 m for 120 in³ airgun). However, the third condition is rather poorly satisfied in that there is a considerable amount of topographic relief over some regions of the survey. Vertical to horizontal topography ratios of nearly 1:3 (or dips of 18°-20°) are observed in the region of maximum relief (i.e., -126.825°, 48.69° on Figure 2.13).

To satisfy the last condition, a single conversion coefficient for the entire grid was established using data from the flattest portion of seafloor in the survey area. This "flat" region corresponds approximately to the area covered by single-channel lines SCS-26

through SCS-36 and between latitudes 48.67° and 48.71° (see Figures 2.2 and 2.13). WBM and primary amplitudes for the seafloor were used to calculate a conversion coefficient for each trace over this section of the survey (see equation 3.5). A single conversion coefficient of 0.0013 (± 0.0002) was obtained from the median value of these. RCs generated with this conversion coefficient are denoted as "Flat" RCs. Using the conversion coefficient from this method assumes that the acquisition system remained relatively stable over the survey.

3.2.6 Tying the Seismic Data to the Drillhole

A means of obtaining reflection coefficients without the use of multiple to primary ratios is achieved by tying the BSR amplitudes in the immediate vicinity of drillhole 889B to a BSR RC value calculated from downhole density and acoustic velocity data.

The velocity and density estimates above and below the BSR can be inserted into equations 3.2 and 3.1 to yield an expected RC at the drillhole. Density across the BSR appears unchanged from both the corrected density log and core density measurements (Figure 2.10 right) over the depth interval of interest (200 mbsf - 240 mbsf). Assuming a constant density across the interface, equation 3.1 becomes a function of velocity only,

$$RC = \frac{(v_2 - v_1)}{(v_2 + v_1)}. \quad (3.6)$$

The VSP data (Figure 2.10 left), as discussed in Section 2.4.3, are assumed to be the most accurate representation of acoustic velocity, and indicate an average velocity above the BSR of 1830 m/s. This value was obtained from the five VSP data points above the BSR and corresponds to approximately 25 m of sediment. An average velocity of 1515 m/s was obtained from the three available VSP data points below the BSR, corresponding to approximately 15 meters of sediment. Using these velocity estimates, equation 3.6 returns a drillhole RC of 0.0944, indicating that approximately 10% of the incident acoustic wave energy will be reflected from the BSR interface at this location.

A conversion coefficient was derived from the drillhole RC and the regional BSR amplitude for this area,

$$Conv\ Coef = \frac{RC_{Drillhole}}{Amp_{Drillhole}}. \quad (3.7)$$

BSR amplitudes in the immediate vicinity of the drillhole from lines SCS-12 and SCS-13 were averaged to acquire the regional drillhole amplitude ($Amp_{Drillhole}$). Equation 3.7 returned a conversion coefficient of 0.00105.

As was done for Warner's "Flat" method, this conversion coefficient was applied to the BSR and seafloor amplitudes across the survey to obtain the appropriate RC values for these reflectors. The seafloor amplitudes are *reduced* in this case by approximately 15% to compensate for geometrical spreading. RCs generated in this way are denoted as "Drillhole" RCs.

3.3 REFLECTION COEFFICIENT RESULTS

We have determined that the most accurate RC values are those generated by Warner's "Flat" method and by the "Drillhole" method. These RCs are assumed to be accurate within the magnitude of random errors related to acquisition and thus representative of true reflectance at the seafloor and BSR. The results from both methods differ by less than 20%.

RCs generated by these two methods are displayed on the same figure since they are simply a direct scaling of amplitude strength. For ease of discussion the "Drillhole" RCs will be referenced and the corresponding "Flat" RCs will be given in square brackets.

3.3.1 Seafloor Reflector

Figure 3.8 shows the "best estimates" for GRID A seafloor reflection coefficients obtained using the Flat and Drillhole amplitude conversion methods. Maximum RCs of 0.40 to 0.45 [0.50-0.57] are observed in a primarily north-south striking feature that extends north of the drillhole. Similar magnitude RCs can be seen as a linear section along the western edge

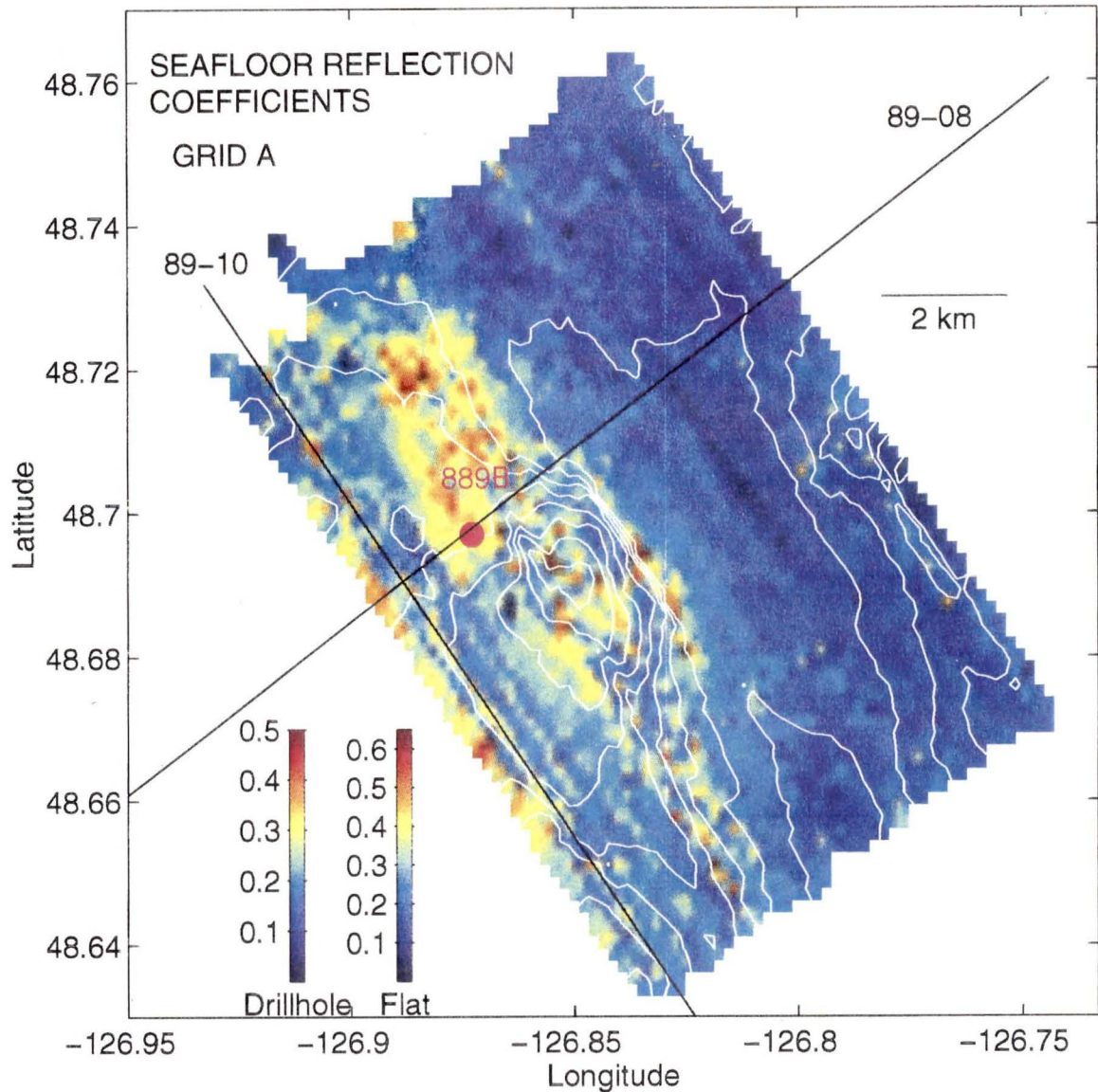


Figure 3.8

Best estimates for the seafloor reflection coefficients over GRID A. These estimates are obtained by scaling the raw amplitudes and therefore the regional amplitude variation is preserved. The legends (bottom left) are labeled according to where in the survey Amplitude-to-RC conversion coefficients were calculated (see sections 3.2.5 and 3.2.6). Maximum "Drillhole" RCs are between 0.35 and 0.45 [0.45-0.60 "Flat"], and grade smoothly to a minimum of approximately 0.15 [0.20] where recent slope sediments are interpreted. RCs of between 0.15 and 0.20 are consistent with the literature for distal turbidites.

of the survey ($-126.86^\circ, 48.65^\circ$ to $-126.90^\circ, 48.70^\circ$) but are separated by a trough of low RC ranging between 0.18 and 0.25 [0.23 - 0.31] which runs the length of the survey.

An elongated oval region SSE of the drillhole exhibits slightly lower RCs between 0.25 and 0.35 [0.31 - 0.45]. These are correlatable to the highest topography in the survey. Moving south from the topographic peak, this feature narrows and RCs decrease in magnitude to between 0.25 and 0.3 [0.31 - 0.37].

East of the ridge RCs grade smoothly to an average of 0.15 [0.19], with a minimum of approximately 0.1 [0.125], along a linear belt paralleling the margin and approximately following the outline of adjacent topographic contours. Further east a subtle increase, to just over 0.25 [0.31], can be observed over the local maxima in topography centered at $-126.79^\circ, 48.71^\circ$.

3.3.2 Bottom Simulating Reflector

For many marine seismic surveys transmission losses at the seafloor are not generally a problem since the seafloor is often very homogeneous in terms of its lithology. However, in this survey area we see that there exists large variability in the seafloor reflectance, and the relative strength of the BSR may have been affected by such changes in reflectivity at the seafloor. We see from figure 3.8 that seafloor RCs for the low-lying section of GRID A are approximately 0.2, suggesting that 20% of the wave amplitude is reflected and 80% is transmitted (neglecting scattering and defocusing effects). For regions of considerably higher seafloor RC, 0.4 for example, only 60% of the wave amplitude is transmitted. We thus expect that the BSR amplitudes recorded beneath regions of high seafloor amplitude are attenuated, relative to amplitudes below regions of moderate to low seafloor RC, by a factor proportional to the difference in the overlying seafloor transmission coefficients. We have corrected the BSR amplitude data for these transmission losses, increasing the BSR amplitude by less than 5% over regions where the seafloor RCs are small, but by up to 25% over the regions where seafloor RCs exhibited local maxima.

Figure 3.9 shows the "best estimates" for the BSR reflection coefficients across GRID A using the conversion coefficients generated from the drillhole-tie and by Warner's method over the flattest seafloor regions. As was noted in section 3.1.2, regions described by reds are considered spurious, and the darkest blue color corresponds to where no BSR was interpreted.

Maximum RCs of 0.15 to 0.18 [0.2-0.23] are observed over the topographic high centered at -126.85° , 48.68° and also within an elongated NNW-SSE striking region north and east of the drillhole. Reflection strength decreases in a relatively smooth fashion away from these local maximums and appears to vary proportional to changes in the topography. Four spatially smaller maximums in RC magnitude are observed at: -126.925° , 48.71° ; -126.91° , 48.7° ; -126.86° , 48.67° ; and -126.77° , 48.67° . The validity of the first two might be questioned owing to their very small size and the lack of smooth gradation radially.

Minimum RCs observed (where the BSR is interpreted) range between 0.05 and 0.07 [0.062-0.087]. The median average RC value for the entire survey is estimated at between 0.09 and 0.11 [0.12-0.15].

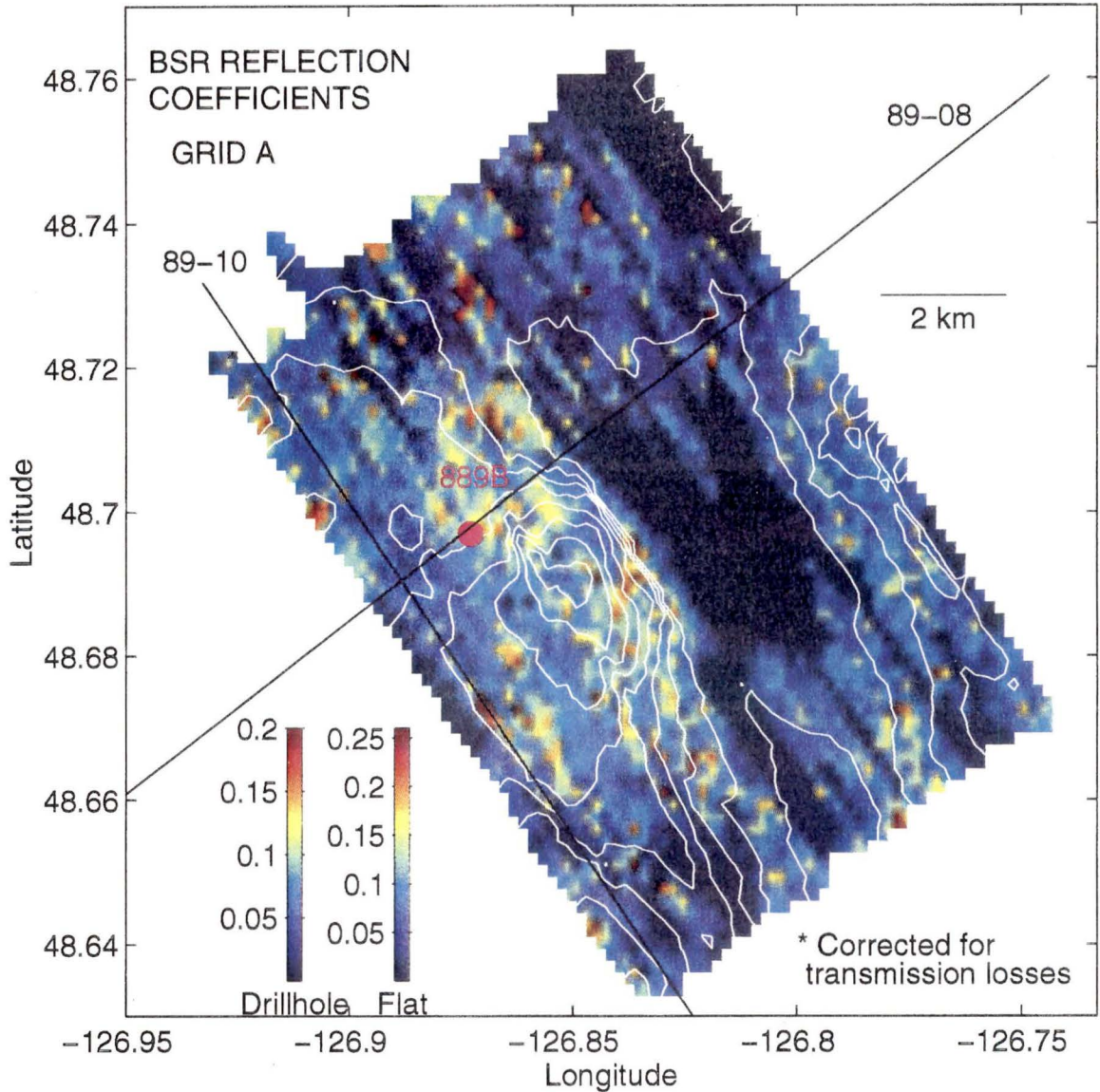


Figure 3.9

Best estimates for the BSR reflection coefficients over GRID A. These estimates are also obtained by scaling the raw amplitudes and, again, legends are labeled "Drillhole" and "Flat" according to where conversion coefficients were calculated. Maximum "Drillhole" RCs are between 0.13 and 0.16 [0.17-0.22 "Flat"]. Background RC magnitudes range between 0.05 and 0.07 [0.062-0.087], and the median average over the entire survey is estimated at between 0.08 and 0.1 [0.1-0.125]. Spatial variability is strongly constrained by local topography, and suggests that it may be influencing hydrate concentration, assuming this is the primary control for RCs at the BSR.

CHAPTER FOUR FREQUENCY ANALYSIS

4.1 OBJECTIVES OF FREQUENCY ANALYSIS

The data set used for this thesis is unique, compared to typical marine surveys which image the BSR, in that we are able to evaluate the BSR's response to seismic data of three independent dominant source frequencies. As discussed in chapter 2, these are; 30 Hz, 75 Hz, and 150 Hz (primary frequencies). Velocity and density data from ODP site 889 have been used to develop realistic synthetic seismogram models as a "tie" for the seismic data, and to model tuning effects at the BSR and at the seafloor. All seismic models were developed using the PC based Outrider™ software.

The specific objectives of the frequency analyses were: (1) to test the correspondence between the seismic data and synthetic seismograms generated from the VSP and density log data, for each of the primary frequencies; (2) to establish minimum thicknesses for discrete layers above and below the BSR by accurately determining the tuning widths of each of the primary frequencies, and (3) to develop practical geologic models that describe the observed reflectivity at the BSR and at the seafloor.

4.2 WAVELET EXTRACTION

Before any synthetic seismograms were created, waveforms for the primary frequencies were established. Source wavelets were extracted from the data by averaging the seafloor reflection waveforms over the survey area. The seafloor was chosen because it is generally considered to represent a simple reflector, free from such effects as attenuation, interbed multiples and strong velocity gradients which can distort the source waveform. For the 30 Hz data, 50 seafloor reflection waveforms from 89-08 and 89-10 were averaged. For the 150 Hz SCS data set, 100 seafloor reflections from GRID B were averaged, and from the larger 75 Hz SCS data set, approximately 200 seafloor reflection

waveforms, sampled regularly from across GRID A, were averaged to extract the dominant waveforms.

Figure 4.1 shows the results of this technique. All three source wavelets are approximately zero phase and can be described as a single peak framed by two equally spaced troughs. Simple trough to trough measurement returned frequencies for these waveforms within 5% of the dominant frequency determined from their amplitude spectra (Figure 2.11). Wavelengths at the BSR were calculated using the equation,

$$\lambda = v / f, \quad (4.1)$$

where v is 1830 m/s, corresponding to the velocity above the BSR derived from the VSP measurements. At the seafloor, wavelengths are approximately 20% shorter corresponding to the difference between velocity above the BSR and seawater velocity (~1460 m/s).

A zero phase Ricker wavelet of the appropriate frequency very closely approximates the observed waveforms for each of the primary frequencies. Thus, in the synthetic seismogram comparisons below, a Ricker wavelet was used so that results could be attributed solely to differences in dominant frequency, and not to minor differences in wavelet shape.

4.3 SYNTHETICS SEISMOGRAMS FROM VSP DATA

Figure 4.2 shows the synthetic seismograms for each of the primary frequencies, generated from the velocity contrasts established by the VSP at 889B (Figure 2.10). Layer densities have been approximated from the compressional wave velocities using the following relation;

$$\rho = 1.135V_p - 0.190, \quad (4.2)$$

where ρ is g/cm^3 and V_p is in km/s. This relationship was established by Hamilton (1978) for shallow marine sediments (silts, clays, and turbidites), and is in good agreement ($\pm 5\%$) with the velocity and density data recorded at site 889.

PRIMARY FREQUENCY WAVELETS

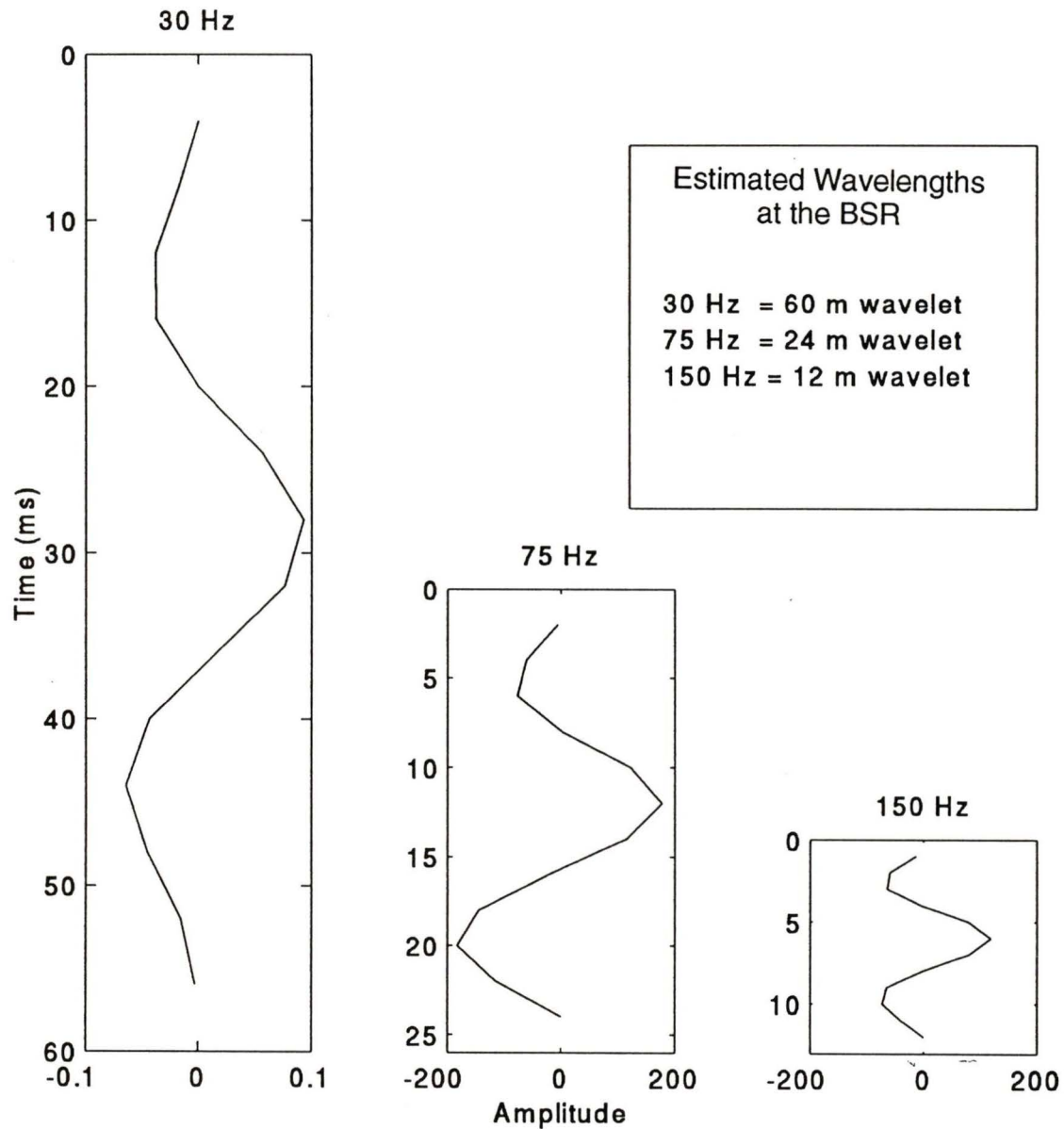


Figure 4.1

Source wavelets for the primary frequencies. Source wavelets were approximated by extracting seafloor reflection waveforms from the seismic data. Each wavelet is shown in proportional size. Sampling rates are 4 ms, 2 ms and 1 ms for the 30 Hz, 75 Hz, and 150 Hz data, respectively. Wavelengths at the BSR are estimated using equation 4.1.

The impedance contrast at the seafloor is generally considered the result of an increase in density there. Since neither seafloor velocity nor density data were available from the drilling sites, we assume the seafloor is typical Cascadia margin sediment, with a velocity of 1460 m/s and a density of 1.60 g/cm³ (Hannay and Chapman, 1995). VSP velocities were only established for the region 125-243 mbsf (see Figure 2.9). To model the section from seafloor to 125 mbsf, a monotonically increasing velocity function was used from the seafloor velocity to the first VSP velocity estimate (1756 m/s), and therefore no reflections were generated in the synthetics for this zone. Each seismic section displayed in Figure 4.2 shows 11 traces, with the center trace corresponding to that which is nearest to the drillhole.

The difference in reflector arrival times observed between each frequency is a result of differences in recording time lag during acquisition. Note that the interval time for the seafloor to BSR reflections is the same for all three frequencies. The two-way travel times identified by the 30 Hz data are assumed to be correct. Minor differences in traveltimes intervals for the seafloor to first reflector on the synthetic seismograms can be attributed to inaccuracies in the linear velocity function used for this section.

A reflection of particular interest in the synthetics is the small amplitude event just above the BSR, seen most clearly on the 75 Hz (at 2.05 s) and 150 Hz (at 2.02 s) sections. This event correlates temporally to the moderately large decrease in velocity shown on the VSP 10 m above the BSR. Like the BSR, this reflection has negative polarity, and as such can not be modeled as the top of a thin hydrate zone, since an increase in velocity due to a concentration of hydrate in the porespace would result in a positive impedance contrast. We suggest that this moderate decrease in velocity above the BSR may represent either (1) a lithologic boundary within the overlying sediments, (2) a zone of sediments with very small concentrations of free gas (<<1%), or (3) a zone of reduced concentration of hydrate relative to the zone above.

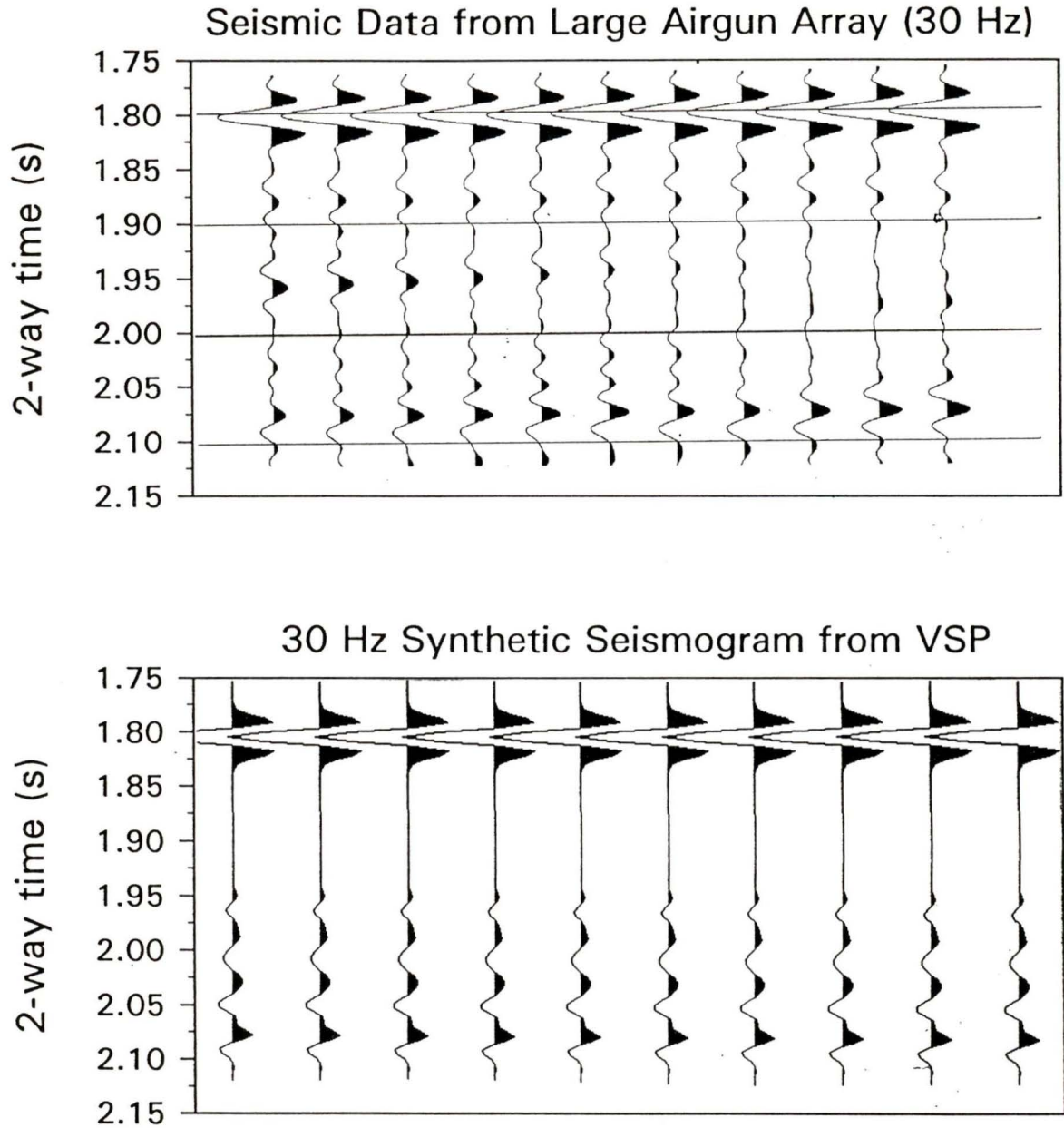


Figure 4.2

Comparison of seismic data and synthetic seismograms generated from VSP data at 889B for each of the primary frequencies. Each seismic section displayed shows 11 traces, with the center trace corresponding to that which is nearest to the drillhole. The seismic section above is from 100% coverage line MCS 89-08.

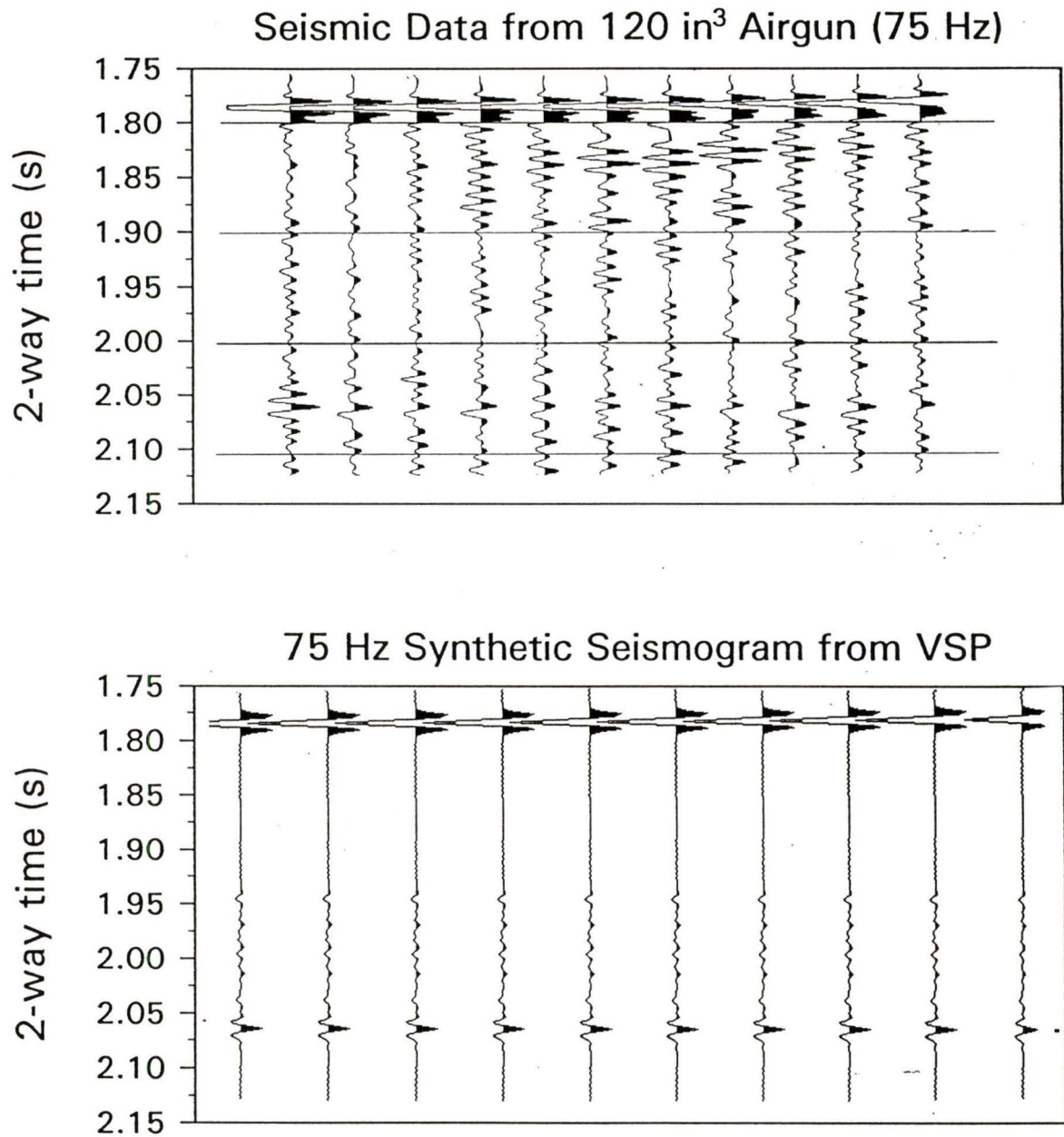


Figure 4.2 continued

75 Hz seismic data from line OBS-2A and corresponding synthetic seismogram from VSP data.

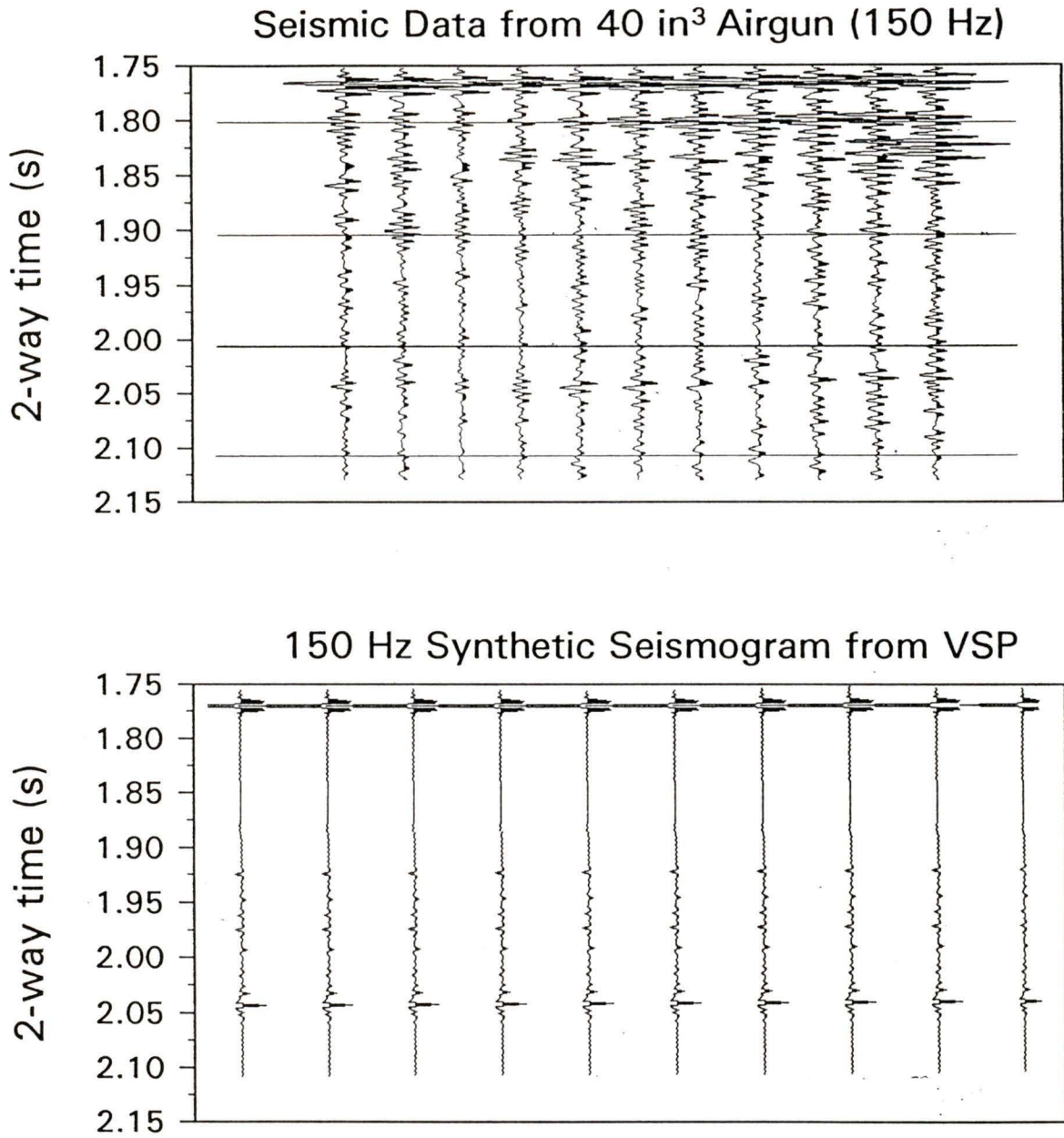


Figure 4.2 continued
150 Hz seismic data from line SCS-72 and corresponding synthetic seismogram from VSP data.

Below 1.90 s the synthetic seismograms correlate well with the recorded data. Thus, we have accepted the velocities established by the VSP with a high degree of confidence and have used these estimates in developing realistic velocity models at the BSR. As discussed in section 3.2.6, the velocity for the high-velocity zone above the BSR was taken to be the average of the VSP velocities for 25 m above the BSR (1830 m/s). We have also assumed that the velocity for the low-velocity zone can be approximated by the average of the three existing VSP measurements below the BSR (1515 m/s).

4.4 SYNTHETIC SEISMOGRAM MODELING

4.4.1 Tuning Width Analysis

The VSP data provide solid evidence for the existence of both a zone of high-velocity (HVZ) above the BSR, possibly due to hydrated sediments, and a zone of low-velocity (LVZ) below the BSR, potentially the result of a small concentration of free gas (1-5%) in the porespace. However, the thickness of these zones is undetermined. The uncertainty arises because there is no seismically detectable top to the HVZ, or bottom to the LVZ.

It is generally agreed that the velocity of a zone of hydrated sediments decreases gradationally upward from the BSR in response to a decrease in hydrate concentration (Katzman et al., 1994; Minshull et al., 1994; Singh et al., 1993; Hyndman and Spence, 1992; Collins and Watkins, 1985; and others), and this seems to fit the sonic log and VSP data from site 889. However, one might expect that a free gas zone would have a sharp bottom, particularly if this zone is the result of hydrate dissociation in response to the upward migration of the base of the methane hydrate stability field (Whiticar, 1995 [personal communication]). Unfortunately the VSP data did not sample sediment velocities at depths greater than 15 m below the BSR, and therefore the possibility that a sharp base to the presumed free gas zone exists is neither established nor dismissed.

From seismic data, the base of a free gas zone can be identified by a strong reflection or "flat spot" (White, 1979). Figure 4.3 shows coincident seismic lines MCS

seen, and in particular no flat spot can be identified. When only 30 Hz (multichannel) seismic data were available in this area, it was suggested (Hyndman & Spence, 1992; Singh and Minshull, 1993; and others) that the absence of such a base to the free gas zone might be the result of tuning effects between the negative polarity event at the BSR and the positive event at the base of a thin free gas zone, such that only a single reflection was observed. Simplified tuning width estimates suggested that the gas zone must be consistently less than about 15 m thick ($1/4 \lambda$), but still no less than approximately 7 m thick to account for the strong amplitudes recorded. The acquisition and analysis of higher frequency data has enabled us to evaluate the precise tuning widths for waveforms of variable length. With this type of analysis we are able to confidently eliminate the possibility of a sharp base for a low velocity zone (LVZ) of any thickness that could result in amplitudes as high as those obtained along MCS lines 89-08 and 89-10. In the interest of completeness we have determined a similar result ruling out the possibility of a thin layer of high velocity hydrated sediments above the BSR.

To quantitatively determine the "tuning width" of each source frequency, synthetic seismogram modeling was performed for two 3-layer velocity models. Each model was developed with a wedge of either hydrated or free gas bearing sediments between two half spaces of appropriately different sediments. Wedge thicknesses ranged from 1 m to approximately 50% of the dominant wavelength being modeled so that the interference effects of the waveforms could be determined as a function of layer thickness. The 1 m lower limit is the minimum thickness allowed by the modeling software.

The velocity and density values used for each wedge layer correspond to the velocity (VSP only) and density data from ODP site 889 (see Figure 2.10). Above and below the wedge layer in each model, realistic velocity-depth functions were used to identify impedance parameters for these layers. The velocity-depth function for typical

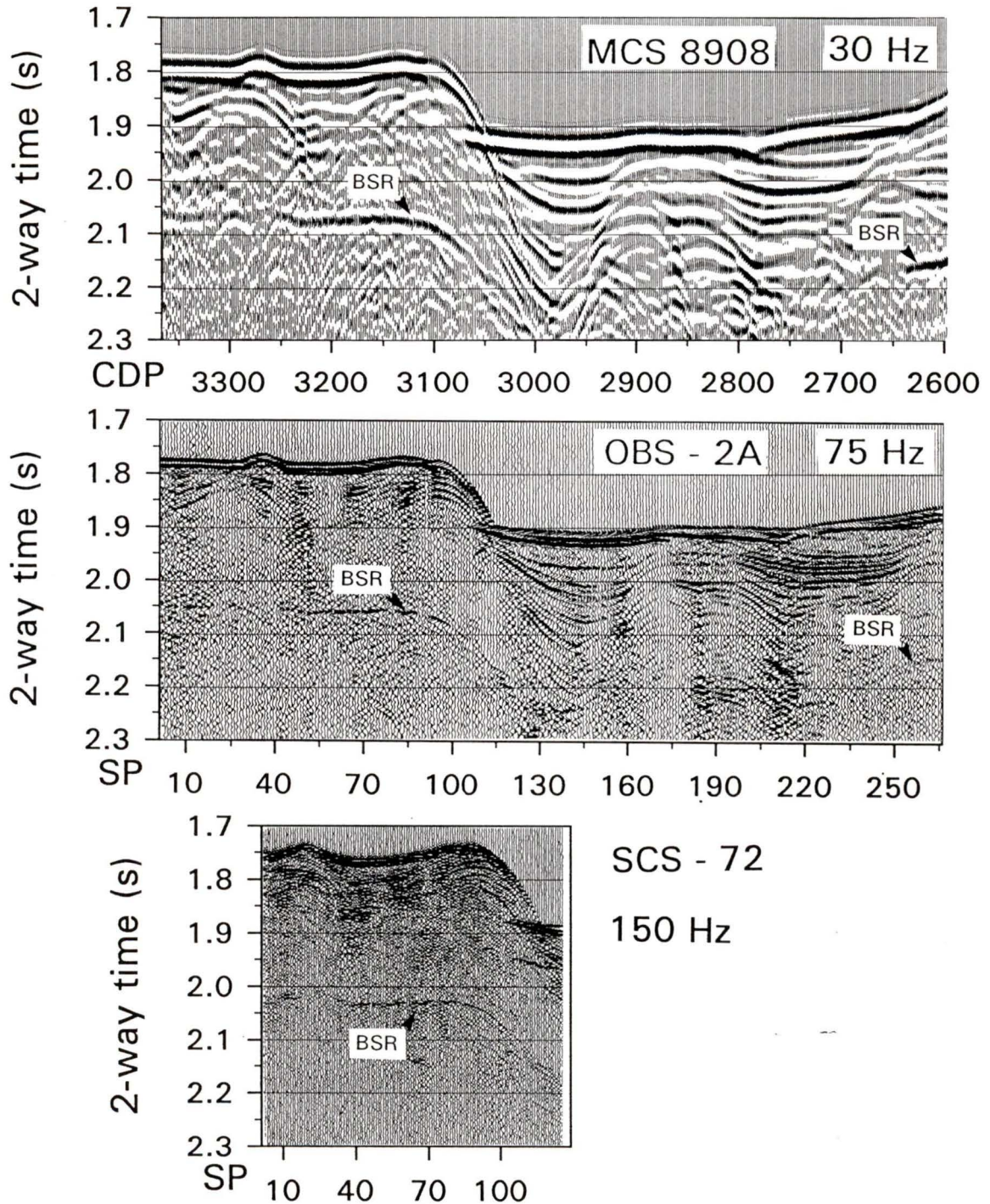


Figure 4.3

Observation of only a single BSR reflection for seismic lines of the three primary frequencies (1). Lines shown are MCS 89-08, OBS-2A, and SCS-72. Low frequency line is plotted as variable area due to high density of trace coverage. No BSR is identified under lowest seafloor topography (see discussion in section 3.1.2).

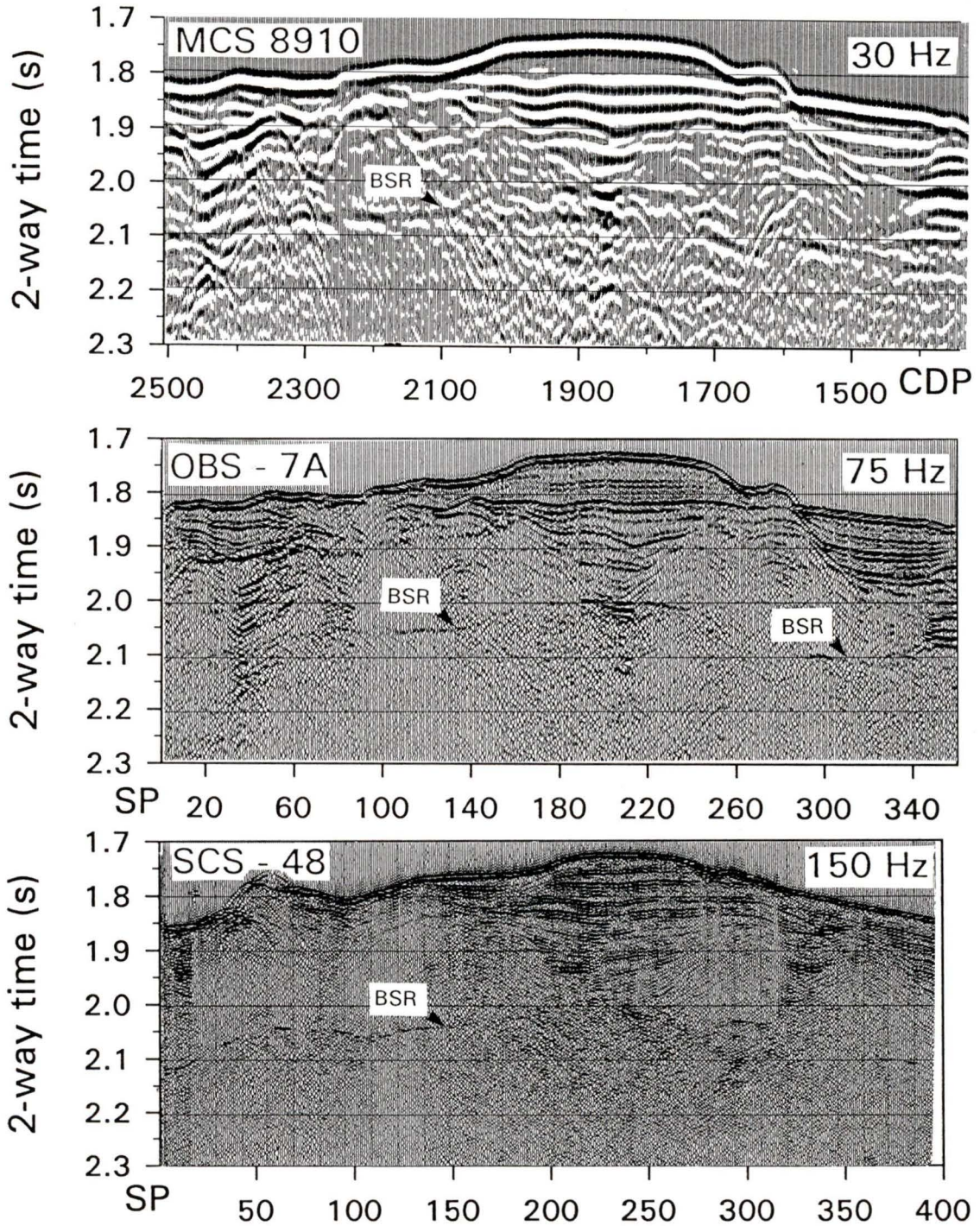


Figure 4.4

Observation of only a single BSR reflection for seismic lines of the three primary frequencies (2). Lines shown are MCS 89-10, OBS-7A, and SCS-48. See Figure 2.2 for location within survey. Low frequency line is plotted as variable area due to high density of trace coverage. Higher density of SCS-48 is due to reduced shot spacing for high frequency lines.

margin sediments with no concentrations of free gas or methane hydrate (Figure 4.5) was derived from a third order regression fit to detailed RMS interval velocity analyses on the multichannel data within the survey area (Yuan et al., 1994). This "background" velocity function is approximately linear, and at BSR depths yields a velocity of 1625 m/s (± 25 m/s).

Velocity Models

Model 1 (Figure 4.6 top) includes a constant velocity wedge of free gas bearing sediments below a half space of hydrated sediments with velocity 1830 m/s. The velocity in the wedge is held constant at 1515 m/s, which is consistent with a gas-brine mixture in the sediment pore space (Domenico, 1976). Although gas concentrations above 1% generally result in lower sediment velocities, MacKay et al. (1993) comment that the high pressures due to water depths greater than 1300 m (~13 MPa) can act to diminish the velocity reduction effect. Below the gas layer, the velocities are assigned to values from the background velocity-depth function.

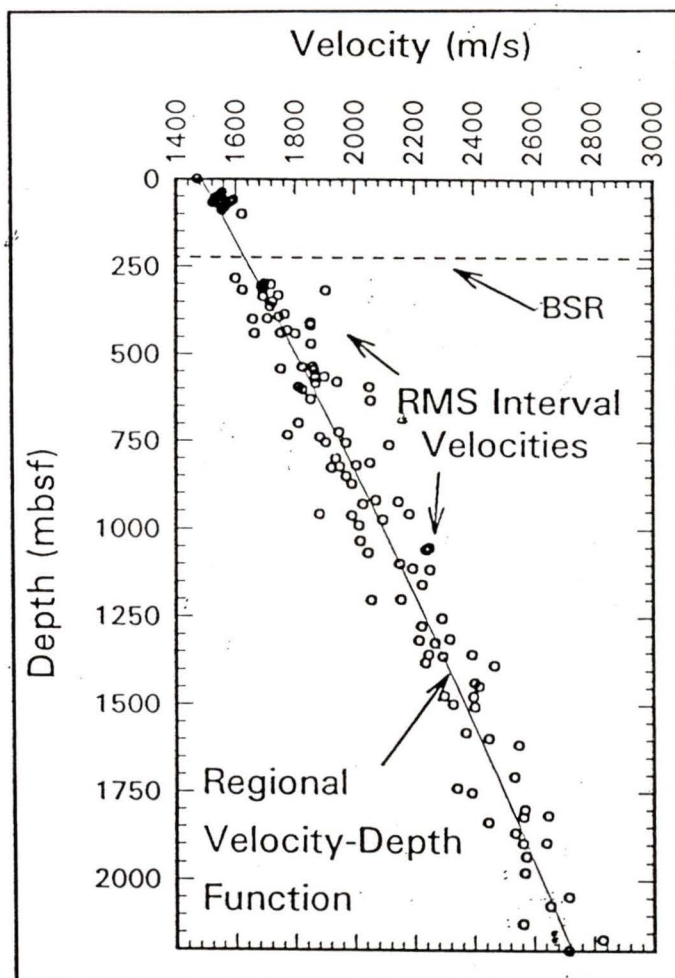


Figure 4.5

Regional velocity depth function for typical margin sediments in survey area. RMS interval velocities were calculated from stacking velocities interpreted from multichannel seismic data within the survey area. A third order regression fit to the data describes the regional velocity-depth function for this area. A small section above and below the BSR has been excluded so that the function is not influenced by the presence of hydrate or free gas. This function yields a "normal" sediment velocity at BSR depths of 1625 m/s. Modified from Yuan et al., 1994.

Model 2 (Figure 4.6 bottom) includes a wedge layer of relatively high velocity due to hydrated sediments above the BSR. The velocity within the wedge is held constant at 1830 m/s. Above and below the hydrate wedge, the background velocity-depth function is used to establish realistic gradient velocity parameters.

In models 1 and 2 the density for both the hydrate and free gas layers is held constant at 1.85 g/cm^3 consistent with the well site density estimates (Figure 2.10).

Synthetic Seismograms

Amplitude strength

for the synthetic seismograms was calibrated by calculating the theoretical BSR to

seafloor amplitude ratio which is a quantity that can be directly compared to what is observed on the seismic data. This was achieved by first calculating the reflection coefficient at the seafloor and at the top interface of the wedge, from their modeled acoustic impedances using equations 3.1 and 3.2. The seafloor amplitude, A_{SF} , could then

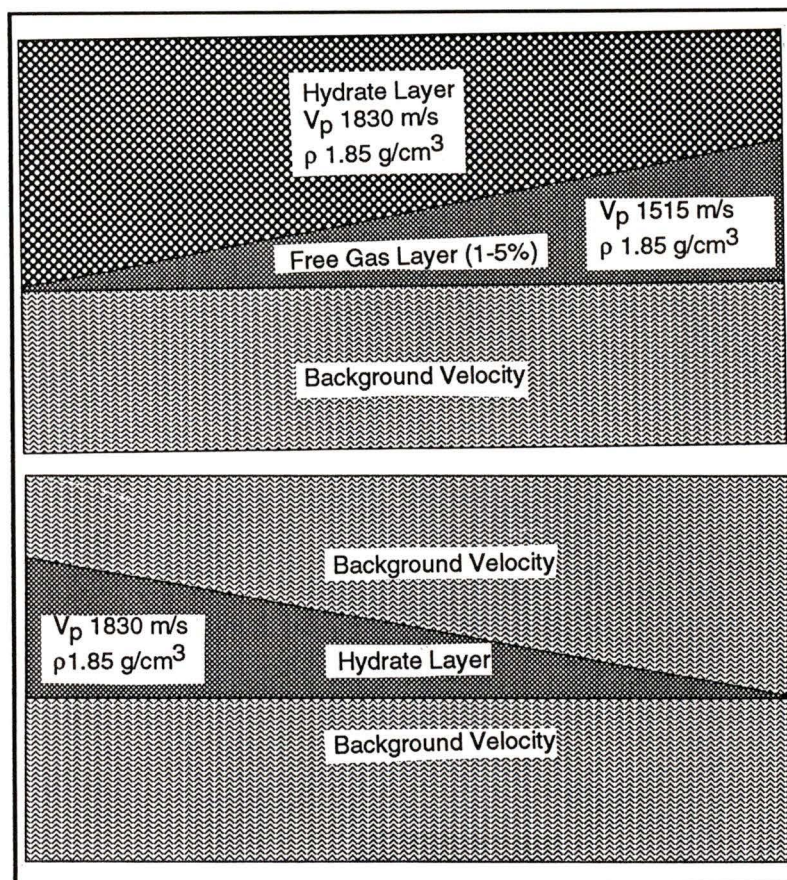


Figure 4.6

Tuning width velocity models. Model 1 (top) describes a wedge of gas bearing sediments overlain with a gradational half space of hydrated sediments. Below the gas layer, normal margin sediments are modeled. Model 2 is a wedge of hydrated sediments between two half spaces of typical margin sediment. The "normal" margin sediment velocities were calculated from a regional velocity-depth function (see Figure 4.5).

be expressed in terms of the amplitude where no interference (tuning) effects were observed, $A_{no\ tune}$:

$$A_{SF} = A_{no\ tune} \left(\frac{RC_{SF}}{RC_{no\ tune}} \right). \quad (4.3)$$

The resultant BSR to seafloor amplitude ratio was determined from the ratio of tuned reflection amplitudes to untuned reflection amplitudes observed on the synthetics;

$$\frac{A_{tuned}}{A_{SF}} = \frac{A_{tuned}}{A_{no\ tune} \left(\frac{RC_{SF}}{RC_{no\ tune}} \right)} \quad (4.4)$$

Synthetic seismograms generated from models 1 and 2 are shown in Figures 4.7 and 4.8, respectively. The results for both models are very similar, and since the main question of tuning effects concerns the possibility of a thin layer of gas-bearing sediments below the BSR, we limit our discussion to the results of model 1. The theoretical reflection coefficient for the seafloor is 0.19, assuming that only densities change across the interface (i.e., 1.05 to 1.60 g/cm³). However, the reflection coefficient analyses in Chapter 3 indicated much larger RC values, as high as 0.45 in some areas. For the model we selected a value of 0.23 since this value is consistent with the literature for distal margin sediments (Rohr et al., 1993; Warner, 1990). The RC determined from equations 3.1 and 3.2 for the top interface in model 1 (hydrate over free gas) is 0.09417.

It can be seen from the top diagram in Figure 4.7 that the 30 Hz data are able to resolve a top and bottom to the gas layer for thicknesses greater than about 20-25 m (~40% λ_{30}). Maximum constructive interference occurs between 14 m and 6 m (23%-10% λ_{30}), and below 6 m amplitudes drop off sharply. Amplitudes for thicknesses less than 2-3 m result in very small BSR to seafloor amplitude ratios (< 0.15).

The 75 Hz synthetic seismogram identifies two-layer resolution for any thickness greater than about 8 or 9 m (~40% λ_{75}). Maximum constructive interference is observed from 5.5 m to 3.5 m (23%-15% λ_{75}), after which we begin to see destructive interference effects.

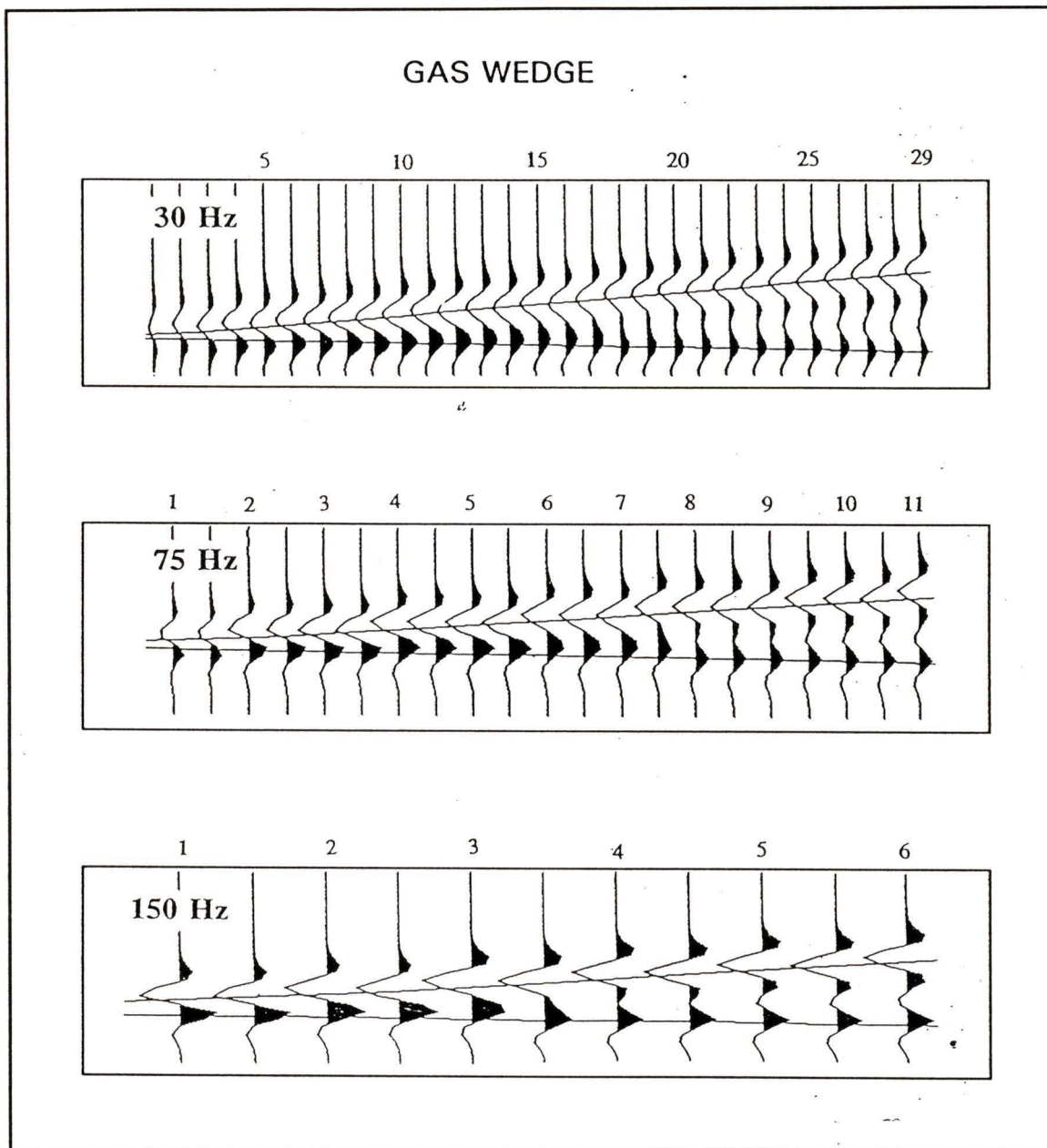


Figure 4.7

Wedge model synthetic seismograms for free gas zone. Tuning widths for a thin layer of low velocity are identified for each of the primary frequencies. Wedge thickness is given in meters across the top of each seismogram. See text for specifics of model layers. Two-layer resolution thickness occurs at 20-25m for 30 Hz data, 8-9 m for 75 Hz and 4-4.5 m for 150 Hz data. Destructive interference effects can be seen for the low frequency data at thickness less than 5-6 m. Results indicate that a thin discrete layer of low velocity below the BSR is unlikely.

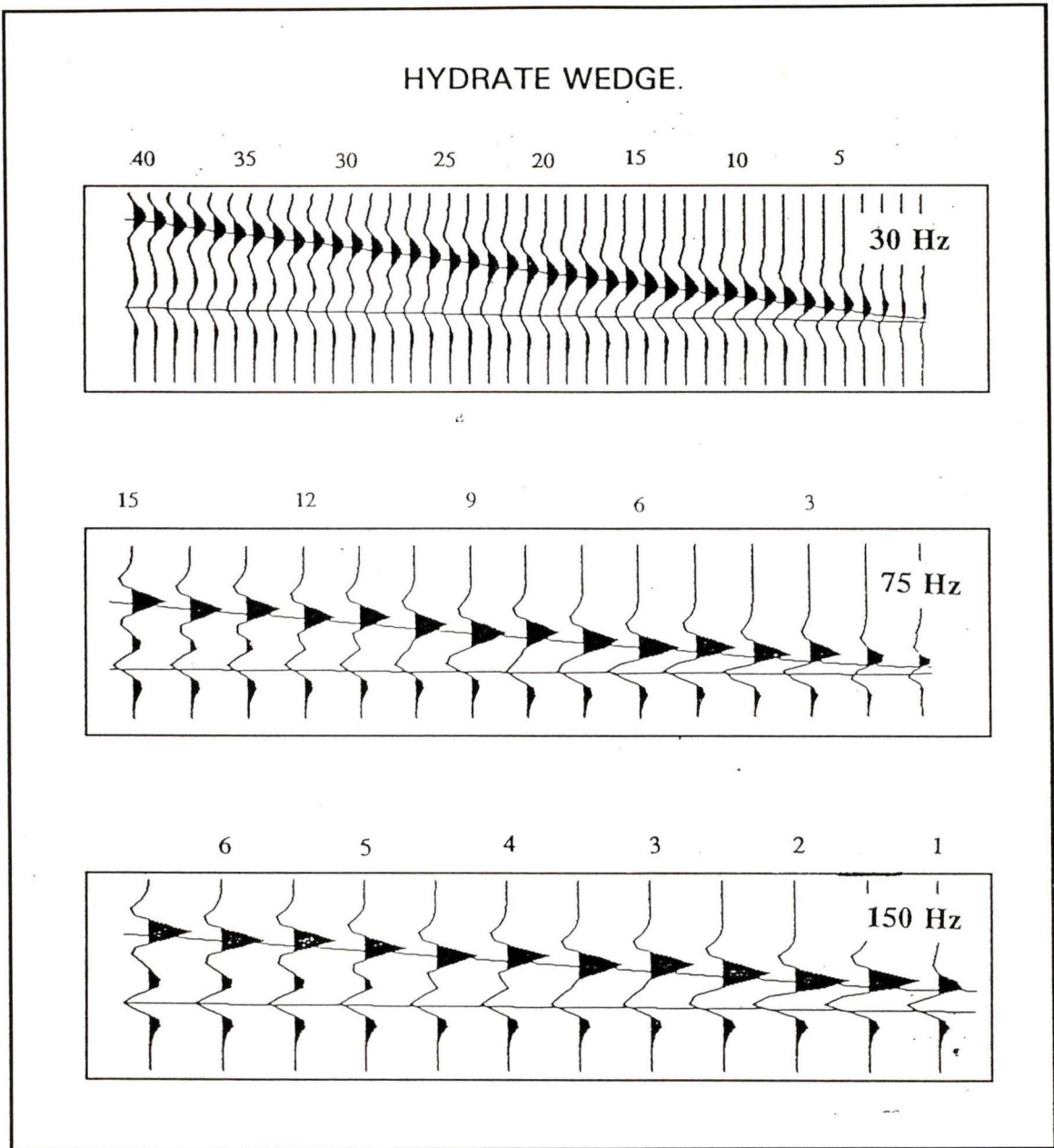


Figure 4.8

Wedge model synthetic seismograms for hydrate zone. Tuning widths for a thin layer of high velocity (HVZ) are identified for each of the primary frequencies. Wedge thickness is given in meters across the top of each seismogram. See text for specifics of model layers. The results for this model are similar to the gas wedge results, but resolution thicknesses are increased for each frequency. 30 Hz data clearly resolves a top and bottom to the HVZ at 28-30 m compared to 20-25 m for the free gas layer. Similar differences are observed for the 75 z and 150 Hz synthetic seismograms. This is likely the result of a less substantial impedance contrast for the hydrate only model.

The bottom seismogram on Figure 4.7 identifies the resolving power of the 150 Hz seismic data. We see that for thicknesses greater than 4-4.5 m ($\sim 40\% \lambda_{150}$), reflections from both the top and bottom of the gas layer can be seen. Below 3 m ($\sim 25\% \lambda_{150}$) this frequency shows consistent waveforms with high relative amplitude corresponding to maximum constructive interference. BSR to seafloor ratios for this thickness are approximately 0.45-0.50.

Requirement of Free Gas Layer

By calculating the theoretical reflection coefficients generated for the hydrate-only model and for the free-gas below hydrate model, it has been determined that a zone of low velocity is necessary to generate BSR-to-seafloor amplitude ratios similar to those observed in the seismic field data. The existence of free gas in small quantities (but greater than 1% by volume) can produce the required LVZ below the BSR (MacKay et al., 1994; Domenico, 1976). Free gas below the BSR is thus implied for this study area.

Ruling Out a Thin Layer

We may now examine the practicality of a thin layer of gas bearing sediment below the BSR. We begin by assuming that the LVZ below the BSR is a thin layer with a sharp top and bottom. The wedge model analysis shows that in order for only one reflector to be observed on the 150 Hz data, this layer must be consistently less than 4 m. For a LVZ thickness of less than 4 m, the BSR to seafloor amplitude ratio would be larger for the 75 Hz and 150 Hz data than for the 30 Hz data. However, the 30 Hz seismic data identifies the highest BSR to seafloor amplitude ratios of the three primary frequencies, up to 0.5 in some areas along MCS line 89-08 (see Chap. 3; also Hyndman and Spence, 1992). This analysis strongly suggests that the single reflection observed at the BSR can not be the result of tuning effects between the top and bottom of a sharply defined low velocity zone. The modeling results also imply that the concentration of free

gas decreases gradationally, and thus increases gradationally with respect to velocity with increasing depth below the BSR.

The results of the tuning effects identified in this section are used in the following section to model the anomalously large reflectivity observed at the seafloor over some regions of the survey.

4.4.2 Carbonate Pavement at the Seafloor

The seafloor reflection coefficients obtained from the 75 Hz amplitude data (Figure 3.8) show localized regions of very high RC. Values as high as 0.44-0.55 (depending on scale method used) were observed in the region of ODP site 889, and in other regions of locally high seafloor topography (see 3-D seafloor topography in Figure 2.14). One explanation for the large RC values is hydrothermally induced cementation of calcium carbonate and silica resulting in a carbonate pavement at the seafloor (Carson et al., 1994; Rohr et al., 1993).

Figure 4.9 is a plot of raw amplitudes for coincident lines OBS-2A (75 Hz) and MCS 89-08 (30 Hz). A sharp drop (break) in amplitude is observed along line 2A at approximately 2 km NE of cross-line MCS 89-10. This break corresponds spatially to a relatively sharp drop in seafloor topography, or increase in water depth from 1325 meters below sealevel (mbsl) to 1440 mbsl over 500-700 m horizontal distance. Southwest of this break, amplitude values are approximately 2.15-2.25 times as large as those NE of the break. However, for line MCS 89-08 (30 Hz), the amplitudes SW of the break are only about 1.21-1.33 times as large as those NE of the reference point.

The tuning width analysis suggested that a thin HVZ could generate the observed difference in the relative amplitudes for two lines of high and low frequency. A thin layer of high velocity carbonate overlying "normal" seafloor sediments was modeled to explain the observed differences. Velocity and density for the carbonate layer were set to 3000 m/s and 2.29 g/cm³, respectively, consistent with the values given by Hamilton (1978).

The thickness was restricted to 2 m corresponding to a thickness where 30 Hz amplitudes are strongly attenuated due to interference effects between the top and bottom of the layer. The topographic relief of the geologic model was designed to represent the structure observed in seismic lines MCS 89-08 and OBS-2A (Figure 4.3). The carbonate layer was confined to the topographically elevated section SW of the break.

The resulting synthetic seismograms are shown in Figure 4.10. For the 75 Hz synthetic seismogram, we observe amplitudes corresponding to where the carbonate was included, that are 2.21 times as large as amplitudes from the region where only normal sediments were modeled. For the 30 Hz synthetic, amplitudes for the elevated regions were only 1.36 times as large as those returned for "normal" seafloor sediments.

The modeling results are in good agreement with the observed 75 Hz and 30 Hz amplitudes as shown in Figure 4.9. Considering the simplicity of the model, we feel this is good evidence to support the existence of a thin layer of high-velocity at the seafloor. Carbonate pavement seems a likely scenario which could produce the required HVZ.

4.5 Frequency Analysis Overview

We conclude that the VSP data can accurately describe the velocity function for the region above the BSR and immediately below it. The data imply that the BSR reflection is due to a HVZ above the BSR and a LVZ below it, each relative to the regional background velocity function which describes unhydrated, gasless sediments at these depths. It has been determined that the single BSR reflection can not be the result of tuning between the top and bottom of either a thin HVZ above or a thin LVZ below the BSR. Both the HVZ and the LVZ must be gradational, away from the BSR interface.

The high seafloor reflectivity observed over some regions of the survey area can be modeled by a thin layer of high velocity at the seafloor. The layer must be thin enough such that destructive interference of 30 Hz data obscures the impedance contrast for those data, but still be thick enough so that 75 Hz waveforms will sample a significant portion

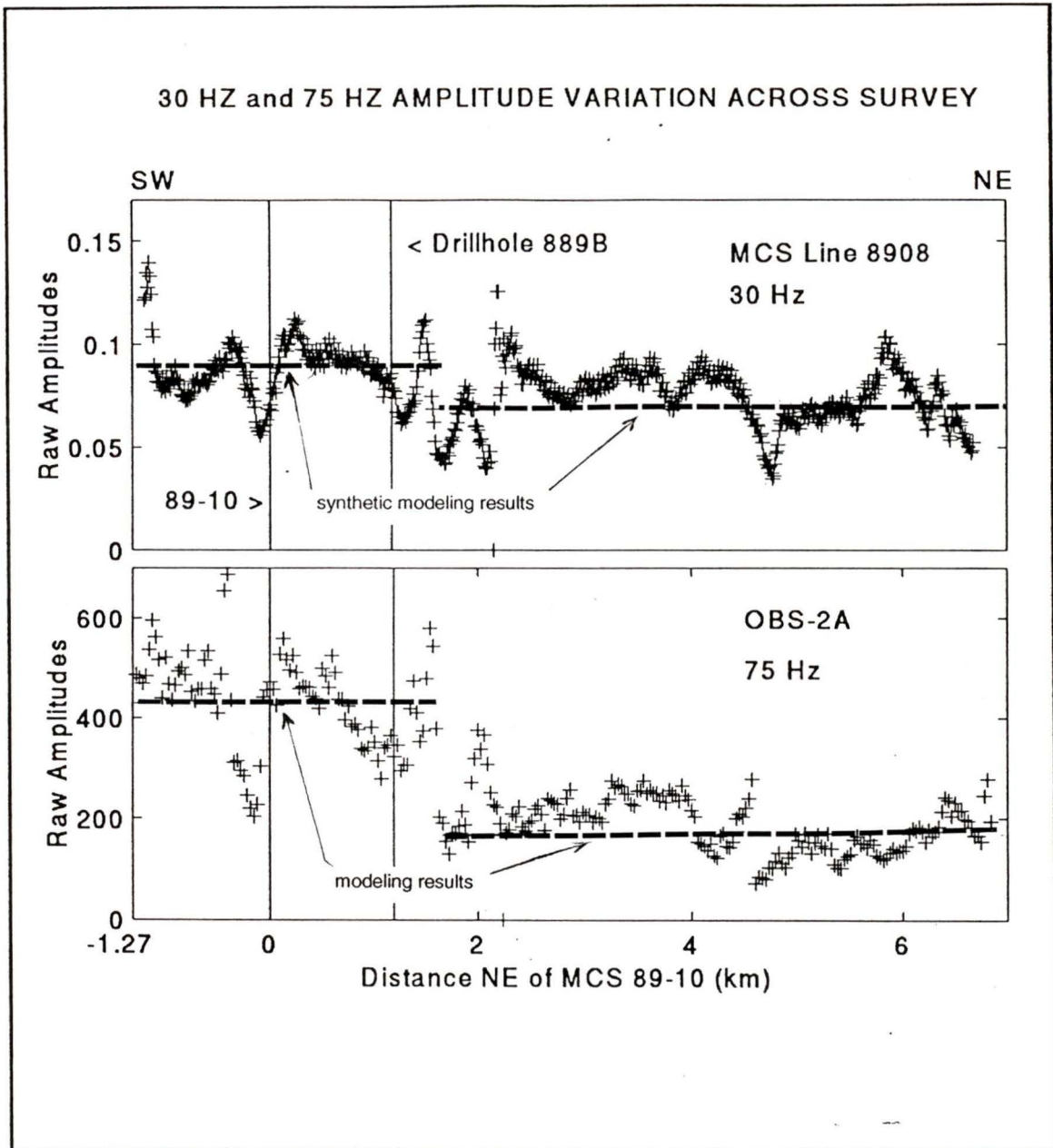


Figure 4.9

Seafloor amplitude variation between 30 Hz and 75 Hz coincident lines. A large decrease in amplitude is observed on line OBS-2A approximately 2 km NE of X-line 89-10 (0 reference). The ratio of high amplitude to low amplitude for the 30 Hz data is 1.21-1.33, but increases to 2.25-2.5 for the 75 Hz data. The results of the thin layer modeling are shown as dashed lines. The lower amplitude line was chosen arbitrarily, as an approximate average to what is observed. The high amplitude section is plotted according to the observed amplitude ratio on the synthetic seismograms of Figure 4.10.

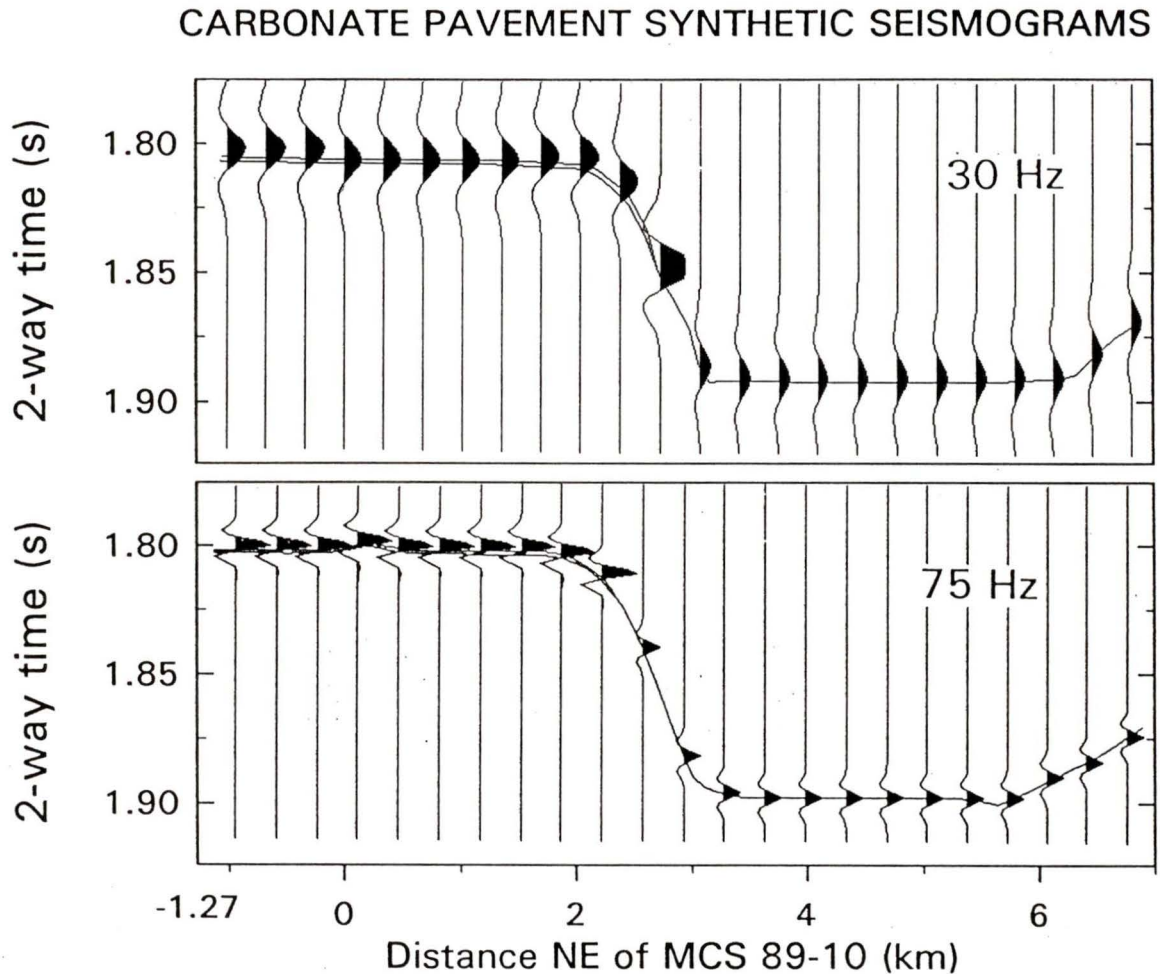


Figure 4.10

Carbonate pavement synthetic seismograms. The observed difference in amplitudes between 30 Hz and 75 Hz seismic data has been modeled to be partially the result of a thin layer of high velocity carbonate at the surface. The model structure was designed to represent the structure observed in lines MCS 89-08 and OBS-2A, with a thin layer of carbonate pavement above only the topographically high region west of the 2 km reference point. The lines shown on the model represent the time horizon of the structure modeled. The carbonate layer in the model is 2 m thick with a velocity of 3000 m/s and a density of 2.29 g/cm³ (Hamilton, 1978). The amplitudes for the 30 Hz synthetic increase by a factor of ~1.36 over the region where the carbonate is modeled but for the 75 Hz data, the increase is by a factor of ~2.21 (see Figure 4.9).

of the HVZ. Because a 225-250% increase in amplitude is observed for the 75 Hz data, it is inferred that velocities of at least 3000 m/s ($\rho \sim 2.3 \text{ g/cm}^3$) are required at the seafloor. The thickness of the carbonate pavement is estimated to be approximately 2 m; thick enough that the 75 Hz data will sample the high velocity material, yet thin enough that destructive interference effects will dominate for the 30 Hz data.

CHAPTER FIVE DISCUSSION OF RESULTS

5.1 FACTORS AFFECTING SEISMIC AMPLITUDES

5.1.1 Focusing and Defocusing

Focusing and defocusing produced by lateral velocity variations or by curvature of a reflector can produce amplitude anomalies in vertically-incident reflection data. It has been shown (Raynaud, 1988) that anomalies due to lateral velocity variations are, in general, much smaller than those predicted by geometrical ray theory since the finite wavelength of the reflected signal acts to smooth lateral variations in amplitude. Focusing due to reflector curvature is an unlikely cause of the high reflection strength observed for the seafloor and the BSR in this survey area, since the highest amplitudes for both reflectors are observed over local highs in topography. The associated convex-upwards curvature would act to defocus the reflected seismic energy and result in lower amplitudes relative to more gently sloping or flat areas of the survey. Therefore we can assume that the amplitude values recorded over regions of sharp increases in topography (e.g., -126.85° , 48.7° on Figure 3.1) are smaller than would be recorded if the seafloor was flat since the amplitudes are not corrected for defocusing.

The broad depression across the central portion of the survey has a general curvature which is concave-upwards. We expect high relative amplitudes over the central portion of the depression in response to focusing effects, but these are not observed in the data.

5.1.2 Scattering and Anelastic Attenuation

The effects of scattering and anelastic attenuation are difficult to assess accurately, and the two effects are even harder to separate from one another. Both will act to reduce the

recorded amplitudes and both will have the largest effect for the highest source frequencies (Warner, 1990).

Attenuation

No correction for attenuation was made to the amplitude data because the target depth of the BSR was less than 240 mbsf. However, this effect might explain the observed reduction in amplitude with an increase in source frequency (see Figures 2.3 and 2.4). It is reasonable to assume that the Q value for the seawater is very high (2000+) and thus very little energy is lost for these sections of the raypath. However, between the seafloor and the BSR, the lowest frequency data cycle approximately 4 times each way (down and up), compared to 10 times for the 75 Hz data, and 18 times for the 150 Hz data. A decrease in the effective Q value with increase in frequency may partially explain the decrease in relative amplitude strength between the BSR and seafloor, observed when comparing the data from the three primary source frequencies. Unfortunately no independent data were available which estimated the effective for these sediments. It is mentioned here as a potential source of error.

Scattering

The degree of seafloor surface roughness is the primary factor affecting the scattering of acoustic waves. If the magnitude of the roughness is sufficiently small ($< 1/4 \lambda$), energy loss, L , due to scattering can be described by the Eckhart scattering law, (Diachok et al., 1994);

$$L = e^{-2g^2} \quad (5.1)$$

where $g = 2ks(\sin \theta)$, k is the wave number, s is the surface roughness, and θ is the grazing angle. Because amplitude to RC conversion using the bin-by-bin Warner's method returned inconsistent results, it is speculated that, over the regions where WBM amplitudes are anomalously low, scattering due to surface roughness may have affected the amplitudes of the WBM reflection more severely than the seafloor primary reflection. The reasons for this are two-fold: (1) the WBM samples the seafloor twice in its path to

the receiver and therefore will experience scattering effects twice, and (2) the incident angles of the WBM raypath are closer to 90° , for which Eckhart's law predicts maximum energy losses. This speculation is supported in experimental studies of reflection loss from the ocean bottom by Hannay (1995). The studies showed that the two-bottom reflection paths were significantly less focused about the specular reflection raypath than the single bottom reflection path, consistent with the scattering theory which predicts stronger scattering and a greater angular spread for higher grazing angles. We assume that this effect is minimized over the region where the conversion coefficient is consistent from trace-to-trace, since the recent sedimentation interpreted in these areas should result in a very smooth sea bottom.

Several mathematically rigorous studies exist on the theoretical and observed scattering effects of small-scale roughness (e.g., Watson and Keller, 1983; Labianca and Harper, 1977; Twersky, 1983). Unfortunately, the scale of seafloor roughness is not well known for the survey area, and therefore no reliable correction can be made. However, we suggest that recorded amplitudes can again be considered smaller than would be recorded from an ideally smooth reflector since they are uncorrected for scattering.

5.2 FREQUENCY ANALYSIS RESULTS

5.2.1 Tuning Width Analysis

Tuning width analysis of the three primary frequencies has determined that the single symmetrical pulse of the BSR reflection can not be the result of tuning between the top and bottom of either a thin HVZ above, or a thin LVZ below the BSR. Both zones must be gradational, increasing in velocity for the LVZ and decreasing in velocity for the HVZ, away from the BSR interface, and each must be a minimum of 15-20 m thick ($30 \text{ Hz } 1/4 \lambda$). A gradationally decreasing velocity structure for the presumed hydrated sediments above the BSR is supported by the VSP and sonic log velocity estimates, the OBS analysis from Spence et al. (1995), and the RMS interval velocity estimates from the

MCS data in the survey area (Yuan et al., 1994). The RMS velocity estimates are able to define the anomaly, but the depth interval where hydrates are anticipated has been excluded to derive the "norm" or background velocity structure. VSP velocity estimates are limited to 15 m below the BSR, and therefore do not provide conclusive evidence for gradational velocity structure of the LVZ. However, the tuning width analysis, together with the observed reflectivity below the BSR on all primary frequency seismic sections support this assessment.

A gradational top to the hydrated zone is expected following the hydrate formation model proposed by Hyndman and Davis (1992) (see section 1.3.2). Their model, as well the gas bubble migration of Minshull et al. (1994), predicts that the hydrate layer will build upward from the base of the stability field. The layer thus has a sharp base and a transitional upper boundary, and with progressive fluid migration its concentration and thickness increase. This result is important because it contrasts with the vertical distribution of hydrate predicted by the in-situ model of methane hydrate formation. Since the entire section from the seafloor to the BSR is within the stability field, the in-situ formation model implies a more uniform concentration of hydrate and high velocity, relative to background velocity, throughout this section. Clearly this is not observed as we see sonic log velocities at Site 889 return to the background velocity function above approximately 125 mbsf (compare Figures 2.10 and 4.5). A gradational LVZ implies that the hydrate builds upward from the base of the stability zone, and thus supports the fluid migration model of Hyndman and Davis (1992).

5.2.2 Seafloor Reflectivity Implications

High seafloor reflectivity is observed over some regions of the survey area by the 75 Hz data, but not by the 30 Hz data. This observation can be partially explained by a thin high-velocity zone at the seafloor (~2 m). The HVZ must be thin enough so that for 30 Hz data, destructive interference between the top and bottom reflections attenuates

reflection strength considerably so that only a small increase in seafloor amplitude is observed (i.e., < 25% increase). However, the HVZ must still be thick enough so that a significant increase in amplitude is observed for the 75 Hz data (i.e., >200%). Synthetic seismic data computed for a 2 m thick layer with a velocity of 3000 m/s return amplitudes close to what are observed in the data.

5.3 REFLECTION COEFFICIENT ANALYSIS RESULTS

5.3.1 Seafloor Reflectivity

For the 75 Hz data set recorded over GRID A (Figure 3.8), seafloor RCs as high as 0.5-0.6 (depending on method of amplitude scaling) were observed over the anticlinal ridge which runs the length of the survey. RC values of this magnitude and higher (e.g., 0.7 - 0.71), were obtained for the Cascadia accretionary margin, offshore Oregon (Carson et al., 1994). These authors attributed high RC values to the influence of carbonate diagenesis at the seafloor. It is presumed that the HVZ at the seafloor in our study area is also the result of hydrothermal alteration of sediments resulting in a thin carbonate pavement at the seafloor, and that this diagenesis can be attributed to increased methane fluid flow in those regions.

Diagenesis occurs as methane-bearing pore waters are exposed to the low-temperature, lower-pressure, oxidizing conditions at or near the seafloor. Near-surface oxidation precipitates diagenetic calcite, aragonite, and/or dolomite at fluid expulsion sites (Ritger et al., 1987). Using results from GLORIA sidescan surveys Carson et al. (1994) have identified carbonate pavements above ridges, similar in structure to where we observe anomalously high seafloor reflectivity in this study area. Although these authors have attributed much of the fluid transport to localized faults in their area, the pavement areas they identified are often several kilometers wide suggesting that perhaps a more dispersed fluid-flow regime is responsible. Regardless of methane transport mechanism, carbonate pavements have been observed and sampled (with ALVIN) in the

Cascadia subduction zone (Carson et al., 1994), and are therefore a practical model for the observed increase in reflectivity over some regions of the seafloor in our survey area. Potentially seafloor reflectivity from 12 kHz Seamarc II data could be analyzed for anomalous regions of high seafloor reflectivity, and this could in turn be used to identify regions where there is a higher than normal probability that hydrated sediments will be found at depth.

The observed regions of high reflectivity at the seafloor suggest a considerable flux of methane bearing fluids from depth to the surface, and thus imply that the sediments above the hydrate stability zone are reasonably permeable since no major fault conduits are present. This rationale also supports the fluid migration theory of hydrate formation.

The smaller seafloor RCs of 0.15-0.25 are consistent with the reflection coefficients anticipated for distal margin turbidites in the Cascadia margin, and are in general agreement with the RC values obtained by Rohr et al. (1993). Such seafloor RCs correspond to large increases in density, 1.05 g/cm^3 to $>1.55 \text{ g/cm}^3$, but a very minimal, if any, increase in velocity ($\sim 1460 \text{ m/s}$) since turbiditic sediments at the surface are unconsolidated muds and clays. RC values are essentially constant for sand percentages from 0 to 35% and for clay percentages from 0 to 100% (from drilling results, ODP Site 855; Rohr et al., 1993).

5.3.2 BSR Reflectivity

The reflection coefficient variability of the BSR over GRID A (Figure 3.9) follows closely the variability exhibited by the seafloor (Figure 3.8). The highest BSR RCs were observed below the topographic highs at $-126.85^\circ, 48.69^\circ$ and at $-126.79^\circ, 48.71^\circ$. These areas have average RC values of 0.10 with localized highs between 0.13 and 0.15. Away from the topographic highs, RC values range between 0.05 and 0.08, with the exception of a region of high RC NW of 889B, and another centered at $-126.775^\circ, 48.66^\circ$. These

results are similar to BSR reflection coefficients obtained with vertically-incident seismic data over Blake Ridge offshore North Carolina. Katzman et al. (1994) obtained reflection coefficients of 0.09 ± 0.04 for the strongest BSRs in their survey area. Results are also consistent with those obtained for a BSR offshore Peru by Miller et al. (1991), who determined the BSR impedance contrast to be the result of a free gas zone (with no distinguishable base) beneath a zone where hydrate fills >15% of the porosity.

Correlation between seafloor topography and both seafloor and BSR RC is immediately apparent (Figures 3.8 and 3.9). As such, it is conceivable that topography is providing a major control on the reflectivity. From the 3-D map of figure 2.14 we can identify closure around the topographic high at $-126.85^\circ, 48.69^\circ$, and closure around the other local maximum at $-126.79^\circ, 48.71$ along the landward edge of the survey can be verified from Seamarc II acoustic sea bottom imagery (Hyndman et al., 1994). Volumes of methane-bearing fluids from broad areas at depth may have become significantly concentrated under these closed topographic highs, and have thus resulted in larger volumes of methane becoming hydrated above the BSR. In turn, larger volumes of methane fluids may reach the surface. This hypothesis requires that the BSR itself acts as a semi-permeable barrier which impedes, but does not completely obstruct, the migrating fluid. As the fluid migrates past the BSR, methane becomes hydrated when an empty "water-cage" exists nearby, or it continues to move upward with the fluid until it reaches the surface where it may become precipitated out of solution in some form of diagenesis. Such a scenario can explain the increased RCs observed for the BSR and for the seafloor below topographic maxima. This hypothesis might also explain why the base of the free gas zone is gradational; as the dissolved methane in migrating fluids becomes more concentrated near the BSR, the fluid may become over-saturated and release the methane as small quantities of free gas. The probability of over-saturation will decrease with depth as the concentration of methane decreases and pressure increases. The result is a gradational decrease in free gas with depth.

The hypothesis that the BSR may form a semi-permeable seal and therefore act as a trap, although not well established, does have its supporters. White (1978) interpreted from seismic data that hydrate layers trapped free gas in the Gulf of Oman, and inferred that the hydrate layer was only relatively impermeable to allow for reduced advection of pore fluids. These interpretations were supported by high amplitude seismic reflections as well as core samples. Lodolo et al. (1992) concluded from seismic studies offshore Antarctica, that the high amplitude reflections corresponding to the base of the hydrate stability field were due in part to trapping of free gas by the base of a semi-permeable methane hydrate seal. Similarly, Collins and Watkins (1985) showed that seismic and geochemical evidence supported a conclusion that small amounts of free gas were being trapped beneath a relatively impermeable hydrate layer off southwestern Mexico. Finally, at the Blake Ridge, Paull et al. (1995) attributed an increased flux of methane-bearing fluids at the seafloor to the fluid and free gas concentrating effects of a domed hydrate layer at approximately 250 mbsf.

5.4 ESTIMATES OF HYDRATE SATURATION

The survey design of GRID A has allowed us to make interpretations of the regional variability in reflector strength for the BSR. We have estimated the hydrate concentration above the BSR from the results of the RC analysis, to obtain a regional interpretation of hydrate distribution for this study area. From this map of hydrate concentration in the sediments, we can estimate the amount of methane gas that is sequestered in hydrate form within the 100 km² of this area. This information can then be used as a constraint for the estimates of carbon content in larger areas such as the entire Cascadia subduction margin.

5.4.1 Hydrate Volume Estimate Assumptions

In order for the initial hydrate concentration estimate to be made, several assumptions are necessary. These are listed below with appropriate qualifying discussion.

(1) The velocity below the BSR is a constant, set to 1515 m/s corresponding to the only available data points from the VSP at ODP Site 889.

We assume this to be reasonably valid since any increases in gas concentration above 1% will have very little effect on the resulting sediment velocity (Domenico, 1978). It can be argued that where the BSR is very weak, concentrations of gas less than 1% may exist in the sediments below the BSR, but often for these areas no BSR was interpreted and thus, they will not make a contribution to the total hydrate volume estimate. In this respect, the volume will be under-estimated.

(2) Density is constant across the BSR and thus the impedance contrast (RC) is solely the result of variation in velocity.

Hydrate density (0.93 g/cm³ [Kvenvolden and MacDonald, 1985]) is nearly the same as pore water density, so density of hydrated sediments is little different from the density of unhydrated sediments. Furthermore, in the gas-bearing sediments below the BSR, the gas concentrations are so small (MacKay et al., 1994), that the presence of gas has little effect on sediment density. The available density log and core data at Site 889 (Figure 2.10) also suggest that density is constant, independent of velocity, and is therefore a reasonable assumption for the rest of the study area.

(3) The velocity increase above the BSR, relative to the background velocity, is a result of the infilling of a percentage of the pore space with methane hydrate. Replacing pore water with high-velocity hydrate has the same effect as replacing pore water by sediment matrix; that is, the sediment velocity increases because the porosity is effectively reduced.

We use the porosity-velocity relationship of Hyndman et al. (1993), described by the equation,

$$\phi = -1.18 + \frac{8.607}{v} + \frac{-17.89}{v^2} + \frac{13.94}{v^3}, \quad (5.2)$$

where ϕ is porosity and v is velocity in km/s. This relationship was developed initially for the Nankai margin offshore Japan, but recent experiments by Davis and Fisher (1994) have shown that the function provides a very good fit to the observed velocity-porosity relationship in the Cascadia subduction zone for unhydrated, gasless sediments. Although pure hydrate velocity (3800 m/s) is somewhat slower than that of the matrix (~4500 m/s), the increase in grain boundary adhesion by the hydrate make it as effective in increasing velocity as reducing the porosity (i.e., increasing the matrix content). Using a lower velocity would increase the calculated porosity.

(4) The difference in porosity calculated from background sediment velocity and hydrated sediment velocity equals the concentration of hydrate in the sediment.

This assumption is the least supported of the four. The increase in velocity with no apparent decrease in porosity observed from logging data, suggests that hydrate may be the cause of the observed velocity increase. However, the effect of diagenetic cementation may also increase the velocity, without significantly affecting porosity. We allow that this may be a source of error in which our hydrate volume may be over-estimated.

5.4.2 Hydrate Concentration Calculation

Assumption (2) states that the observed reflection coefficient is entirely the result of the velocity contrast at the BSR interface. Rearranging equation 3.6, we can now calculate the velocity of the upper layer v_1 at the BSR, from the assumed velocity of the bottom layer v_2 and the observed RC,

$$v_1 = v_2 \frac{1 - RC}{1 + RC}. \quad (5.3)$$

The upper layer velocity at the BSR was established for each bin in GRID A. The theoretical porosity at the BSR was then calculated for these velocities from equation 5.2. The porosity at the BSR was also established for the "best-fit" background velocity of

1625 m/s. Porosity calculated from equation 5.2 for the background velocity was 59%, 4% higher than the neutron-porosity well log values of ~55% obtained from Site 889 (MacKay et al., 1994). For consistency only equation 5.2 was used when determining porosity differences between hydrated and unhydrated sediments. The difference in porosity at each bin was calculated and thus a regional representation of hydrate concentration was established. Figure 5.1 shows the calculated velocity, and associated hydrate concentration for the sediments immediately above the BSR (i.e., within $1/2 \lambda$, or 11 m) using the best-fit approximation for the background velocity function. The median hydrate concentration for GRID A is between 5% and 10% of the sediment volume, or 10-20% of the pore space. The highest concentrations are associated with the high reflectivity observed beneath the topographic maxima and reach values as high as 15-18% of the sediment volume. Concentrations higher than 21% are not observed.

Near drillsite 889B we see that the hydrate concentration returned by this calculation is roughly 12-15%, or 24-30% of the pore space. This is in approximate agreement with the 0-20% estimate of hydrate concentration in sediment obtained from ODP well logs at Site 889B by MacKay et al. (1994). These estimates are also consistent with the 10-15% estimate from MCS data by Yuan et al. (1995) and with the 15-18% concentration in sediment estimated from pore fluid geochemical data from recovered cores at Site 889B (Desmons et al.; in preparation, 1995).

We note here that a shift in the background velocity will directly affect the calculated hydrate concentration. We are confident that the background velocity of Yuan et al. (1994) approximates the unhydrated velocity very closely, due to the consistency of the RMS velocity calculations. However, an estimate of the error in the calculation can be obtained by determining hydrate concentrations using the 95% confidence limits of the best-fit background velocity estimate. These are 1600 m/s and 1670 m/s for the low and high limits, respectively. A 1600 m/s background velocity increases calculated hydrate concentrations by a factor of approximately 1.1, while the upper limit decreases hydrate

HYDRATE VELOCITY AND HYDRATE CONCENTRATION

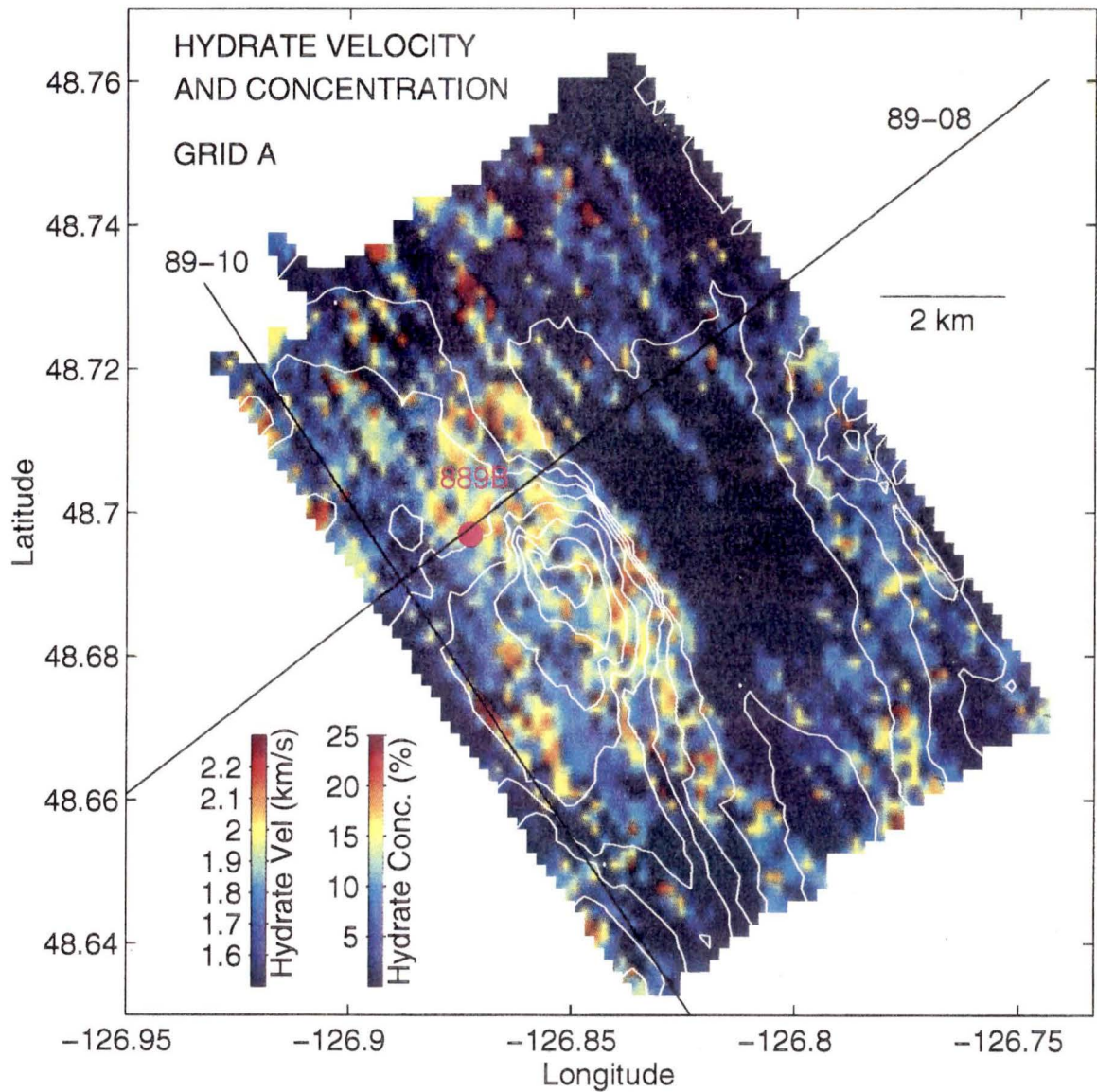


Figure 5.1

Hydrate velocity and concentration map, for the sediments immediately above the BSR. Concentration is measured as a percent of the total sediment volume. Velocity above the BSR is estimated from the reflection coefficients at each bin in GRID A, by assuming that the velocity below the BSR is constant. Below the BSR small concentrations of free gas are assumed within the sediments resulting in a velocity of 1515 m/s. Because velocity does not change appreciably for free gas concentrations greater than 1%, this velocity is assumed everywhere beneath the BSR. Concentrations are determined from the calculated porosity differences between hydrate velocity and a background velocity of 1625 m/s.

concentrations to about 0.88 of the best-fit values. From this simple calculation the estimate for error in hydrate concentration from this source is approximately $\pm 10\%$.

5.4.3 Regional Methane Gas Volume Estimate

Having established the concentration of hydrate near the BSR, we are now able to make a crude estimate of the total volume of methane gas within the 100 km² survey area. We begin by making two additional assumptions;

- (1) The concentration of hydrate is assumed to be decreasing linearly with increasing distance above the BSR to a zero concentration at 100 m above the BSR, or 124 mbsf.
- (2) The ratio of volume of methane gas to volume of solid methane hydrate at standard temperature and pressure is assumed to be 164:1.

The first assumption, although not well constrained, is supported by the sonic log velocity data which shows a return to the assumed background velocity at a depth of 125 mbsf. A linearly decreasing concentration over 100 m of sediment translates to 50 m of sediment of constant hydrate concentration. The second assumption follows the laboratory studies of Sloan (1990), and is commonly agreed to be the gas to solid ratio for methane hydrate.

Each bin in GRID A then represents a 185 m X 185 m X 50 m cube of hydrated sediments with a concentration of hydrate given by the value returned from the porosity-difference calculation described above (section 5.4.2). The total solid hydrate from the sum of these bins is $\sim 3.92 \times 10^8 \text{ m}^3$. The volume of methane gas sequestered in this volume of hydrate is obtained from the gas to solid ratio resulting in a gas volume of $\sim 6.43 \times 10^{10} \text{ m}^3$. Finally we convert this number to the more commonly referenced gas volume units, trillion cubic feet (tcf), to obtain a total methane gas volume for our detailed survey area of $\sim 2.07 \text{ tcf}$. If the concentration at the drillhole was taken to be representative of the entire area, and all other variables remained the same, that volume

estimate would be ~4.30 tcf, a factor of 2.08 greater than our variable concentration estimate.

We have determined that our hydrate concentration values and subsequent gas volumes are under-estimated by some degree, due to factors which acted to reduce recorded amplitudes (see section 5.1), even though diagenesis of sediments above the BSR may have caused an over-estimate in the porosity difference calculation. The total error in our volume calculations from these sources is estimated to be less than 20%.

CHAPTER SIX CONCLUSIONS

Analysis of seismic data with such a high density of coverage and unique variability of source frequency had not been previously undertaken for the study of methane hydrates in the Cascadia subduction zone. This kind of analysis has produced some interesting and unexpected results. I feel these results are well supported and make a significant contribution to the scientific community concerned with the hydrate problem. I believe the following conclusions from this study should be emphasized.

Synthetic seismogram and reflection coefficient analyses in this study confirm that a concentration of free gas of at least 1-5% in the sediments below the BSR is necessary to produce the observed impedance contrast, even with a 10-15% concentration of hydrate present above the BSR. Without a concentration of free gas below the stability zone, and assuming that the VSP velocities from drillsite 889 are accurate, the theoretically calculated impedance is at least 50% less than is observed (with 10% hydrate). The existence of free gas below the hydrate stability zone had been long debated in previous BSR studies in the Cascadia subduction zone, and although many authors suspected free gas, no conclusive evidence existed to support their speculation. I believe the data analysis and modeling results presented here provides that evidence.

The frequency response of the seafloor and the BSR has been examined through synthetic seismogram modeling. It has been shown that a minimum thickness of 5 to 10 meters is required for either the hydrated sediments above or the free gas bearing sediments below the BSR, in order to yield the observed seismic response. That is, neither a thin layer of free gas below, nor a thin layer of hydrate above the BSR, is responsible for the single symmetrical pulse observed for the BSR in this area. It was determined that both of these layers must be gradational, decreasing in concentration away from the BSR.

The regional variation of hydrate concentration in the sediments above the BSR ranges from 10% to 35% of the pore space, assuming 50% porosity in the sediments at this depth, and the variability in concentration appears to be strongly controlled by topography. Fluid focusing effects due to the apparent closure of the semi-permeable hydrate seal at the base of the stability zone, and which follows the topographic contours, may be responsible for an increase in the flux of methane bearing fluids beneath the topographic highs. An increase in fluid flux is a probable mechanism for the increased hydrate concentration detected beneath these structural highs over the survey area. It has also been suggested by many authors (MacKay et al, 1995; Whiticar, personal communication, and others) that the base of the hydrate stability field has moved up section in the recent geologic past. Free methane gas, dissociated from the paleo-base of the stability zone, should have also become concentrated below the structural highs. As this concentration of free gas migrated up into the newly established stability zone it will also have contributed to an increase in the hydrate concentration in these areas.

The anomalously high reflectivity observed at the seafloor over topographically higher regions of the survey can be partially explained by the presence of a thin layer of diagenitically-induced carbonate pavement. The presence of carbonate pavement in these areas is consistent with the hypothesis of increased fluid flux under regions of high topography as explained above. Carbonate pavement, although observed at the seafloor along the Oregon margin, has not been previously observed, or inferred as in this case, over this region of the Cascadia margin. Although no record of carbonate pavement was obtained from the drilling during ODP Leg 146, the geophysical evidence presented here does support such a hypothesis.

The conclusions presented here are consistent with the fluid expulsion model for hydrate formation. As such, this model is determined to be representative of the methane hydrate formation process in this area, and by extension, in areas all along the Cascadia margin where methane hydrates are found.

Volume Estimate Conclusions

The volume of methane gas sequestered in hydrate form for the 100 km² of GRID A is estimated at approximately 2.07 tcf. It is noted here that a simplified calculation from only the borehole data at drillsite 889B would over-estimate the total gas volume by more than a factor of 2. It is hoped that this detailed, variable concentration estimate will improve current volume estimates of methane gas contained in hydrate form, and that the methodology described here may be used to improve global methane hydrate estimates.

BIBLIOGRAPHY

- Anstey, N.A., 1966. The sectional autocorrelogram and the sectional retrocorrelogram: *Geophysical Prospecting*, v. 14, p. 389-426.
- Appenzeller, T., 1991. Fire and ice under the deep-sea floor: *Science*, v. 252, p. 1790-1792.
- Brooks, J.M., H.B. Cox, W.R. Bryant, M.C. Kennicutt II, R.G. Mann, and T.J. MacDonald, 1985. Association of gas hydrates and oil seepage in the Gulf of Mexico: *Advanced Organic Geochemistry*, v. 10, p. 221-234.
- Carson, B., E. Seke, V. Paskevich, and M.L. Holmes, 1994. Fluid expulsion sites on the Cascadia accretionary prism; Mapping diagenetic deposits with processed GLORIA imagery: *Journal of Geophysical Research*, v. 99, p. 11959-11969.
- Claypool, G.W., and I.R. Kaplan, 1974. The origin and distribution of methane in marine sediments, in *Natural Gases in Marine Sediments*, I.R. Kaplan, ed., Plenum, New York, p. 99-139.
- Clowes, R.M., C.J. Yorath, R.D. Hyndman, 1987. Reflection mapping across the convergent margin of western Canada: *Geophysical Journal of the Royal Astronomical Society*, v. 89, p. 79-84.
- Collett, T.S., 1992. Potential of gas hydrates outlined: *Oil and Gas Journal*, v. 90(25), p. 84-87.
- Collins, B.P., and J.S. Watkins, 1985. Analysis of a gas hydrate off southwest Mexico using seismic processing techniques and Deep Sea Drilling Project Leg 66 results: *Geophysics*, v. 50, p. 16-24.
- Davis, E.E., and J.L. Karsten, 1986. On the asymmetric distribution of sea mounts about the Juan de Fuca ridge; ridge-crest migration over a heterogeneous asthenosphere: *Earth and Planetary Science Letters*, v. 79, p. 385-396.
- Davis, E.E., and R.D. Hyndman, 1989. Accretion and recent deformation of sediments along the northern Cascadia subduction zone: *Geological Society American Bulletin*, v. 101, p. 1465-1480.
- Davis, E.E., R.D. Hyndman, and H. Villinger, 1990. Rates of fluid expulsion across the northern Cascadia accretionary prism: constraints from new heat-flow data and multichannel seismic reflection data: *Journal of Geophysical Research*, v. 95, p. 8869-8889.
- Davis, E.E., and A.T. Fisher, 1994. On the nature and consequences of hydrothermal circulation in the Middle Valley sedimented rift; inference from geophysical and geochemical observations, Leg 139: in *Proceedings of Ocean Drilling Program, Scientific Results, V. 139*, M.J. Mottl, E.E. Davis, A.T. Fisher, and J.F. Slack, eds., College Station, TX. (Ocean Drilling Program), p. 695-717.
- Desmons, B. et al., 1995. personal communication.

- Diachok, O.I., R.L. Dicus, and S.C. Wales, 1994. Elements of a geoacoustic model of the uppercrust: *Journal of the Acoustical Society of America*, v. 75, p. 324-334.
- Domenico, S.N., 1976. Effect of brine-gas mixture on velocity in an unconsolidated sand reservoir: *Geophysics*, v.41, p. 882-894.
- Englezos, P., and Bishnoi, P.R., 1988. Prediction of gas hydrate formation in aqueous solutions: *American Institute of Chemical Engineers*, v.34, p.1718-1721.
- Gornitz, V., and I. Fung, 1994. Potential distribution of methane hydrates in the world's oceans: *Global Biogeochemical Cycles* v. 8(3), p. 335-347.
- Hamilton, E.L., 1978. Sound velocity-density relations in sea-floor sediments and rocks: *Journal of the Acoustical Society of America*, v. 63, p. 366-377.
- Hammerschmidt, E.G., 1934. Formation of gas hydrates in natural gas transmission lines: *Industrial Engineering (Chemical)*, v. 26, p. 851-855.
- Hannay, D.E., 1995. Estimation of geoacoustic parameters of the ocean bottom by inversion of reflection loss data: M.Sc. Department of Physics and Astronomy, University of Victoria, Victoria, B.C.
- Hannay, D.E. and N.R. Chapman, 1995. Analysis of geoacoustic shot run data from the Pacific Shelf experiment: JASCO Research Ltd. for Defence Research Establishment Pacific, Research and Development Branch, Department of National Defence, Sydney, B.C., p.15.
- Holder, G.D., V.A. Kamath, and S.P. Godbole, 1984. The potential of natural gas hydrates as a fuel source: *Annual Reviews of Energy*, v. 9, p. 427-445.
- Hyndman, R.D., 1983. Geothermal heat flux, Juan de Fuca Plate map: *Juan de Fuca Plate Map Service., Pacific Geoscience Centre, Geological Survey of Canada*.
- Hyndman, R.D., C.J. Yorath, R.M. Clowes, and E.E. Davis, 1990. The northern Cascadia subduction zone at Vancouver Island; Seismic structure and tectonic history: *Canadian Journal of Earth Science*, v. 27, p. 313-329.
- Hyndman, R.D., 1992. "Ice" beneath the deep sea: Studies of methane hydrate layers beneath the continental slope off Vancouver Island: *Geoscience Canada*, v. 19, p. 21-26.
- Hyndman, R.D., J.P. Foucher, M. Yamano, A. Fisher, et al., 1992. Deep sea bottom simulating reflectors; Calibration of the base of the hydrate stability field as used for heat flow estimates: *Earth and Planetary Science Letters*, v. 109, p. 289-302.
- Hyndman, R.D. and G.D. Spence, 1992. A seismic study of methane hydrate marine bottom simulating reflectors: *Journal of Geophysical Research*, v. 97, p. 6683-6698.
- Hyndman, R.D. and E.E. Davis, 1992. A mechanism for the formation of methane hydrate bottom simulating reflectors by vertical fluid expulsion: *Journal of Geophysical Research*, v. 97, p. 7025-7041.

- Hyndman, R.D., G.F. Moore, and K. Moran, 1993. Velocity, porosity, and pore-fluid loss from the Nankai subduction zone accretionary prism: In *Proceedings of the Ocean Drilling Program, Scientific Results*, Vol. (131), College Station, TX (Ocean Drilling Program), P.211-220.
- Hyndman, R.D., G.D. Spence, T. Yuan, and E.E. Davis, 1994. Regional geophysics and structural framework of the Vancouver Island margin accretionary prism: *Proceedings of the Ocean Drilling Program, Initial Reports*, v. 146 (I), G.K. Westbrook, B. Carson, R.J. Musgrave et. al.; eds., p.399-419.
- Jarrard, R.D., M.E. MacKay, G.K. Westbrook, and E.J. Screaton, 1995. Log-based porosity of ODP sites on the Cascadia accretionary prism: *Proceedings of the Ocean Drilling Program, Scientific Results, Volume 146*, Carson, B. and K. Westbrook et al.,(eds.), College Station, TX., (Ocean Drilling Program), *in press*.
- Katzman, R., W.S. Holbrook, and C.K. Paull, 1994. Combined vertical-incidence and wide-angle seismic study of a gas hydrate zone, Blake Ridge: *Journal of Geophysical Research*, v. 99, p. 17,975-17,995.
- Kvenvolden, K.A., and L.A. Barnard, 1983. Hydrates of natural gas in continental margins, in Studies in Continental Margin Geology, Mem. 34, J.S. Watkins and C.L. Drake, eds., p. 631-640, American Association of Petroleum Geologists, Tulsa, Okla.
- Kvenvolden, K.A., 1988. Methane hydrates and global climate: *Global Biogeochemical Cycles*, v. 2(3), p. 221-229.
- Kvenvolden, K.A. and A. Grantz, 1992. Gas hydrates in the arctic region, in The Arctic Ocean Region: The Geology of North America, GSA, Boulder, Colo., v. L. , Grantz, A., Johnson, L., & J.F. Sweeney, eds., p. 539-549.
- Kvenvolden, K.A., 1993. Gas hydrates-geological perspective and global change: *Reviews of Geophysics*, v. 31, p. 173-187.
- Labianca, F.M., and E.L. Harper, 1977. Connection between various small wave-height solutions of the problem of scattering from the ocean surface: *Journal of the Acoustical Society of America*, v. 62, p. 1144-1157.
- Lodolo, E., A. Camerlenghi, and G. Brancolini, 1993. A bottom simulating reflector on the South Shetland margin, Antarctica Peninsula: *Antarctic Science*, v. 5(2), p. 207-210.
- MacDonald, G.T., 1990a. The future of methane as an energy resource: *Annual Reviews of Energy*, v. 15, p. 53-83.
- MacDonald, G.T., 1990b. The role of methane clathrates in past and future climates: *Climate Change*, v. 16, p. 247-281.
- MacKay, M.E., R.D. Jarrard, G.K. Westbrook, and R.D. Hyndman et. al., 1994. Origin of bottom simulating reflectors: Geophysical evidence from the Cascadia accretionary prism: *Geology*, v. 22, p. 459-462.
- Makogan, Y.F., 1981. Hydrates of Natural Gas, Penwell, Tulsa, p.237.

- Max, M.D., W.P. Dillon, and R.D. Malone, 1991. Report on National Workshop on Gas Hydrates: U.S. Geological Survey, Reston, VA., published by U.S. Department of Energy.
- Miller, S.L., 1974. The nature and occurrence of clathrate hydrates, in Natural Gases in Marine Sediments, I.R. Kaplan, ed., Plenum, New York, p. 151-177.
- Miller, S.A., M.W. Lee, and R. von Heune, 1991. An analysis of a seismic reflection from the base of gas hydrate zone: *American Association of Petroleum Geologists Bulletin*, v. 75, p.910-924.
- Minshull, T.A., and R.S. White, 1989. Sediment compaction and fluid migration in the Makran accretionary prism: *Journal of Geophysical Research*, v. 94, p. 7387-7402.
- Minshull, T.A., S.C. Singh, and G.K. Westbrook, 1994. Seismic velocity structure at a gas hydrate reflector, offshore western Columbia, from full waveform inversion: *Journal of Geophysical Research*, v. 99, p. 4715-4734.
- Murota, T., 1995. Personal communication, York University.
- Peacock, K.L., and S. Treitel, 1969. Predictive deconvolution: theory and practice: *Geophysics*, v. 34, p. 155-169.
- Raynaud, B.A., 1988. Diffraction modeling of 3-D lower-crustal reflectors: *Geophysics*, v. 93, p. 149-161.
- Rice, D. and Claypool, G.W., 1981. Generation, accumulation, and resource potential of biogenic gas: *American Association of Petroleum Geologists Bulletin*, v. 65, p. 5-25.
- Riddihough, R.P., 1984. Recent movements of the Juan de Fuca Plate system: *Journal of Geophysical Research*, v. 89, p. 6980-6994.
- Ritger, S., B. Carson, and E. Suess, 1987. Methane-derived authigenic carbonates formed by subduction-induced pore-water expulsion along the Oregon/Washington margin: *Geological Society of America Bulletin*, v. 98, p.147-156.
- Rohr, K.M.M., U. Schmidt, and H. Groschel-Becker, 1993. Regional patterns of hydrothermal alteration of sediments as interpreted from seafloor reflection coefficients, middle valley, Juan de Fuca Ridge: *Geophysical Research Letters*, v. 20(17), p. 1867-1870.
- Shine, K.P., R.G. Derwent, D.J. Wuebles, J.J. Morcette, 1990. Climate Change. The IPCC Scientific Assessment, J.T. Houghton, G.J. Jenkins, and J.J. Ephraums, eds., Cambridge Univ. Press, New York, p.41-68.
- Singh, S.C., T.A. Minshull, and G.D. Spence, 1993. Velocity structure of a gas hydrate reflector: *Science*, v. 260, p. 204-207.
- Singh, S.C., and T.A. Minshull, 1995. Velocity structure of a gas hydrate reflector at Ocean Drilling Program site 889 from a global seismic waveform inversion: *Journal of Geophysical Research*, v.99, p. 24221-24233

- Sloan, E.D., 1990. Clathrate hydrates of natural gas, Marcel Dekker, ed., New York, p. 641.
- Spence, G.D., R.M. Clowes, and R.M. Ellis, 1991. Seismic structure across the active subduction zone of western Canada: *Journal of Geophysical Research*, v. 90, p. 6754-6772.
- Spence, G.D., R.D. Hyndman, S.G. Langton, E.E. Davis, and C.J. Yorath, 1991. Multichannel seismic reflection profiles across Vancouver Island continental shelf and slope: *Open-File Report. - Geological Survey of Canada*, 2391.
- Spence, G.D., R.D. Hyndman, et. al., 1991. Seismic structure of the northern Cascadia accretionary prism; evidence from new multichannel seismic reflection data: in *Continental Lithosphere, Deep Seismic Reflections*, Meissner, R., L. Brown, W. Birbalet, K. Frank, K. Fuchsand, and F. Seifert (eds.), American Geophysical Union, Geodynamic Service, v. 22, p. 257-263.
- Spence, G.D., 1993. Seismic studies of the methane hydrate layer near ODP drillsite 889B, offshore Vancouver Island. Report of Cruise PGC93002, *Centre for Earth and Ocean Research*, Report 93-4.
- Spence, G.D., T.A. Minshull, and C. Fink, 1995. Seismic studies of methane gas hydrate offshore Vancouver Island: *Ocean Drilling Program Scientific Results*, . *in press*.
- Twersky, V., 1983. Reflection and scattering of sound by correlated rough surfaces: *Journal of the Acoustical Society of America*, v. 73, p. 85-94.
- Warner, M., 1990. Absolute reflection coefficients from deep seismic reflections: *Tectonophysics*, v. 173, p. 15-23.
- Watson, J.G., and J.B. Keller, 1983. Reflection, scattering, and absorption of acoustic waves by rough surfaces: *Journal of the Acoustical Society of America*, v. 74, p. 1887-1894.
- Watson, R.T., H. Rodher, H. Oeschger, and U. Siegenthaler, 1990. Greenhouse gases and aerosols, in Climate Change. The IPCC Scientific Assessment, J.T. Houghton, G.J. Jenkins, and J.J. Ephraums, eds., Cambridge Univ. Press, New York, p. 1-40.
- Westbrook, G.K., B. Carson, R.J. Musgrave et. al.; eds., 1994. *Proceedings of the Ocean Drilling Program, Initial Results, Volume 146 (I)*, College Station, TX., (Ocean Drilling Program).
- Westbrook, G.K., 1991. Geophysical evidence for the role of fluids in accretionary wedge tectonics: *Philosophical Transactions of the Royal Society of London A*, v. 355, p. 227-242.
- White, R.S., 1979. Gas hydrate layers trapping free gas in the Gulf of Oman: *Earth and Planetary Science Letters*, v. 42, p. 114-120.
- Whiticar, M.J., 1995. Personal communication. School of Earth and Ocean Sciences, University of Victoria, Victoria, B.C., V8N-2Y2.

- Whiticar, M.J., 1990. A geochemical perspective of natural gas and atmospheric methane, *Organic Geochemistry*, v. 16, p.531-547.
- Wood, W.T., P.L. Stoffa, and T.H. Shipley, 1994. Quantitative detection of methane hydrate through high resolution seismic velocity analysis, *Journal of Geophysical Research*, v. 99, p. 9681-9695.
- Yamano, M.S., S. Uyeda, Y. Aoki, and T.H. Shipley, 1982. Estimates of heat flow derived from gas hydrates: *Geology*, v. 10, p. 339-343.
- Yorath, C.J., R.M. Clowes, R.D. MacDonald, C. Spencer, K. Rohr, J.F. Sweeney, R.G. Currie, J.F. Halpenny, and D.A. Seemann, 1987. Marine multichannel seismic reflection, gravity and magnetic profiles-Vancouver Island continental margin and Juan de Fuca Ridge: *Open-File Report. - Geological Survey Canada*, 1661.
- Yuan, T., G.D. Spence, and R.D. Hyndman, 1994. Inferred seismic velocities and porosities in the accretionary wedge sediments at the Cascadia margin: *Journal of Geophysical Research*, v.99, p. 4413-4427.
- Yuan, T., R.D. Hyndman, G.D. Spence, and B. Desmons, 1995. Velocity structure of a BSR and deep sea gas hydrate concentrations on the northern Cascadia continental slope: *in press*.
- Yilmaz, O., 1987. Seismic Data Processing, S.M. Doherty, ed., Society of Exploration Geophysicists, Tulsa, Oklahoma.

VITA

Surname: Fink

Given Names: Cameron Roger

Place of Birth: Red Deer, Alberta, Canada

Educational Institutions Attended:

University of Victoria	1993 to 1995
University of Alberta	1990 to 1993
Red Deer College	1989 to 1990

Degrees Awarded:

B.Sc. (First Class Honours)	University of Alberta	1993
-----------------------------	-----------------------	------

Honours and Awards:

University of Victoria Graduate Fellowship	1993-95
Canadian Society of Exploration Geophysicists Scholarship	1991-94
BC Advanced Systems Institute, Graduate Scholarship	1993
APEGGA Past Presidents' Society "Leadership Award"	1993
Norcen Energy Scholarship	1991-92
KITE "Award of Excellence for Academic Standing"	1990
Hewlett Packard (Canada) Scholarship	1990

Publications:

G.D. Spence, T.A. Minshull and C.R. Fink, 1995. Seismic Studies of Methane Gas Hydrate, Offshore Vancouver Island: In *Proceedings of the Ocean Drilling Program, Scientific Results*, Volume (146), G.K. Westbrook et al., eds., College Station, TX (Ocean Drilling Program).

PARTIAL COPYRIGHT LICENSE

I hereby grant the right to lend my thesis to users of the University of Victoria Library, and to make single copies only for such users or in response to a request from the Library of any other university, or similar institution, on its behalf or for one of its users. I further agree that permission for extensive copying of this thesis for scholarly purposes may be granted by me or a member of the University designated by me. It is understood that copying or publication of this thesis for financial gain shall not be allowed without my written permission.

Title of Thesis:

Methane Hydrate Distribution Offshore Vancouver Island
From Detailed Single Channel Seismic Studies

Author

Cameron Roger Fink

July 25, 1995